

Contents

Articles

Transformation of BCC and B2 High Temperature Phases to HCP and Orthorhombic Structures in the Ti-Al-Nb System. Part I: Microstructural Predictions Based on a Subgroup Relation Between Phases	L. A. Bendersky, A. Roytburd, and W. J. Boettinger	561
Transformation of BCC and B2 High Temperature Phases to HCP and Orthorhombic Structures in the Ti-Al-Nb System. Part II: Experimental TEM Study of Microstructures	L. A. Bendersky, and W. J. Boettinger	585
Corrosion Characteristics of Silicon Carbide and Silicon Nitride	R. G. Munro and S. J. Dapkunas	607

Conference Reports

North American Integrated Services Digital Network (ISDN) Users' Forum (NIUF)	Elizabeth B. Lennon	633
---	---------------------	-----

News Briefs

GENERAL DEVELOPMENTS	637
United States, Russia Develop Optical Imaging System Biosensor Consortium Announces First Members Standards Working Group Plans Moscow Meeting	
Models Measure Speed of Sound for Gas Mixtures Location Effects in Orifice Flowmeters Documented Key Escrow Encryption Standard Proposed Guide Helps Users Build Open Systems	638
Researchers Help Circuit Layers "Get in Line" Volt Standard Marketed With NIST Cooperation New Test Planned for Paint Industry's Palette DNA Standard Makes the "Top 100" List Novel Chemical Concentrator Makes Debut	639

Consortium to Help Building Systems Communicate Plan Announced to Harmonize U.S. Labs Now Hear This: Sound Used for Cleaner Burns Major Barrier to Advanced Materials Identified	640
GATT Standards Activities Reported for 1992 New Software Simplifies Semiconductor Measurements Cryogenic Alloy Now Available for Licensing New Facility Designed for Better Antenna Assessments	641
1993 Weights and Measures Labs Directory Published Atomic-Level Deposits Promise Solid Returns Researcher Wins Turkey's Highest Science Award Proposals Sought for Precision Measurement Grants Data Tables on Ethane Properties Available	642
First Product Successfully Machined Using STEP NIST Measurement Technology Goes to Market CRADA Sets Plans for Atomic Microclock in Motion	643
NCWM to Work on Price Accuracy in Retail Stores Partners to Develop Powerful Tunable Laser New Device Precisely Measures Hydrogen in Metals Antenna Software Measures "Near and Far"	644
NIST Leads Industry to Resolve Problems in Determining Laser Beam Spatial Parameters NIST, Sandia Collaborate to Develop Tools for Evaluating Thermal Performance of Semiconductor Device Packaging NIST Measurements of Ion Kinetic Energies from RF Plasmas Provide Baseline Data for Semiconductor Processing	645
NIST Contributes to Development of Prototype Software Supporting Computer Design of High-Power Microwave Tubes AFM Maps Observe New Deposition Process	646
Sea-Viewing Radiometer Developed New Ionization Source Developed for Mass Spectroscopy Missing Link in Fission Systematics Found	647
Laser Ionization Monitoring Promises New Diagnostic of Semiconductor Growth NIST Research Associates License Bone Repair/Replacement Material Classification System for Advanced Ceramics Developed by International Collaboration Phase Transition Puzzle Clarified	648
Simultaneous Measurement of Soot Volume Fraction and Temperature in Flames Application Portability Profile (APP) Guide Revised NIST Supports the Department of Defense Computer-Aided Acquisition and Logistic Support (CALs) Initiative in Computer Graphics	649
FIPS for Massachusetts General Hospital Utility Multi-Programming System (MUMPS) Programming Language Revised NIST/ASA/NSF Fellow Develops New Statistical Methods for Manufacturing Process Quality Assurance	650
<i>Calendar</i>	651

Transformation of BCC and B2 High Temperature Phases to HCP and Orthorhombic Structures in the Ti-Al-Nb System. Part I: Microstructural Predictions Based on a Subgroup Relation Between Phases

Volume 98

Number 5

September–October 1993

L. A. Bendersky

National Institute of Standards and Technology,
Gaithersburg, MD 20899-0001

A. Roytburd

Dept. of Materials and Nuclear Engineering,
University of Maryland,
College Park, MD 20742

and

W. J. Boettinger

National Institute of Standards and Technology,
Gaithersburg, MD 20899-0001

Possible paths for the constant composition coherent transformation of BCC or B2 high temperature phases to low temperature HCP or Orthorhombic phases in the Ti-Al-Nb system are analyzed using a sequence of crystallographic structural relationships developed from subgroup symmetry relations. Symmetry elements lost in each step of the sequence determine the possibilities for variants of the low symmetry phase and domains that can be present in the microstructure. The orientation of interdomain interfaces is determined by requiring the existence of a strain-free interface between the domains. Polydomain structures are also determined that minimize elastic energy. Microstructural predictions are made for comparison to experimental results given by Bendersky and Boettinger [J. Res. Natl. Inst. Stand. Technol. 98, 585 (1993)].

Key words: domain structure; elastic accommodation; phases; space group relations; structural relations; Ti-Al-Nb system; transformation path.

Accepted: May 14, 1993

1. Introduction

The need for low density structural materials with high temperature strength and low temperature ductility has stimulated much interest in Ti-Al-Nb alloys. In particular alloys near and in the Ti_3Al-Nb_3Al pseudobinary section with Nb levels from 10 to 30 at% have been investigated [1-8]. It has been shown that alloys with 10-12 and 25 at% Nb have very promising combinations of specific strength and rupture life at room and high (<800 °C) temperatures [1,6,9-14]. The mechanical properties of these alloys were found to be very

sensitive to their microstructure. Most of the microstructures were formed by heat treatments that involve continuous cooling from a high temperature (> 1100 °C) single-phase field with subsequent heat treatment at lower temperatures. The microstructure developed during continuous cooling depends strongly on cooling rate and alloy composition [15-19] and thus affects the microstructure produced from it during the subsequent lower temperature (600 to 900 °C) treatment. From a technological point of view, an understanding of the

formation mechanisms of both continuously cooled and annealed microstructures is very important for processing these alloys for optimum properties, for controlling behavior during thermal cycling, and for obtaining weldability.

Equilibria along the $\text{Ti}_3\text{Al-Nb}_3\text{Al}$ pseudobinary section with $\text{Nb} < 30$ at% involves phases based on two distinct fundamental structures: body centered cubic (BCC) at high temperatures and hexagonal close-packed (HCP) at lower temperatures. The BCC-based phases appear over a wide range of compositions at high temperatures as either a disordered A2 or an ordered B2 (CsCl-type) structure depending on the exact temperature and composition [2-5,20]. For Ti-Al-Nb alloys the B2 ordering appears to have Ti on one site and Al/Nb on the other site [21]. For low Nb content, the HCP-based structures have a disordered hexagonal α phase at intermediate temperatures and an ordered hexagonal DO_{19} phase (Ti_3Al or α_2) at low temperatures. At higher Nb contents, the HCP-based low temperature structure is an orthorhombic O-phase (Ti_2AlNb) [2,4-6,22]. The DO_{19} structure involves binary ordering of the α structure with Ti/Nb occupying one site and Al the other site [23]. The O-phase structure involves further ternary ordering of the α_2 phase with Ti, Al, and Nb predominantly occupying three different sites [2,24]. Due to the structural relations (reflected in the observed Burger's orientation relationships between the phases [2-4,7,8,25]) it is well known that the structural changes (transformations) from BCC- to HCP-based phases can be described as a result of the following, where $(hkl)_c$ refers to the cubic phase:

- 1) distortions of $\{110\}_c$ planes and changes in their interplanar distances;
- 2) shuffles, or relative displacement of neighboring $(110)_c$ planes;
- 3) reordering that changes the distribution (occupancy) of Ti, Al and Nb atoms among the lattice sites.

In the spirit of the Landau theory of phase transitions [26] a common framework is sought to describe all of the BCC- and HCP-based phases. Then in principle, a single thermodynamic potential can be identified as a continuous function of a set of order parameters that describe these three types of structural changes. To obtain such a common framework, a site-to-site correspondence between the structures must be found. This correspondence between atom sites in these phases can be obtained by a single set of Wyckoff sites of the

lowest symmetry phase considered, which in this case is the orthorhombic O-phase. Changes in the coordinates and occupancies of the Wyckoff positions are related to the three types of structural changes mentioned above. Special values of the site occupancy parameters (and lattice parameters) will correspond to changes in crystal symmetry that will follow subgroup/supergroup paths. Analysis of these paths lead to important information regarding the sequence of phase transitions, possible transient states, interconnections between the structures, and domain interface configurations.

To make this approach valid, two assumptions are required:

- 1) The transformations are diffusionless, i.e., no changes in compositions of phases may occur. The assumption seems to be valid considering the time scale of long-range diffusion as compared the interatomic jumps or displacements required for chemical or displacive ordering respectively;
- 2) The transformations are coherent, i.e., no discontinuities occur by slip or fracture in order to relieve internal stress during the phase transformation.

Both assumptions are likely to hold for the Ti-Al-Nb compositions considered either during sufficiently fast continuous cooling from the high temperature single-phase BCC or B2 field or during the initial stages of isothermal annealing of the metastable quenched-in phase. Experimental microstructural results indicate the occurrence of martensite-type ordering transitions and coherent structures under these conditions. Phase separation involving long-range compositional diffusion will be treated by Bendersky and Boettinger [J. Res. Natl. Inst. Stand. Technol. **98**, 585 (1993)].

In this paper we analyze the possible continuous transformations on cooling in the Ti-Al-Nb system and the expected features of idealized coherent microstructures. The approach here is to see the transformations as a sequence of symmetry reductions, and microstructure as a collection of domains. The microstructural features determined by this analysis will be used for comparison to the actual experimental results of Bendersky and Boettinger based on microstructural studies of three Ti-Al-Nb alloys, mainly by transmission electron microscopy (TEM).

Prediction of the microstructural features relies almost entirely on the known structural and symmetry relations between the highest and lowest symmetry phases. The necessary information

concerning the symmetry relations is contained in the space group tables of the International Tables for Crystallography [27]. Based on this information, maximal group/subgroup symmetry relations between phases will be established in Sec. 2. Each transformation step will be considered as a symmetry change, and the transformation path as sequence of subgroups. The symmetry analysis can preclude certain transformation paths, assist in an interpretation of the observed paths and also predict possible intermediate phases. From the predicted path, domain structures can be anticipated. Such domain structures will consist of a hierarchical distribution of interfaces due to the formation of orientational (twin) and translational (anti-phase domain) variants, (Sec. 3). It is expected that the formation of domain structures will minimize the elastic energy arises due to the coherency of transformation. Therefore, low energy, stress free interfaces (SFI) between orientational domains as well as their mutual arrangement are considered in Sec. 4. In Sec. 5 results from the previous sections will be summarized to show what microstructures are expected to be seen for different transformation paths.

2. Group/Subgroup Relations Between BCC ($\text{Im}\bar{3}\text{m}$), HCP ($\text{P6}_3/\text{mmc}$) and Ordered Orthorhombic (Cmcm) Phases

2.1 Sequence of Maximal Subgroups

The Landau theory of phase transition of first or higher order assumes that the symmetry of the product phase is a subgroup of the parent phase and that the atomic positions of the two structures are closely related by a set of order parameters. Usually the low temperature phase has symmetry lower than the high temperature phase and the decrease in symmetry is known as ordering while an increase in symmetry is known as disordering. The group/subgroup relationship between the parent and product phases need not be maximal.¹ However in this paper, we will search for a sequence of maximal group/subgroup relationships in order to anticipate all possible (but not necessarily occurring) intermediate states. Such a sequence can be obtained using the International Tables for Crystallography [27], where the maximal subgroups and supergroups of all 230 crystallographic space groups are tabulated. Table 1 gives examples of such subgroup tables for (a) the $\text{Im}\bar{3}\text{m}$ space group (e.g.,

of the BCC structure) and (b) the $\text{P6}_3/\text{mmc}$ space group (e.g., of the HCP structure). Examples of the known structures represented by these subgroups are B2 ($\text{Pm}\bar{3}\text{m}$) in the IIa subgroups of $\text{Im}\bar{3}\text{m}$ and DO_{19} ($\text{P6}_3/\text{mmc}$) in the IIc subgroups of $\text{P6}_3/\text{mmc}$.

Table 1. Subgroups and supergroups from the International Tables of Crystallography for $\text{Im}\bar{3}\text{m}$ and $\text{P6}_3/\text{mmc}$ ^a

		(a) $\text{Im}\bar{3}\text{m}$	
Maximal non-isomorphic subgroups		I	[3] $\text{I4/m } 12/\text{m } (\text{I4}/\text{mmm})$
			[3] $\text{I4/m } 12/\text{m } (\text{I4}/\text{mmm})$
			[3] $\text{I4/m } 12/\text{m } (\text{I4}/\text{mmm})$
→		[4]	$\text{I}\bar{1}\bar{3}2/\text{m } (\text{R}\bar{3}\text{m})$
		[4]	$\text{I}\bar{1}\bar{3}2/\text{m } (\text{R}\bar{3}\text{m})$
		[4]	$\text{I}\bar{1}\bar{3}2/\text{m } (\text{R}\bar{3}\text{m})$
		[4]	$\text{I}\bar{1}\bar{3}2/\text{m } (\text{R}\bar{3}\text{m})$
		[2]	$\text{Im}\bar{3}1 (\text{Im}\bar{3})$
		[2]	I432
		[2]	$\text{I}\bar{4}3\text{m}$
→ IIa		[2]	$\text{Pm}\bar{3}\text{m}$
		[2]	$\text{Pn}\bar{3}\text{n}$
		[2]	$\text{Pm}\bar{3}\text{n}$
		[2]	$\text{Pn}\bar{3}\text{m}$
IIb		none	
Maximal isomorphic subgroups of lowest index		IIc	[27] $\text{Im}\bar{3}\text{m } (a' = 3a, b' = 3b, c' = 3c)$
Minimal non-isomorphic supergroups		I	none
		II	[4] $\text{Pm}\bar{3}\text{m } (2a' = a, 2b' = b, 2c' = c)$
		(b) $\text{P6}_3/\text{mmc}$	
Maximal non-isomorphic subgroups		I	[2] P6_3222
			[2] $\text{P6}_3/\text{m}11(\text{P6}_3/\text{m})$
			[2] $\text{P6}_3\text{mc}$
			[2] $\text{P}\bar{3}\text{m}1$
			[2] $\text{P}\bar{3}1\text{c}$
			[2] $\text{P}\bar{6}\text{m}2$
			[2] $\text{P}\bar{6}2\text{c}$
→		[3]	$\text{Pm}\text{mc } (\text{Cmcm})$
		[3]	$\text{Pm}\text{mc } (\text{Cmcm})$
		[3]	$\text{Pm}\text{mc } (\text{Cmcm})$
IIa		none	
IIb		[3]	$\text{H6}_3/\text{mmc } (a' = 3a, b' = 3b) (\text{P6}_3/\text{mcm})$
Maximal isomorphic subgroups of lowest index		→ IIc	[3] $\text{P6}_3/\text{mmc } (c' = 3c); [4] \text{P6}_3/\text{mmc } (a' = 2a, b' = 2b)$
Minimal non-isomorphic subgroups		I	none

^a (a) the $\text{Im}\bar{3}\text{m}$ space group of the BCC structure and (b) the $\text{P6}_3/\text{mmc}$ (of both simple HCP and ordered DO_{19}) hexagonal structures. Different types of subgroups are listed according to: I—no change of translations; IIa—decentering; IIb—enlarging the conventional cell; IIc—no change of the group type. [x]—index of the subgroup which gives the number of variants.

¹ A subgroup H of space group G is called a maximal subgroup of G if there is no subgroup L of G such that H is a subgroup of L , i.e., $G > L > H$ [27].

Often there is no apparent subgroup relation between parent and product phases. Examples are found for transitions between structures with cubic and hexagonal symmetry, like the phases in the Ti-Al-Nb system. Here the non-coinciding 3-fold $\langle 111 \rangle$ cubic and 6-fold $[0001]$ hexagonal symmetry axes preclude such a relation. Usually transformations between two phases which do not have a group/subgroup relation are considered reconstructive and not treated by the Landau approach. A connection between symmetries can be restored in some cases by introducing an intermediate structure with space group G_t that is either a supergroup of both structures, G_1 and G_2 , or a subgroup of both structures [28]. When G_t is a supergroup (also called a paraphase in [28]), it is at least a group union of the G_1 and G_2 groups and might not necessarily exist. Such is the case for the BCC and HCP phases considered here which already have very high symmetry. However a subgroup, G_t can always

be found (and not necessarily the trivial group $P1$) as the intersection group of G_1 and G_2 . In particular, for the disordered BCC and HCP phases with $Im\bar{3}m$ and $P6_3/mmc$ space groups and an orientation of unit cell axes according to the Burger's relationship (parallel close packed directions $[111]_c//[11\bar{2}0]_h$ and planes $(110)_c//(0001)_h$), the intersection group G_t is the orthorhombic $Cmcm$, with its c -axis parallel to the $[110]_c$ direction.

The $Cmcm$ space group (with appropriate choice of Wyckoff sites) can represent a structure which is close to HCP but differs in symmetry and relative position of the atoms in the basal planes (Fig. 1). Such an intermediate structure was reported as a martensitic phase in some Ti alloys [29]. The $Cmcm$ structure can also be considered as the BCC structure distorted by shuffles (relative shifts) of the $(110)_c$ planes. In this case the $Cmcm$ group could have been found procedurally by taking the intersection of the cubic symmetry and the symmetry

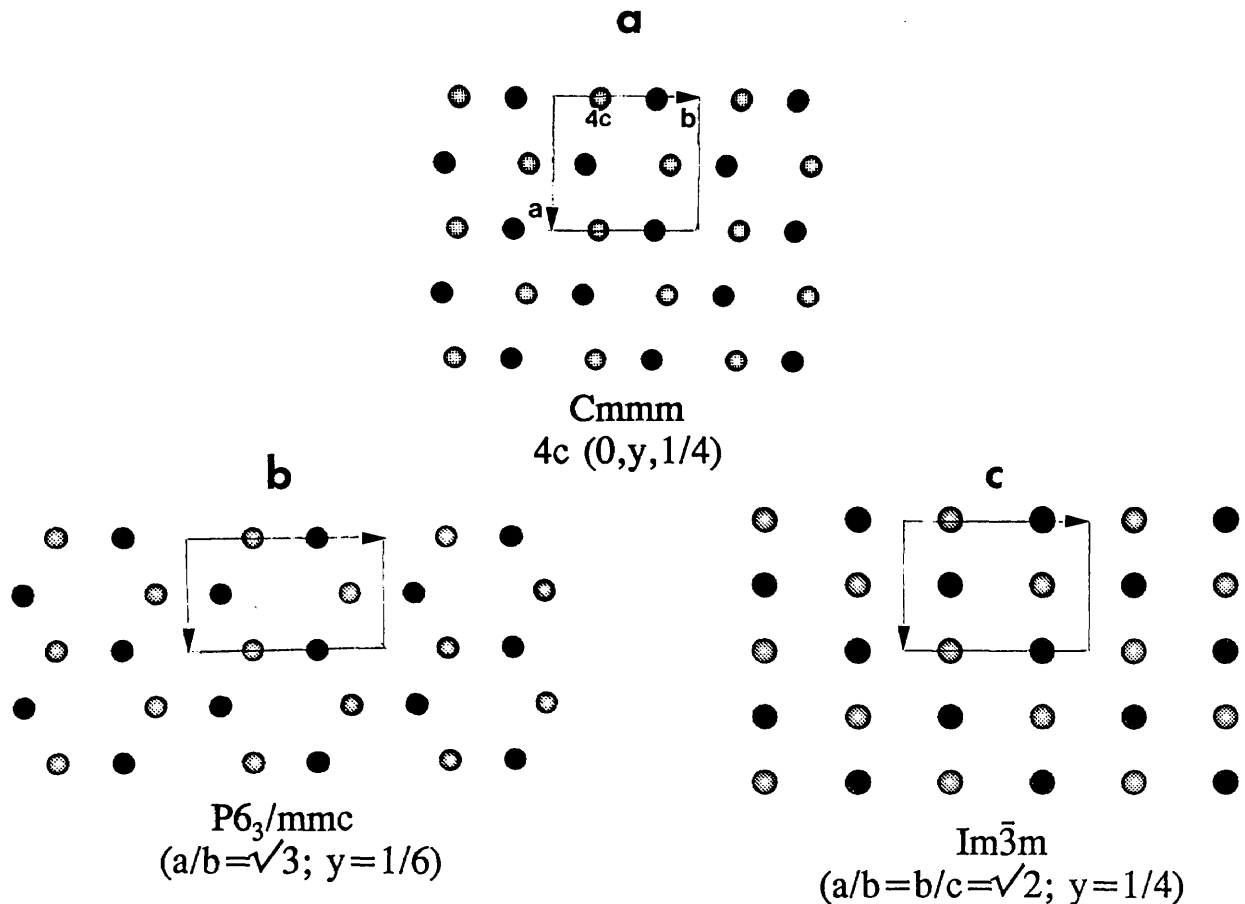


Fig. 1. The $Cmcm$ space group is represented by the structure (a) which is close to both the HCP (b) and BCC (c) but nevertheless different in symmetry and the relative positions of their basal planes. The structures are shown in projections along their $[001]$ (a, b) and $[110]$ (c) directions. Black and white shades represent two neighboring layers of atoms.

of the shuffle displacement wave (mmm point group symmetry for the (110)[$\bar{1}10$]-type shuffle [30,31]). Such symmetry can be locally present in the premartensitic tweed states of quenched BCC or BCC-based structures, which are also known to have the (110)[$\bar{1}10$]-type soft phonon modes (tweed BCC).²

Sequences of maximal subgroups were found that connect the highest symmetry cubic and hexagonal space groups to the low symmetry orthorhombic “intersection” space group (Fig. 2). This sequence includes all known equilibrium phases observed in alloys near the Ti₃Al-Nb₃Al section with less than 30 at% Nb. The figure includes sequences along disordered (BCC) and ordered (B2) branches of the high temperature phases. In the figure the space groups are connected to each other with arrows indicating

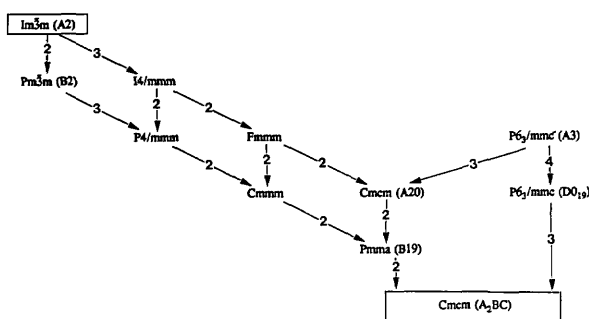


Fig. 2. Subgroup/supergroup symmetry relations between the high symmetry $Im\bar{3}m$ (BCC) and the lower symmetry orthorhombic $Cmcm$ (Ti₂AlNb) space groups. Space groups are connected to each other with arrows pointing in the direction of a decrease in symmetry. The number shown in square brackets next to each arrow is the index of symmetry reduction. Vertical arrows are used to indicate changes in symmetry due to displacive ordering. Angled arrows indicate that the difference in symmetry is due to changes in atomic site occupancy (chemical ordering).

² The use of an intersection group to create continuity of group/subgroup relations has been successfully used in a study of the formation of ω -type phases from a B2 high-temperature phase in a different region of the Ti-Al-Nb system containing 37.5 at% Al and 12.5 at% Nb [32]. In this case the 111 shuffle displacement wave of the omega transition has the cylindrical ∞h symmetry (for coinciding wave and polarization vectors) [30]. The intersection point group of the $m\bar{3}m$ (BCC) and the ∞h (with the mirror plane h parallel to one of the $\langle 111 \rangle_c$ directions) has the trigonal $\bar{3}m$ point group symmetry. The $P\bar{3}m1$ space group ($\bar{3}m$ point group) is obtained from the intersection of space groups of the two stable phases, the high-temperature B2 ($Pm\bar{3}m$) and the low-temperature hexagonal $B8_2$ ($P6_3/mmc$). The structure with the trigonal $P\bar{3}m1$ symmetry was indeed observed as an intermediate state in the transformation path.

symmetry decrease. The numbers shown are the indices of symmetry reductions between two neighboring subgroups (the index of a subgroup is the ratio of the number of symmetry elements in a group to that of the subgroup). These integers give the number of lower symmetry variants (domains) that would be possible if a transition from high to the low symmetry occurred. Inclined arrows indicate symmetry changes due to atomic site (Wyckoff) position changes leaving the occupancy fixed, i.e., displacive ordering. Vertical arrows indicate symmetry changes due primarily to changes in atomic site occupancy, i.e., chemical ordering. Slight adjustments of site positions and occupancies due to the new atomic environments will accompany the chemical and displacive ordering respectively. As described in Sec. 3, one possible transformation sequence for the formation of the lowest symmetry orthorhombic phase from BCC will involve symmetry increase (supergroup formation) from the A20 structure to the A3 structure. In this case no new variants are formed.

2.2 Intermediate Subgroups and Their Corresponding Structures

In addition to the space groups of the Ti-Al-Nb equilibrium phases, A2(BCC): $Im\bar{3}m$, B2: $Pm\bar{3}m$, A3(HCP): $P6_3/mmc$, DO₁₉: $P6_3/mmc$ and O-phase (Ti₂AlNb: $Cmcm$), several other space groups must be introduced in order to keep the subgroup relation maximal (Fig. 2). Crystallographic structures corresponding to the space groups in Fig. 2 are shown in Figs. 3 and 4 (with occupancies relevant for the ternary Ti-Al-Nb alloys). These figures assume an atom to atom correspondence between the structures. In Fig. 3 all of the structures are presented in a common projection normal to their close-packed planes. Frames of both the largest unit cell (of the O-phase) and of the particular crystal structure unit cells are also shown. Analysis of the intermediate structures lead to the following details.

The $I4/mmm$ and $Fmmm$ structures (obtained from the disordered BCC, $Im\bar{3}m$) and the $P4/mmm$ and $Cmmm$ structures (obtained from the ordered B2, $Pm\bar{3}m$) represent homogeneous strain of the cubic lattice. The $I4/mmm$ (Wyckoff position 2a) and $P4/mmm$ (Wyckoff positions 1a and 1d) are tetragonally distorted along the cubic $\langle 100 \rangle$ direction. The $Fmmm$ and $Cmmm$ are structures with different distortions along two orthogonal cubic $\langle 011 \rangle$ directions (with Wyckoff positions 4a and 2a, 2c, respectively, and a doubled unit cell, recentered

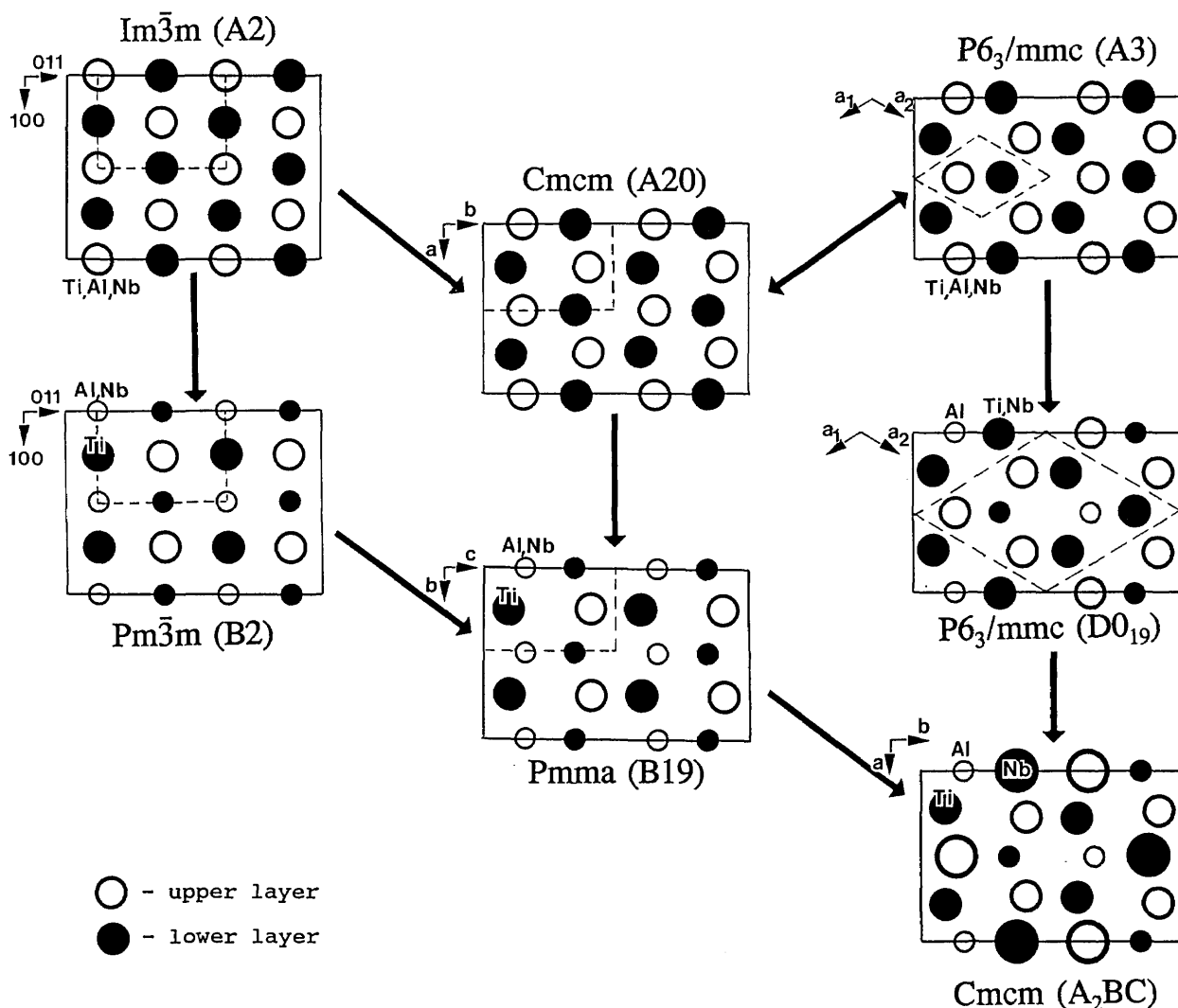


Fig. 3. Structures corresponding to the Fig. 2 subgroup sequence, as viewed along the $[001]_o$, $([011]_c)$ direction. Frames of the largest unit cell (of the O-phase) and of each particular crystal structure are drawn. Increasing size circles represents Al, Ti, and Nb atoms, respectively. Filled and empty circles correspond to different parallel layers of atoms.

and rotated by 45° ($a' = a + b$; $b' = a - b$). The homogeneous strains of orthorhombic symmetry do not change the number of atoms per primitive cell—there remains one atom/cell for the disordered and two atoms/cell for the ordered structures (Fig. 4).

The overall orthorhombic distortion of the cubic structure, if not supported by ordering, is most probably unstable for materials with simple metallic bonding. Therefore, these structures are not expected to exist as metastable states but rather represent a homogeneous strain accompanying (and selecting the orientation of) the subsequent symmetry reduction by shuffle displacement (from

$Fm\bar{3}m$ and $Cmmm$ to $Cmcm$ and $Pmma$, respectively).

Structures corresponding to the $Cmcm$ and $Pmma$ space groups are known in the literature as the Strukturbericht A20 (α -U prototype) and B19 (AuCd prototype), respectively. These structures can be obtained by heterogeneous shuffles of pairs of $(110)_c$ planes of either disordered or ordered cubic structure [corresponding to either 100 or 010 planes of the $Fm\bar{3}m$ and $Cmmm$, respectively (Fig. 4)]. The amplitude of the shuffle displacement wave is reflected in the parameters of the y coordinate of Wyckoff positions: $4c$ $(0, y, 1/4)$ for the $Cmcm$ structure and $2e$ $(1/4, y_1, 0)$; $2f$ $(1/4, y_2, 1/2)$ for $Pmma$. The

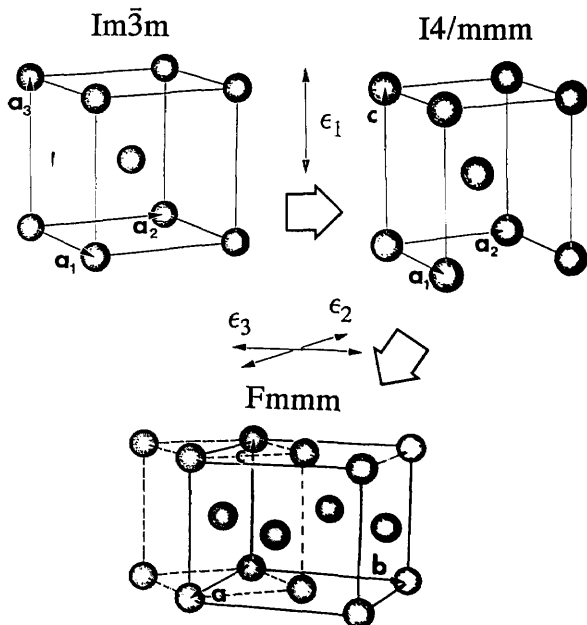


Fig. 4. Space groups and structures representing homogeneous strain distortion of the cubic lattice (a). (b) The $I4/mmm$ and $P4/mmm$ are structures of tetragonal distortion along cubic $\langle 100 \rangle$ (with Wyckoff positions $2a$ and $1a, 1d$, respectively). (c) The $Fmmm$ and $Cmmm$ are structures with orthorhombic biaxial distortion along orthogonal cubic $\langle 011 \rangle$ directions (with Wyckoff positions $4a$ and $2a, 2c$, respectively, and a doubled size unit cell).

symmetry changes do not depend on the size of the displacement. The effect of the shuffles on the disordered $Fmmm$ (010) is that its mirror planes are changed into diagonal glide planes, and all two-fold axes disappear, as shown in Fig. 5 which compares the symmetry elements of these two space groups. The $Cmcm$ structure (or equivalently $Amam$ for the $Fmmm$ coordinate system) has a shifted coordinate origin at either $0, -1/4, -1/4$ or $0, 1/4, 1/4$ (in order to have coincidence of common symmetry elements as shown in Fig. 5). Similarly, for the ordered $Cmmm$ (010) mirror planes and two-fold axes disappear, and the symmetry became $Pm\bar{m}$ (or conventional $Pmma$ [27] with a permutation of the b and c axes). A new coordinate origin of the $Pmma$ is also at $\pm 1/4, 0, 1/4$.

The two origins correspond to two translational variants, with a $(0, 1/2, 0)$ displacement vector. Formally, from the maximal subgroup relations

[27], the translational variants are the result of a lattice decentering. Structurally, the formation of the two variants can be described by shuffle displacement waves that are out of phase by a half period in opposite directions. Because of the displacive nature of ordering, a translational interface between them has a stacking fault nature with atomic distances different from the bulk material. We will discuss details of the interface structure later.

For some special values of Wyckoff positions (y coordinates) and/or of lattice parameters, a structure can degenerate into a structure of higher symmetry. Such a higher symmetry structure, the hexagonal $P6_3/mmc$ (Fig. 3), occurs for the disordered $Cmcm$ when the shuffles are such that Wyckoff position parameter y is $1/3$ and the ratio of lattice parameters, b/a , is $\sqrt{3}$. For the ordered orthorhombic $Pmma$ such a symmetry increase by displacement is precluded by the chemical order inherited from the B2. The disordered hexagonal $P6_3/mmc$ is expected to be more stable than the disordered orthorhombic $Cmcm$; in a hard sphere approximation $P6_3/mmc$ has higher entropy (due to its higher symmetry) while interaction energies are comparable. No thermodynamic barrier for the $Cmcm$ (A20) to $P6_3/mmc$ (A3) transition is expected, and therefore the disordered $Cmcm$ structure is believed to be unstable. This conclusion cast doubts on the existence of the truly disordered orthorhombic martensite [29]. (Nevertheless disordered $Cmcm$ (A20) structures are known for U, Am, Ce, Ga with nonspherical electron densities). Conversely, the $Pmma$ structure (B19) could well be a stable or a metastable phase and exist as a transient state. Indeed numerous B19 phases are known in different systems as either metastable (martensitic) or stable phases, e.g., AuCd and NiTi.

The structure with the lowest symmetry, the O-phase, also has the $Cmcm$ space group and ternary ordering on three Wyckoff positions, $4c_1$, $4c_2$, and $8g$. The O-phase translations on basal $(001)_O$ plane are twice that of the binary ordered $Pmma$ (B19). The structure can be obtained by ordering either $Pmma$ (B19) or $P6_3/mmc$ (DO_{19}). The DO_{19} structure itself can be obtained by binary ordering of the disordered HCP (A3) and could be in an intermediate metastable state.

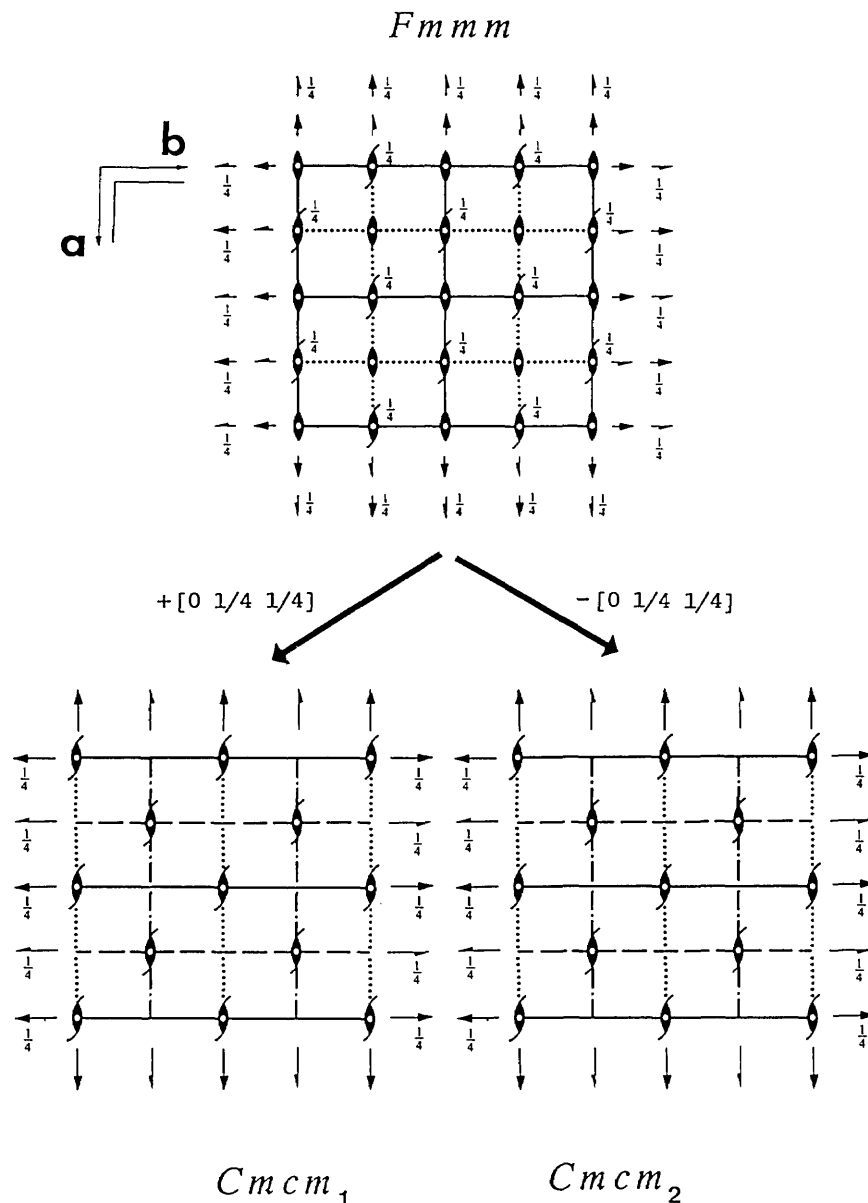


Fig. 5. Comparison of the space-group diagrams of $Fm\bar{m}m$ and two translational variants of $Cm\bar{c}m$. In order to have coincidence of common symmetry elements of these two space groups, the $Cm\bar{c}m$ diagrams must have a coordinate origin shifted to either $0, -1/4, -1/4$ or $0, 1/4, 1/4$. The translation vector between two $Cm\bar{c}m$ variants is $[0\ 1/2\ 1/2]$.

2.3 Description of Structures as Special Cases of the Lowest Symmetry $Cm\bar{c}m$

To summarize, the structures from the group/subgroup sequence can be described in terms of the lowest symmetry $Cm\bar{c}m$ space group corresponding to the Ti_2AlNb phase. The orthorhombic structure has three Wyckoff positions, $4c_1(0, y_1, 1/4)$, $4c_2(0, y_2, 1/4)$ and $8g(x_3, y_3, 1/4)$. Special values of the Wyckoff coordinates, the site occupancies,

and the ratios of the orthorhombic lattice parameters can describe all the structures. The results are summarized in Table 2 where the space groups, Strukturbericht name, prototypes, restrictions on lattice parameters (if any), occupancies (general values and measured values for Ti, Al, Nb) and coordinates of the Wyckoff sites are presented.

Table 2. Description of various phases based on common sites in the Cmc₂m space group

Structure	Lattice Conditions	Occup.	Wyck.	x	y	z
Ti ₂ AlNb, HgNa, Cmc ₂ m	$y_1 = 0.163; y_2 = 0.623$ $y_3 = 0.904; x_3 = 0.231$	A	4c ₁	0	y ₁	1/4
		B	4c ₂	0	y ₂	1/4
		C	8g	x ₃	y ₃	1/4
Ti ₃ Al, DO ₁₉ Ni ₃ Sn, P6 ₃ /mmc	$b/a = \sqrt{3}$	A	4c ₁	0	1/6	1/4
		B	4c ₂	0	2/3	1/4
		B	8g	1/4	11/12	1/4
α Ti, A3 Mg, P6 ₃ /mmc	$b/a = \sqrt{3}$	A	4c ₁	0	1/6	1/4
		A	4c ₂	0	2/3	1/4
		A	8g	1/4	11/12	1/4
Ti-Nb, A20 α U, Cmc ₂ m	y ₁ = 0.1	A	4c ₁	0	y ₁	1/4
		A	4c ₂	0	1/2+y ₁	1/4
		A	8g	1/4	3/4+y ₁	1/4
Ti-Ni, B19 AuCd, Pm ₃ m(Pmma)	y ₁ = 0.156 y ₂ = 0.906	A	4c ₁	0	y ₁	1/4
		A	4c ₂	0	1/2+y ₁	1/4
		B	8g	1/4	y ₂	1/4
β Ti, A2 W, Im $\bar{3}$ m	$b/a = \sqrt{2}$ $c/a = \sqrt{2}/2$	A	4c ₁	0	1/8	1/4
		A	4c ₂	0	5/8	1/4
		A	8g	1/4	7/8	1/4
TiNi, B2 CsCl, Pm $\bar{3}$ m	$b/a = \sqrt{2}$ $c/a = \sqrt{2}/2$	A	4c ₁	0	1/8	1/4
		A	4c ₂	0	5/8	1/4
		B	8g	1/4	7/8	1/4

From the schematic representation of the data in Fig. 3 one can visualize the transformation sequence as a continuous change of atomic sites occupancies and positions within the framework of the O-phase. Regardless of whether the transformations occur by a continuous mechanism, the common geometrical description of the known equilibrium phases permits the realization, in principle, of a single thermodynamic potential representing all of the phases as a function of a set of order parameters based on the site positions and occupancies.

3. Transformation Paths, Types and Hierarchy of Domains Interfaces

The formal crystallographic sequence of group/subgroup relations (Figs. 2 and 3) suggests different ways that the coherent phase transformations from the high temperature BCC (Im $\bar{3}$ m) phase might occur in reality. While the direct formation of the lowest symmetry phase by a reconstructive transformation is possible, microstructural evidence presented by Bendersky and Boettinger

suggests the contrary. The transformation proceeds by steps according to the sequence which imply metastable transient phases. Each transient phase may exist over some temperature interval between upper (to the supergroup phase) and lower (to the subgroup phase) critical temperatures (or temperatures of phase instability for 1st order transitions). Each transformation step of the sequence will reduce a crystal of the higher symmetry phase into lower symmetry phase variants (except A20 \rightarrow A3 where an increase of symmetry does not lead to new variants). The orientation and relative translation of the variants will be related to each other by the symmetry operations of the preceding higher symmetry phase that disappeared after the transition. Therefore a hierarchical (in a sense of both symmetry reduction and domain interface distribution) microstructure is expected. Assuming the nucleation of different low symmetry phase variants in each variant of the high symmetry phase and the absence of significant domain coarsening, a hierarchy of microstructural scale is also expected. The transformation sequence can then be recognized by the way in which the variants of the lowest symmetry phase are grouped.

Starting from the A2 (BCC) phase, the lowest symmetry O-phase can be obtained along different transformation paths (different sequences of transformation steps). Using the maximal subgroups relations in Fig. 2 and reasoning about the stability of structures discussed in Sec. 2.2, one finds that following three transformation paths are feasible:

Path 1: $\text{Im}\bar{3}\text{m}(\text{A2}) \rightarrow [12] \rightarrow \text{Cmcm}(\text{A20}) \rightarrow [1]$
 $\rightarrow \text{P6}_3/\text{mmc}(\text{A3}) \rightarrow [4] \rightarrow \text{P6}_3/\text{mmc}(\text{DO}_{19})$
 $\rightarrow [3] \rightarrow \text{Cmcm}(\text{O})$

Path 2: $\text{Im}\bar{3}\text{m}(\text{A2}) \rightarrow [2] \rightarrow \text{Pm}\bar{3}\text{m}(\text{B2}) \rightarrow [12]$
 $\rightarrow \text{Pmma}(\text{B19}) \rightarrow [2] \rightarrow \text{Cmcm}(\text{O})$

Path 3: $\text{Im}\bar{3}\text{m}(\text{A2}) \rightarrow [12] \rightarrow \text{Cmcm}(\text{A20}) \rightarrow [2]$
 $\rightarrow \text{Pmma}(\text{B19}) \rightarrow [2] \rightarrow \text{Cmcm}(\text{O})$

where the numbers in brackets are the number of variants possible after symmetry the change.

The microstructures resulting from these sequences will consist of the same O-phase but with distinctly different hierarchies and types of interfaces. The type of interfaces, either rotational, translational or mixed, is obvious from the group/subgroup relation. Each symmetry reduction has necessarily more than one variant of the low symmetry phase. Variant generating operations and their matrices, g_{ij} , can be obtained with the help of the International Tables for Crystallography [27] from the list of *Symmetry Operations* of the space group, after excluding the symmetry operations of the subgroup listed in the *Maximal subgroups* table (see Table 1).

The number of variants in each transition is equal to the index of the subgroup (square brackets in Fig. 2 and in paths 1–3). For a sequence of transitions the number of lowest symmetry phase variants (with respect to the highest symmetry phase) will be the product of indices for each step. For the transformation, paths 2 and 3, the number of variants is the same; viz., 48 ($2 \times 12 \times 2$ or $12 \times 2 \times 2$). For the transformation path 1 more variants occur; viz., 144 ($12 \times 1 \times 4 \times 3$) because of the hexagonal symmetry present as an intermediate state. The index of 12 in paths 1–3 is the product ($3 \times 2 \times 2$) of indices of the individual maximal subgroups that accomplish the homogeneous distortion and the shuffles between $\text{Im}\bar{3}\text{m}$ and Cmcm or between $\text{Pm}\bar{3}\text{m}$ and Pmma .

The maximal subgroups in [27] (e.g., shown in Table 1) are divided into isomorphic and non-isomorphic subgroup classes. The isomorphic subgroups (IIc) differ from their parent group only by a translation group; i.e., an increased unit cell size (e.g., HCP to DO_{19} ordering which maintains the same rotation group but doubles the unit cell dimensions in the basal plane). The non-isomorphic class is divided into three subclasses. Class IIa, in which the unit cell is decentered, will have translational variants similar to the isomorphic subgroups (e.g., ordering of BCC ($\text{Im}\bar{3}\text{m}$) to $\text{B2}(\text{Pm}\bar{3}\text{m})$). Class IIb, in which the unit cell is decentered *and* enlarged, will also have only translational variants (e.g., ordering in the Fe-Al system of the $\text{B2}(\text{Pm}\bar{3}\text{m})$ to the DO_3 ($\text{Fm}\bar{3}\text{m}$) phase). Therefore variants of these Classes, IIa, IIb and IIc, are purely translational. The third type of non-isomorphic subgroup is Class I (t subgroups), which retain all translation, and have only rotational variants (e.g., transition in the $\text{YBa}_2\text{Cu}_3\text{O}_{7-\delta}$ high- T_c superconductor from the tetragonal $\text{P4}/\text{mmm}$ to the orthorhombic Pmmm superconducting phase). For non-maximal subgroups translational/rotational combinations are possible. In Table 3, the type of interfaces which are created in each group/subgroup transformation step of the transformation paths 1–3 are summarized.

In the case of coherent structure formation, the contacting volumes of the different variants, which form differently oriented or shifted lattices with respect to each other, are known respectively as rotational and translational *domains*. Mixed rotational/translational domains are also possible for transitions with non-maximal subgroup relation. A single rotational variant of a transformation usually has slightly different orientation of axes with respect to its parent than those following the structural correspondence. The orientation depends on the kind of variant of the surrounding domains and the interface orientation. In general, the number and orientation of coexisting domains as well as the configuration of the domain interfaces, i.e., the *domain structure*, depend on the thermodynamics and kinetics of the phase transformation.

Two major factors will effect the morphology and the orientation of equilibrium interfaces—their surface energy and their bulk elastic energy due to the misfit between different variants and between the matrix and different variants. For rotational domains the self-strains generate significant long range strain and one expects elastic energy minimization to dominate the selection of the interface patterns, as described in detail in Sec. 4. For trans-

Table 3. List of interfaces between domains in different group/subgroup transitions. The Class represents type of symmetry reduction [37], the interfaces are described by domain generating symmetry operation (of lowest symmetry)

Group/subgroup	Class of subgroup	Type of interface
$\text{Im}\bar{3}\text{m} \rightarrow \text{Pm}\bar{3}\text{m}$	IIa	translational (APB)
$\text{Im}\bar{3}\text{m} \rightarrow \text{Cmcm}(\text{A20})$	I + I + IIa	rotational (twins of I and II kind), translational with stacking fault mixed twin/translational
$\text{Cmcm}(\text{A20}) \rightarrow \text{P6}_3/\text{mmc}(\text{A3})$	Supergroup	no new interface
$\text{P6}_3/\text{mmc}(\text{A3}) \rightarrow \text{P6}_3/\text{mmc}(\text{DO}_{19})$	IIc	translational (APB)
$\text{P6}_3/\text{mmc}(\text{DO}_{19}) \rightarrow \text{Cmcm}(\text{O})$	I	rotational (compound twins)
$\text{Pm}\bar{3}\text{m} \rightarrow \text{Pmma}(\text{B19})$	I + I + IIa	rotational (twins of I and II kind), translational with stacking fault, mixed twin/translational
$\text{Cmcm}(\text{A20}) \rightarrow \text{Pmma}(\text{B19})$	IIa	translational (APB)
$\text{Pmma}(\text{B19}) \rightarrow \text{Cmcm}(\text{O})$	IIb	translational (APB)

lational domains, (class II subgroup transitions) there is no change of crystal system (e.g., cubic to cubic lattice in the BCC \rightarrow B2 transition), and therefore only dilatational strains are expected. Thus the surface energy, or more precisely its anisotropy, controls the morphology. However, as many examples from ordered alloys show, these surface energies often have weak anisotropy and domain walls are isotropic and wavy. This is especially true for chemical (substitutional or interstitial) ordering [33]. Based on this, wavy isotropic interfaces are expected for the following transitions presented in Table 3: $\text{Im}\bar{3}\text{m} \rightarrow \text{Pm}\bar{3}\text{m}$, $\text{P6}_3/\text{mmc}(\text{A3}) \rightarrow \text{P6}_3/\text{mmc}(\text{DO}_{19})$, $\text{Cmcm}(\text{A20}) \rightarrow \text{Pmma}(\text{B19})$ and $\text{Pmma}(\text{B19}) \rightarrow \text{Cmcm}(\text{O})$. Less clear are two cases of translational domains in the $\text{Im}\bar{3}\text{m} \rightarrow \text{Cmcm}(\text{A20})$ and the $\text{Pm}\bar{3}\text{m} \rightarrow \text{Pmma}(\text{B19})$ transitions as discussed in detail in Appendixes A and B.

4. Equilibrium Structure of Rotational Domains: Interfaces and Their Arrangement

For rotational domains the elastic energy dominates the interfacial energy for sufficiently coarse structures. We will only consider equilibrium features of rotational domain structures which minimize elastic energy while ignoring their interfacial energy. For interfaces with equivalent elastic energy, the interfacial energy, which can be different for different types and orientations of interfaces (even for the same pair of variants), determines the relative stability.

It is convenient to subdivide the elastic problem into two steps. First, we will consider the simplest domain structure—two domains of two different variants. Secondly, using results for the domain pairs, we will discuss the domain structures consisting of more than two domains. The results, first discussed in general terms, will be applied to two transformations in the Ti-Al-Nb system involving rotational domains: cubic to orthorhombic ($\text{Im}\bar{3}\text{m} \rightarrow \text{Cmcm}$, $\text{Pm}\bar{3}\text{m} \rightarrow \text{Pmma}$) and hexagonal to orthorhombic ($\text{P6}_3/\text{mmc} \rightarrow \text{Cmcm}$).

4.1 Pairs of Domains

The most important characteristic which determines a domain structure is *self-distortion*, S_{ij} , or its symmetric part, *self-strain*, e_{ij} . The self-strain is a homogeneous macroscopic strain that accompanies each phase transformation. The inhomogeneous strains associated with shuffles can be neglected since their effects cancel over a few atomic dimensions. Different variants of each transformation are characterized by different self-strain tensors according to different orientations of the crystal axes of the variants, and therefore of the principal axes of the tensor. The self-strain tensors of two different variants, e.g., 1 and 2, are connected by the following relation:

$$e_{ij}(2) = g_{ik}g_{jl}e_{kl}(1), \quad (1)$$

where g_{ik} is the matrix of one of the parent phase space group symmetry operators which are not a part of the space groups of the two variants.

Operating on the self-strain tensor of one variant with these lost symmetry elements generates the self-strain tensors for the other variants. Examples of these matrices for the hex→O-phase and the BCC→O-phase transformations are given in the Appendix A.

In a coherent crystalline system incompatibility of the self-strains on both sides of the interface creates internal stress originating from the interface. Such stress will not arise, and a *stress-free interface* (SFI) will result if

- 1) the interface is planar, and
- 2) the self-strains on both sides are compatible, i.e., no discontinuity of displacements occurs at the interface.

To meet the requirement of compatibility it is necessary and sufficient that the difference between two self-strains can be represented as the symmetric part of a diadic product of two unit vectors, m and n :

$$\Delta e_{ij} = e_{ij}(2) - e_{ij}(1) = \frac{1}{2}s(m_i n_j + n_i m_j) \quad (2)$$

where m_i is a vector normal to the planar interface considered, n_j is a vector orthogonal to the m_i , and s is a scalar measure of self-strain difference [33].

The rotation of the variants necessary to maintain contact between the domains is given as

$$\omega_{ij} = \pm \frac{1}{2}s(m_i n_j - n_i m_j). \quad (3)$$

When the strain difference given in Eq. (2) is combined with the relative rotation of domains given in Eq. (3), a simple shear will describe the relationship between the two domains. The distortion tensor describing this simple shear is either $sn_i m_j$ along a plane with m normal in the direction n or $sm_i n_j$ along the plane with n normal in the direction m . These simple shears are twin shears, and the domains can be considered as twins with two twinning planes, m or n , normal to each other. One of these twinning planes coincides with a mirror plane of the parent crystal structure (which is not a symmetry element of the variants under consideration) and therefore has rational indices. The other one can be a plane with irrational indices in coordinates of the parent crystal. The rational mirror plane corresponds to type I twinning, whereas the second, irrational plane, corresponds to type II twinning [34]. Using a simple two-dimensional example of a square to a rectangle (p4mm to p2mm) transition, Fig. 6 illustrates the operations described above. (Only Type I twinning occur in this example.)

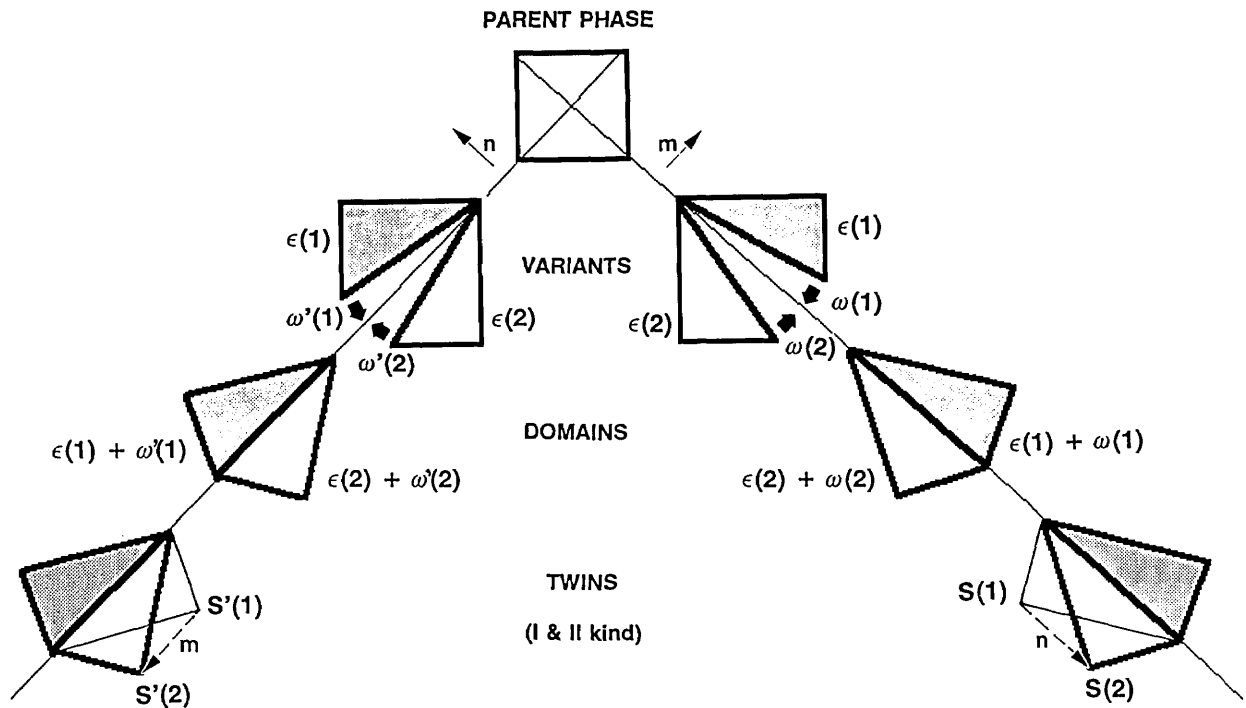


Fig. 6. Two-dimensional example of the square to rectangular (p4mm to p2mm) transition illustrating formation of two pairs of domains, their rotations, strain-free interfaces and description by twinning.

The orientation of SFIs as well as the domain misorientations can be found directly from Eq. (2) in the coordinate system of the principle axes of the strain difference tensor Δe_{ij} [33,35]. For all other coordinate systems it is convenient to transform Eq. (2) by multiplying it by $x_i x_j$, where x_i is an arbitrary vector belonging either to the m ($x_i m_i = 0$) or n ($x_i n_i = 0$) SFI planes to obtain [36]

$$x_i [e_{ij}(2) - e_{ij}(1)] x_j = 0. \quad (4)$$

This quadratic equation splits into the product of two linear equations whose solutions determine the coordinates of two SFI planes. (The absence of a solution of Eq. (4) implies that the difference between the self-strains of the variants can not be represented in the diadic form of Eq. (2), and therefore a domain pair generated by these variants cannot have a SFI.)

Both equivalent equations, Eqs. (2) and (4), were obtained with the assumption that the self-strains are small [33, 36]. However, Eq. (4) can be easily generalized to avoid the small-strain approximation using standard finite deformation analysis. A plane belonging to the parent phase becomes a SFI if any vector x_k in that plane, after being transformed, will have the same length in both variants. In variant (1) the vector x_k becomes $X_i(1) = [\delta_{ik} + S_{ik}(1)]x_k$, where δ_{ik} is a unit matrix, $S_{ik}(1)$ is a self-distortion tensor of the variant 1. The variant (2) transforms the same vector x_k into $X_i(2) = [\delta_{ik} + S_{ik}(2)]x_k$. The equality of the lengths $[X_i^2(1) = X_i^2(2)]$ leads to an equation similar in its form to Eq. (4) but where

$$e_{ij} = \frac{1}{2}(S_{ij} + S_{ji}) + \frac{1}{2}S_{ik}S_{kj} \quad (5)$$

Eq. (5) is a strain tensor commonly used to describe finite deformation and provides an exact definition of self-strain as a symmetric tensor based on the known self-distortion tensor of a transformations, and it includes a quadratic term of the distortion tensor, S_{ij} . For weakly first order and second order ferroelastic-type transformations, the quadratic term can be neglected in the vicinity of transformation because S_{ij} (related to the order parameter) is small. For strongly first order martensitic transformations, with large distortions, the quadratic term can be considerable.

Besides the solutions corresponding to the rational mirror planes in the parent phase, Eq. (4) has solutions that depend on the lattice parameters of the product phases, and therefore yield orientations that are generally irrational and depend on

transformation temperature and the phase compositions. The solutions for orientations of SFIs for 94 different combinations of higher and lower point groups, relevant for ferroelastic transformation, are given by Sapriel by solving Eq. (4) [36]. For the transitions considered in this work, namely for BCC/B2 to orthorhombic/HCP structures [$\text{Im}\bar{3}\text{m}(\text{A}2) \rightarrow \text{Cmcm}(\text{A}20)/\text{P}6_3/\text{mmc}(\text{A}3)$ and $\text{Pm}\bar{3}\text{m}(\text{B}2) \rightarrow \text{Pmma}(\text{B}19)$] and for HCP to orthorhombic [$(\text{P}6_3/\text{mmc}(\text{DO}_{19}) \rightarrow \text{Cmcm}(\text{O-phase}))$], specific forms of Eq. (4) and its solutions are given in Appendix A. For the HCP \rightarrow orthorhombic transformation, there are only symmetric SFIs of the $\{1\bar{1}00\}_h$ and $\{11\bar{2}0\}_h$ types (the irrational solution degenerates into a symmetric one). The SFIs correspond to $\{110\}_o$ and $\{130\}_o$, respectively, when transformed to coordinates of the O-phase. For the BCC \rightarrow orthorhombic (or similarly HCP) transformation, there are three SFIs of the $\{100\}_c$ type, six of the $\{110\}_c$ type, and six irrational $\{hkk\}_c$ types with h/k ratios depending on the lattice parameters of the orthorhombic (or hexagonal) phase. The rational SFIs correspond to $\{021\}_o$ and $\{221\}_o$, respectively, when transformed to coordinates of the O-phase. The $\{hkk\}_c$ -type interfaces in the O-phase coordinates are of the form $\{1, (s-1), 2(s+1)\}_o$ where $s = k/h$. The $\{hkk\}_c$ interfaces, when calculated for the lattice parameters of the DO_{19} or O phases taken from the literature [4], are found to be close to $\{155\}_c$ and $\{144\}_c$, respectively. The pair of orthogonal interfaces between different pairs of variants are summarized in Table 4 where the labeling of the pairs is given according to Fig. A.2.

4.2 Polydomain Structures

Two rotational domains separated by a planar SFI are a unique morphology that avoids long range elastic stress fields. Two domains cannot be bounded by the two conjugate orthogonal SFIs as shown in Fig. 7a, because the corner where these SFIs intersect each other would be a disclination, and therefore a source of a long-range distortion.

The optimal shape of one domain included inside another is a plate with a small thickness to length ratio. (Experimentally the plates usually are found lenticular.) If the wide facets of the plate are SFIs, the stress field would be concentrated only near the plate edge, in a manner similar to a dislocation loop field (Fig. 7b) [35, 37]. This long range field can be reduced if a packet of plate-like domains is formed (Fig. 7c). If the boundaries of the packets (imaginary planes through the plate edges) are aligned

Table 4. List of SFI interfaces for all possible pairs of domain of the O-phase in the $m\bar{3}m \rightarrow mmm$ type transformation. Labeling of variants and interface indexes are given in the cubic coordinates of Fig. A.2. $s = k/h = 2B/(A - C)$

Pair of domains	Interface equation	Interface in Miller indices
1/2	$x = 0;$ $y = 0;$	(1 0 0) (0 1 0)
1/3	$y = z;$ $-2Bx + (C - A)(y + z) = 0;$	(0 1 1) (s 1 1)
1/4	$y = -z;$ $-2Bx + (C - A)(y - z) = 0;$	(0 1 1) (s 1 $\bar{1}$)
1/5	$x = z;$ $-2By + (C - A)(x + z) = 0;$	(1 0 $\bar{1}$) (1 s 1)
1/6	$x = -z;$ $-2By + (C - A)(x - z) = 0;$	(1 0 1) (1 s $\bar{1}$)
2/3	$y = -z;$ $2Bx + (C - A)(y - z) = 0;$	(0 1 1) (s $\bar{1}$ 1)
2/4	$y = z;$ $2Bx + (C - A)(y + z) = 0;$	(0 1 $\bar{1}$) (s $\bar{1}$ $\bar{1}$)
2/5	$x = -z;$ $2By + (C - A)(y - z) = 0;$	(1 0 1) ($\bar{1}$ s 1)
2/6	$x = z;$ $2By + (C - A)(y + z) = 0;$	(1 0 $\bar{1}$) ($\bar{1}$ s $\bar{1}$)
3/4	$x = 0;$ $z = 0;$	(1 0 0) (0 0 1)
3/5	$x = y;$ $-2Bz + (C - A)(x + y) = 0;$	(1 $\bar{1}$ 1) (1 1 s)
3/6	$x = -y;$ $-2Bz + (C - A)(x - y) = 0;$	(1 1 0) (1 $\bar{1}$ s)
4/5	$x = -y;$ $2Bz + (C - A)(x - y) = 0;$	(1 1 0) ($\bar{1}$ 1 s)
4/6	$x = y;$ $2Bz + (C - A)(x + y) = 0;$	(1 $\bar{1}$ 0) ($\bar{1}$ $\bar{1}$ s)
5/6	$y = 0;$ $z = 0;$	(0 1 0) (0 0 1)

parallel to the conjugate SFI plane n of the SFI plane of the individual plates, m , then interference of the edge fields cancels the long-range stress field components. Such plane-parallel packets (also named in the literature as *polytwins* (by analogy with polysynthetic twins, or polydomains) are a typical element of domain morphology.

The polytwin as a whole can be considered as an effective “domain” of second order in a hierarchy of domain structures [33,37]. By analogy domain structures of even higher order can also be con-

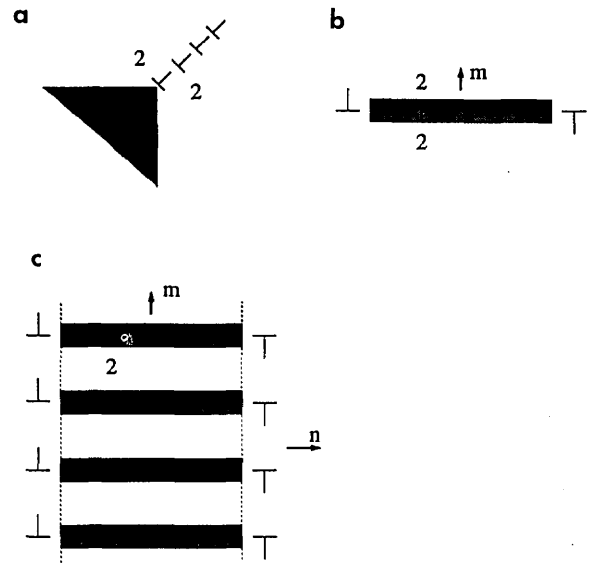


Fig. 7. Schematic drawing of two rotational domains (white and gray shades) separated by planar SFIs and corresponding long range elastic stress fields. (a) Disclination field of a dihedral angle of a domain interface. (b) Dislocation-like field of a single domain inside another domain serving as a matrix. (c) Self-accommodated group of domains with reduced long range field.

structed. Examples of a domain structure of 2nd order for the BCC \rightarrow Ort transition consisting of 3 variants are discussed below and illustrated in Fig. 8.

The pseudo-SFIs between polytwins can be determined by the same Eqs. (4) and (5), where e_{ij} (or S_{ij}) is an *average* self-strain of the polytwin as a whole. For example, the equations for the SFI between the polytwin consisting of domains 1 and 2 and the polytwin consisting of 1 and 3 is

$$x_i [e_{ij}(1,2) - e_{ij}(1,3)] x_j = 0 \quad (6)$$

The average self-distortions $S_{ij}(1,2)$ and $S_{ij}(1,3)$ are expressed through an average distortion of the polytwins

$$S_{ij}(1,2) = (1 - \alpha) S_{ij}(1) + \alpha S_{ij}(2) \quad (7a)$$

$$S_{ij}(1,3) = (1 - \beta) S_{ij}(1) + \beta S_{ij}(3) \quad (7b)$$

where α (or β) is the fraction of domains 2 (or 3) in polytwin (1,2) (or 1,3), and where the distortions $S_{ij}(1)$, $S_{ij}(2)$ and $S_{ij}(3)$ include the supplementary rotations [Eq. (3)] of the domains in the polytwins required for conserving coherency.

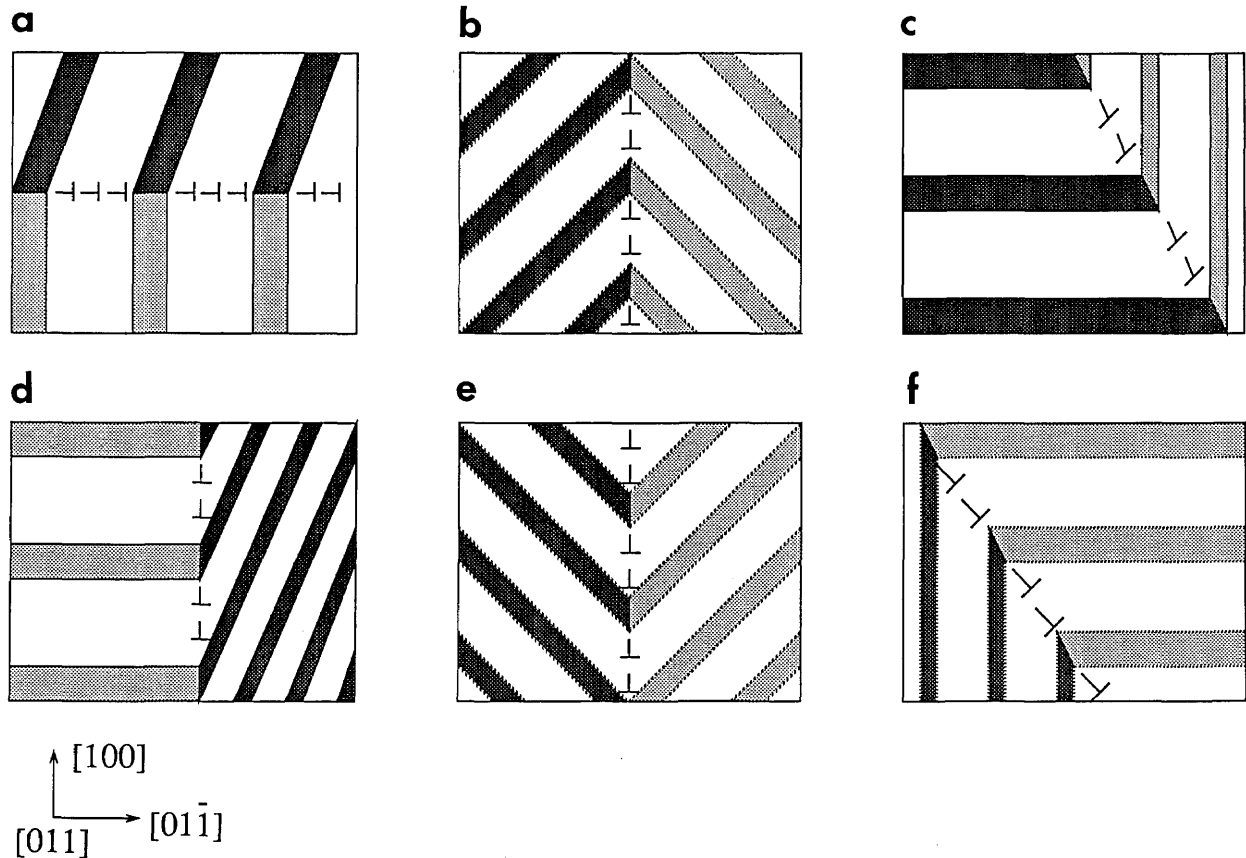


Fig. 8. Polydomain structures of two second order polytwin plates composed of different combinations of three rotational variants (white, light and dark shades) of the orthorhombic phase as seen in the $[011]_c$ direction. The domain interfaces are either SFI (twin boundaries) or low-angle boundaries (dislocation walls). Continuous lines represent “edge-on” planes while dotted lines are inclined planes. Possible combinations of three variants are: (a) $(1,3)/(2,3)$, $(2,4)/(1,4)$; (b) $(4,5)/(2,5)$, $(2,6)/4,6$, $(3,5)/(1,5)$, $(1,6)/(3,6)$; (c) $(1,2)/(2,4)$, $(3,4)/(2,4)$, $(1,2)/(1,3)$, $(3,4)/(1,3)$; (d) $(1,2)/(2,3)$, $(1,2)/(1,4)$, $(3,4)/(2,3)$, $(3,4)/(1,4)$; (e) $(4,6)/(2,6)$, $(1,6)/(3,6)$, $(1,5)/(3,5)$, $(4,5)/(2,5)$; (f) $(1,2)/(2,4)$, $(3,4)/(1,3)$. (The labeling of the variants follows Fig. A.2.)

In general, to determine the pseudo-SFI between polytwins, the fractions α and β must be known. If $\alpha = \beta$, the stress free boundary between polytwin (1,2) and polytwin (1,3) may run along the SFI between domains 2 and 3. For that, a line of intersection of the 1,2 SFI and the 1,3 SFI has to belong to the 2,3 SFI. For the BCC \rightarrow ORT transformation there are three different interfaces of this type between polytwins consisting of 3 types of domains: along $\{100\}_c$, $\{110\}_c$ and $\{h11\}_c$ according to the three possible orientations of the SFIs between the domains given in Table 4. Using Table 4 it is not difficult to find all possible second order polydomain morphologies for the $\alpha = \beta$ case. Such morphologies for three-variant structures are represented in Fig. 8. It is very likely that such structures with $\alpha = \beta$ correspond to a minimal energy.

While interfaces between polytwins that satisfy Eq. (6) have no long-range stress field, they do have microstresses distributed in the packet boundary. Even in the case of good matching ($\alpha = \beta$), the rotation between different domains causes microstresses which can be described as fields from disclination dipoles. These microstresses at the boundary could manifest themselves during annealing as sites for further microstructural change.

The approach of packing first, second, and higher order effective domains can be applied in principle for the analysis of any hierarchy of domain structures. The scale of such hierarchical structures should be determined by the competition between the short-range microstresses distributed in the packet boundaries that tend to disperse the structure and the effective interfacial

energy that tends to coarsen the structure.³ The number of the variants in the polydomain structure which are necessary to accommodate the self strain depends on boundary conditions. For a polydomain structure inside an untransformed matrix, the simplest polytwin that has an invariant plane boundary with the matrix is sufficient [39,40]. If the boundary of the region to be transformed is fixed, e.g., it coincides with a grain boundary, minimum elastic energy corresponds to the minimum average self-strain of the region, or zero average shear. This condition can be achieved only when all variants take part in the polydomain structure. The number of the variants determines an internal hierarchy of the polydomain structure.

5. Expected Microstructures and Transformation Paths

The present analysis suggests that three different types of domain structures are possible for a single phase microstructure of the O-phase depending on the transformation path traversed. Paths 1-3 are summarized in the form of subgroup sequences. These paths differ primarily as to whether the hexagonal symmetry phases or the B19 phase occurs at an intermediate stage of transition. The path involving the hexagonal phases (path 1) involves the formation of a supergroup; i.e., the intermediate orthorhombic A20 structure transforms to the hexagonal A3 by pure displacement. In general this is impossible (as a pure displacive transformation) if the parent phase has either long or short range chemical order of a type which would have been required to adjust to form the higher symmetry [41]. Thus path 1 is only possible for alloys quenched from a disordered BCC phase.

For Ti-Al-Nb alloys quenched from a B2 phase field, path 2 is clearly expected. The path is characterized by the presence of the B19 structure as an intermediate stage of transition, which in this case forms by a purely displacive transition from B2.

The B19 phase could also form from an alloy quenched from the disordered BCC field by path 2 or by path 3. This latter path involves the formation of the B19 structure from the orthorhombic A20 by a pure ordering reaction between Ti and Al/Nb. Experimentally, evidence for the occurrence of one of the three paths can be obtained with microstructural information for the transient existence of B19 or A3 phases in the final O-phase domain structure. In alloys near the Ti_3Al-Nb_3Al section of the ternary system, the tendency towards B2 order in the high temperature BCC phase is strongest for alloys near Ti_2AlNb because the two Wyckoff sites of the B2 are known [21] to be filled with Ti and a mixture of Al and Nb. Thus paths to the O-phase involving the B19 phase are most likely for alloys with Nb contents around 25 at%, while the path to the O-phase involving the hexagonal phase is expected for lower levels of Nb.

The microstructural development for the three paths is depicted in Fig. 9, starting from a large grain single phase BCC and ending with single phase orthorhombic. It is assumed that the interface configuration does not change significantly after formation at each stage of the transformation. All three paths, in their first stages, have similar microstructures composed of orthorhombic phase domains (either disordered Cmc(A20) for paths 1 and 3 or ordered Pmma(B19) for path 2). According to the discussion in Sec. 4, the domains will form a polytwin morphology with SFIs parallel to either $\{100\}_c$, $\{110\}_c$ or conjugate $(hkk)_c$ planes. In path 2, the BCC→B2 ordering precedes the formation of the orthorhombic phase but does not influence the formation and morphology of the polytwin structure. The APBs due to this ordering (curved lines) separate either interconnected or closed volume domains and may be found continuously crossing the polytwin domains. If path 2 starts from the B2 phase, such APBs will be absent.

Inside the polytwin plate-like domains, as Fig. 9 shows, anisotropic planar interfaces (schematically represented as rectangles, or straight lines for interfaces connected to twin boundaries) separate two translational domains resulting from antiphase shuffles (formally due to the Fmmm→Cmc and Cmmm→Pmma symmetry changes). The anisotropy is expected because of the stacking fault nature of the interface structure. Because of the anisotropy the interfaces are distinct for each orthorhombic phase variant orientation.

³ As shown by [33,35,37], similar hierarchical structures can also be formed by domains consisting of different phases. For example, the structure morphologically similar to the 3-domain structure in Fig. 8 can be created by incorporating two domains of the O-phase inside of which there is one domain of the hexagonal DO_{19} phase (domain 1). The geometry of such a heterophase structure will be analyzed in Bendersky and Boettinger [J. Res. Natl. Inst. Stand. Technol. 98, 585 (1993)].

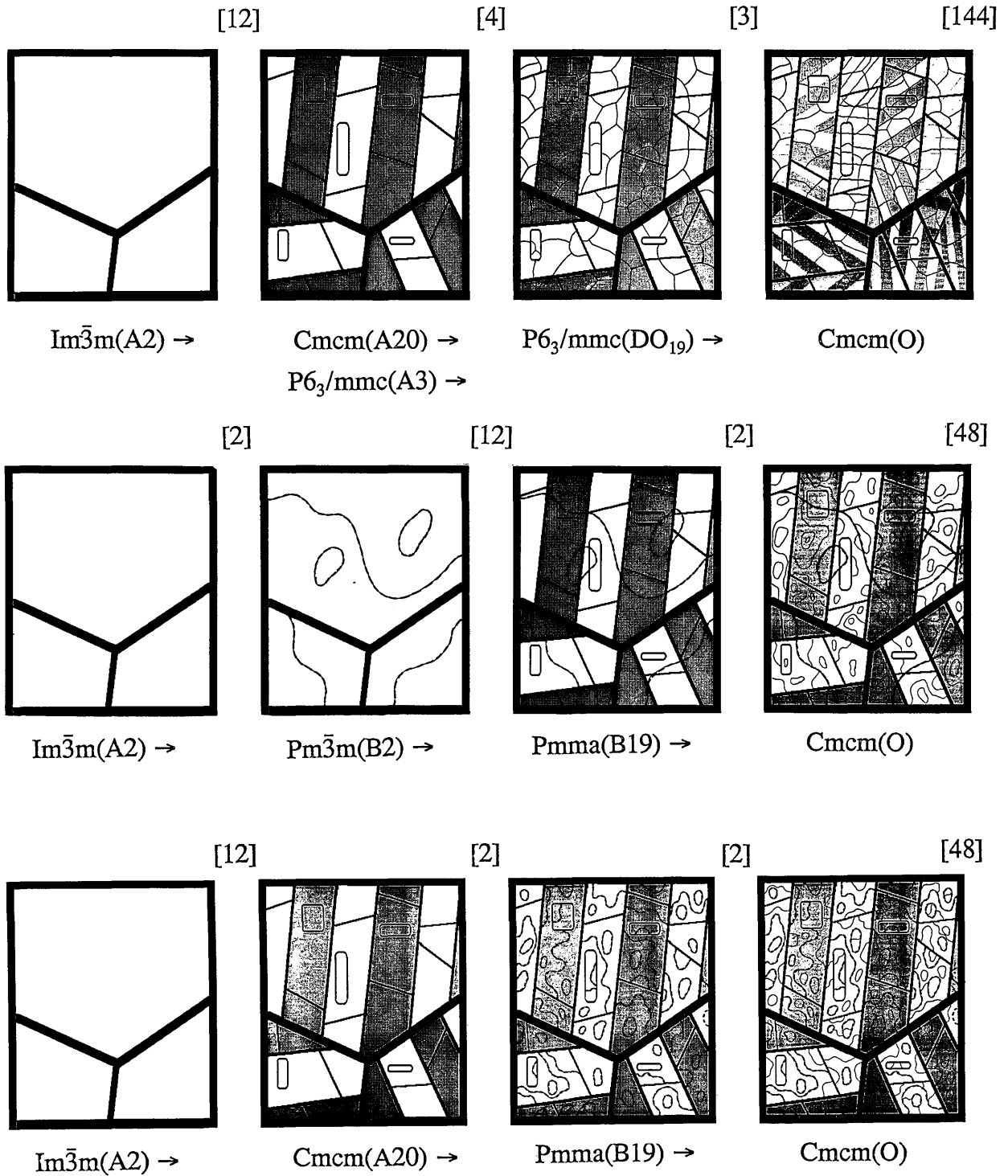


Fig. 9. Graphical representation of the microstructural development for the three paths, starting from a large grain single phase BCC and ending with single phase orthorhombic. For the figure it is assumed that the interface configuration does not change significantly after formation at each stage of the transformation.

After the formation of the polytwin structure by displacive ordering, the next step in all three transformation paths is chemical ordering. For path 1 the ordering involves two steps. First, $A3 \rightarrow DO_{19}$ ordering of the hexagonal lattice (between Al and Ti/Nb) results in a four translational domain structure with isotropic interfaces shown in Fig. 9 as thin lines with triple junctions. Some of the interfaces are shown to coincide with previously formed translational interfaces. These coinciding segments will have a structure where changes in both atomic environment and distances are combined. Secondary ordering ($DO_{19} \rightarrow O$ -phase) between Ti and Nb results in a second polytwin domain structure with planar interfaces running through the DO_{19} APBs, which are not effected by the secondary ordering. The interfaces in the same primary plate can have different orientations (either orthogonal or 60° rotated) as discussed in Appendix A and shown in Fig. 9.

In path 2, the ordering ($B19 \rightarrow O$ -phase) between Al and Nb results in a two domain structure, with isotropic interconnected or closed interfaces. Due to the presumed lower temperature of transformation for this stage, the size of these antiphase domains is shown in Fig. 9 smaller than those from the first $BCC \rightarrow B2$ ordering. If the path starts from the B2 phase only the second type of antiphase domains will occur in the final microstructure.

In path 3 there are two steps of chemical ordering—the first one between Ti and Al/Nb atoms

($A20 \rightarrow B19$) and the second one between Al and Nb ($B19 \rightarrow O$ -phase)—resulting in isotropic interfaces. Again, due to the difference in the presumed temperature of transformation, the size of these antiphase domains may be different. However the difference, as it is shown in Fig. 9, is less than for path 2, and this is the only difference in these two final microstructures.

6. Appendix A. SFIs for the $P6_3/mmc$ (DO_{19}) \rightarrow $Cmcm(O)$ ($6/mmm \rightarrow mmm$) Transition

The structural relation between the phases (o—orthorhombic; h—hexagonal) gives the following lattice correspondence: $a_0 = a_{1h}$; $b_0 = a_{1h} + 2a_{2h}$; $c_0 = c_h$. Fig. A.1 shows stereographic projections of the point groups of the hexagonal and of the orthorhombic phase variants, according to the lattice correspondence. When the symmetry elements of a pair of variants are compared, we find a set of two orthogonal mirror planes which belong to the parent phase but not to the pair considered, e.g., for variants 2 and 3 in Fig. A.1, the set of lost mirror planes is $x = 0$ and $y = 0$. Similarly, for the $1/2$ and $1/3$ pairs of domains the sets are $y/x = \tan 30^\circ = \sqrt{3}/3$, $y/x = \tan 120^\circ = -\sqrt{3}$ and $y/x = \tan 60^\circ = \sqrt{3}$, $y/x = \tan 150^\circ = -\sqrt{3}/3$, respectively. Being mirror planes, and therefore twinning planes, the three sets are planar SFIs running parallel to the z -axis.

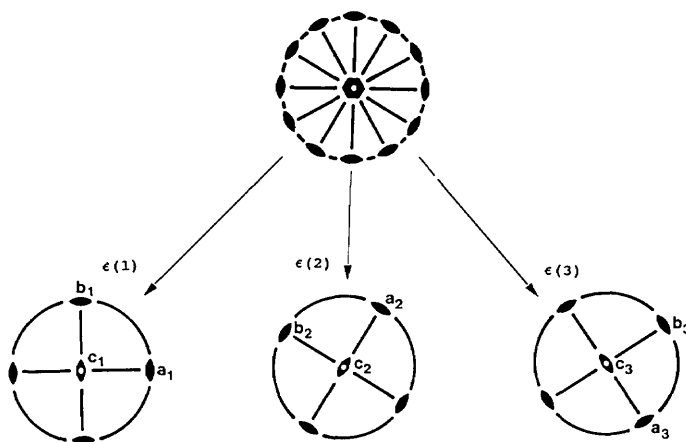


Fig. A.1. Stereographic projections of the point groups of the hexagonal ($6/mmm$) and of the orthorhombic phase variants (mmm 's), according to their lattice correspondence. When the symmetry elements of a pair of variants are compared, a set of two orthogonal mirror planes is found that belong to the parent phase but not to the pair considered.

The same results can be obtained by solving Eq. (4). For this purpose, the self-strain tensor of the three variants must be first determined. For variant 1 in Fig. A.1, the self-strain tensor will be

$$e_{ij}(1) = \begin{vmatrix} e_1 & 0 & 0 \\ 0 & e_2 & 0 \\ 0 & 0 & e_3 \end{vmatrix}, \quad (\text{A.1})$$

where

$$e_1 = a + a^2/2; \quad e_2 = b + b^2/2; \quad e_3 = c + c^2/2.$$

with

$$a = \frac{a_0 - a_h}{a_h}; \quad b = \frac{b_0 - \sqrt{3}a_h}{\sqrt{3}a_h}; \quad c = \frac{c_0 - c_h}{c_h}.$$

The self-strain tensor for the other two variants will be obtained using Eq. (1). The variant generating symmetry operation in that case is chosen to be the three-fold anti-clock-wise rotation ($g_{ij} = 3^-$), so that $e_{ij}(3) = 3^- 3^- e_{ij}(1)$ and $e_{ij}(2) = 3^- 3^- e_{ij}(3)$ (see Fig. A.1). In order to do calculations in orthogonal coordinates, the matrix of the three-fold rotation must be presented in the same coordinates. It is found as

$$3_{ij}^- = \begin{vmatrix} -1/2 & -\sqrt{3}/2 & 0 \\ \sqrt{3}/2 & -1/2 & 0 \\ 0 & 0 & 1 \end{vmatrix}. \quad (\text{A.2})$$

After matrix multiplication we find that

$$e_{ij}(3) = \begin{vmatrix} \frac{a}{4} + 3\frac{b}{4} & -\sqrt{3}\frac{a}{4} + \sqrt{3}\frac{b}{4} & 0 \\ -\sqrt{3}\frac{a}{4} + \sqrt{3}\frac{b}{4} & 3\frac{a}{4} + \frac{b}{4} & 0 \\ 0 & 0 & c \end{vmatrix}, \quad (\text{A.3})$$

and

$$e_{ij}(3) - e_{ij}(1) = \frac{\sqrt{3}(b-a)}{4} \begin{vmatrix} \sqrt{3} & 1 & 0 \\ 1 & -\sqrt{3} & 0 \\ 0 & 0 & 0 \end{vmatrix}. \quad (\text{A.4})$$

Equation (4) for the SI interfaces between variants 3 and 1 will be

$$[e_{ij}(3) - e_{ij}(1)]x_i x_j = x^2 - y^2 + \frac{2}{\sqrt{3}}xy = 0$$

or

$$(y - \sqrt{3}x)(y + x/\sqrt{3}) = 0. \quad (\text{A.5})$$

Two solutions for the quadratic equation are $y/x = \sqrt{3}$ and $y/x = -\sqrt{3}/3$ and they do not depend on the parameters a , b , and c . These are the same mirror planes found with the help of the stereographic analysis performed above. Solutions for the other variants can be found similarly, and they are the remaining mirror planes of the 6/mmm with $y/x = \sqrt{3}/3$, $-\sqrt{3}$ (for the 1/2 variants) and $x=0$, $y=0$ (for the 2/3 variants). A pair of variants can be identified unambiguously from their interface orientation.

7. Appendix B. SFIs for the $\text{Im}\bar{3}\text{m}(\text{A2}) \rightarrow \text{Cmcm}(\text{A20})$ and $\text{Pm}\bar{3}\text{m}(\text{B2}) \rightarrow \text{Pmma}(\text{B19})$ ($\text{m}\bar{3}\text{m} \rightarrow \text{mmm}$) Transition

The structural relation between the phases (c—cubic; o—orthorhombic) gives the following lattice correspondence: $\mathbf{a}_0 = \mathbf{a}_{1c}$; $\mathbf{b}_0 = \mathbf{a}_{2c} + \mathbf{a}_{3c}$; $\mathbf{c}_0 = \mathbf{a}_{2c} - \mathbf{a}_{3c}$. According to the lattice correspondence, Fig. A.2 shows the stereographic projections of the point groups and the crystallographic axes of the parent cubic ($\text{m}\bar{3}\text{m}$) and its six subgroup variants of the orthorhombic (mmm) phases. Comparing symmetry elements belonging to a pair of the variants with those of the parent cubic, we can find mirror planes of the parent (but missing in the product variants) that reflect the variants into each other. The mirror planes serve as the SFIs. For a pair of variants sharing the \mathbf{a}_0 axis (1/2, 3/4, and 5/6 pairs in Fig. A.2), there are two orthogonal mirror planes of $\{100\}_c$ type (parallel to the \mathbf{a}_0 axis). For the other pair of variants, not sharing a common

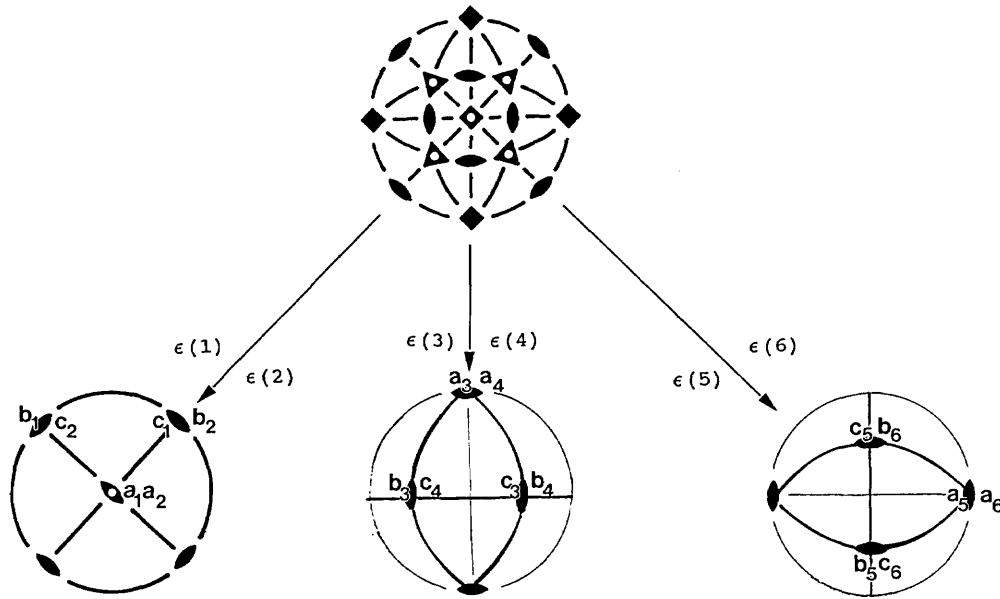


Fig. A.2. Stereographic projections of the point groups and the crystallographic axes of the parent cubic ($m\bar{3}m$) and its six subgroup variants of the orthorhombic (mmm) phases. Comparing symmetry elements belonging to a pair of the variants with those of the parent cubic, mirror planes that reflect the variants into each other can be found.

direction, there is only one such mirror plane, of $\{110\}_c$ type. Orthogonal to the $\{110\}$ plane is either a $\{h\bar{h}k\}_c$ or a $\{h\bar{h}\bar{k}\}_c$ plane, generally of an irrational orientation which depends on the ratio of the lattice parameters. In order to find h and k , Eq. (4) must be solved.

We solve Eq. (4) in the coordinate system of the cubic phase shown in Fig. A.2. First, we find the self-strain tensors of the six variants using the variant generating operators, Eq. (1). All variants can be generated by the mirror plane operations, starting from the first variant:

$$\begin{aligned} e(2) &= m_{100} m_{100} e(1), & e(5) &= m_{10-1} m_{10-1} e(1), \\ e(4) &= m_{011} m_{011} e(1), & e(6) &= m_{010} m_{010} e(5), \\ e(3) &= m_{100} m_{100} e(4). \end{aligned} \quad (B.1)$$

Matrices for the mirror planes are given in Table 11.4 of *The International Tables for Crystallography* [37]. The self-strain tensor for variant 1 (see Fig. A.2) in the coordinates of the variant is

$$e'_{ij}(1) = \begin{vmatrix} a & 0 & 0 \\ 0 & b & 0 \\ 0 & 0 & c \end{vmatrix}, \quad (B.2)$$

where

$$a = \frac{a_0 - a_c}{a_c}, \quad b = \frac{b_0 - \sqrt{2}a_c}{\sqrt{2}a_c}, \quad c = \frac{c_0 - \sqrt{2}a_c}{\sqrt{2}a_c};$$

and a_c, a_0, b_0, c_0 are the lattice parameters of the cubic and the disordered orthorhombic phase (for the ordered O-phase half of their values of a_0 and b_0 should be used).

In order to obtain the $e'_{ij}(1)$ tensor in cubic coordinates, the tensor's axes must be rotated 45° around $[100]_c$, which is obtained by the rotation and permutation matrix

$$\alpha_{ij} = \begin{vmatrix} 0 & m & m \\ 0 & -m & m \\ 1 & 0 & 0 \end{vmatrix}, \quad m = \frac{\sqrt{2}}{2}. \quad (B.3)$$

The tensor $e_{ij}(1)$ in cubic coordinates is then

$$e_{ij}(1) = \alpha_{ik} \alpha_{jl} e'_{kl}(1) = \begin{vmatrix} A & B & 0 \\ B & A & 0 \\ 0 & 0 & C \end{vmatrix}, \quad (B.4)$$

where $A = 1/2(b + c)$; $B = 1/2(c - b)$; $C = a$.
The self-strain tensors for other variants are:

$$e_{ij}(2) = \begin{vmatrix} A & -B & 0 \\ -B & A & 0 \\ 0 & 0 & C \end{vmatrix}, e_{ij}(3) = \begin{vmatrix} A & 0 & B \\ 0 & C & 0 \\ B & 0 & A \end{vmatrix}; \quad (\text{B.5})$$

$$e_{ij}(4) = \begin{vmatrix} A & 0 & -B \\ 0 & C & 0 \\ -B & 0 & A \end{vmatrix}, e_{ij}(5) = \begin{vmatrix} C & 0 & 0 \\ 0 & A & B \\ 0 & B & A \end{vmatrix}; \quad (\text{B.6})$$

$$e_{ij}(6) = \begin{vmatrix} C & 0 & 0 \\ 0 & A & -B \\ 0 & -B & A \end{vmatrix}. \quad (\text{B.7})$$

Equation (4) for the SFI interface between variants 1 and 2 will be

$$[e_{ij}(2) - e_{ij}(1)]x_i x_j = \begin{vmatrix} 0 & 2B & 0 \\ 2B & 0 & 0 \\ 0 & 0 & 0 \end{vmatrix} x_i x_j = xy = 0. \quad (\text{B.8})$$

Solutions are the symmetric $x = 0$, $(100)_c$, and $y = 0$, $(010)_c$, the twinning mirror planes expected from symmetry.

For variants 1 and 3 Eq. (4) is

$$[e_{ij}(3) - e_{ij}(1)]x_i x_j = \begin{vmatrix} 0 & B & -B \\ B & A - C & 0 \\ -B & 0 & C - A \end{vmatrix} x_i x_j = (y - z) [2Bx + (A - C)(y + z)]. \quad (\text{B.9})$$

One solution of the equation is the expected symmetric case, $y = z$, which corresponds to the $(01\bar{1})_c$ crystallographic plane. The second, non-symmetric case, is $2Bx + (A - C)(y + z) = 0$. This is the equation of a plane having a normal n where $n_x = 2B$, $n_y = (A - C)$, and $n_z = (A - C)$. This plane has $(hkk)_c$ Miller indexes, and therefore orthogonal to the $(01\bar{1})_c$. The ratio of h to k is $2B/(A - C)$, or $2(c - b)/(b + c - 2a)$ and depends only on the lattice parameters of the orthorhombic phases $[h/k = 2(2c_0 - b_0)/(b_0 + 2c_0 - 2\sqrt{2}a_0)]$. For the lattice parameters of the Ti-Al-Nb DO₁₉ and O phases [4], the Miller indexes are close to $\{\bar{1}55\}_c$ and $\{\bar{1}44\}_c$, respectively.

Similarly, the solutions for all 15 pairs of domains were found. The results are given in Table 4. There are 30 ($N = 6 \times 5$) SFIs, of which only 21 are different orientations: 3 of the $\{100\}_c$ type, 6 of the $\{110\}_c$ type and 12 of the $\{hkk\}_c$ type.

Figure A.3 shows the directions of the SFI traces superimposed on the $[011]_c$ stereographic projection, as they would be seen for crystals oriented for TEM at the $[011]_c$ zone axis. Such drawings are useful in analyzing the nature of interfaces observed in TEM specimens of the Ti-Al-Nb alloys, as shown by Bendersky and Boettinger. Figure A.3a presents traces of the symmetric $\{001\}_c$ - and $\{110\}_c$ -type interfaces. Figure A.3b presents traces of the non-symmetric $\{hkk\}_c$ -type interfaces. Two of the $\{hkk\}_c$ -type interfaces are oriented edge-on ($kh\bar{h}$ and $k\bar{h}h$), and two are inclined but with a rational trace direction $[01\bar{1}]$ ($kh\bar{h}$ and $\bar{k}hh$). Since the lattice parameter varies with temperature and composition, a range of possible orientations of the interfaces is given for the orthorhombic phase having lattice parameters ranging from those of the Ti₂AlNb O-phase (determined in [24] as $a_0 = 0.60893$ nm, $b_0 = 0.95694$ nm, $c_0 = 0.46666$ nm) to those of the hexagonal DO₁₉ phase (determined in [4] as $a_h = 0.578$ nm, $b_h = 1.001$ nm, $c_h = 0.466$ nm).

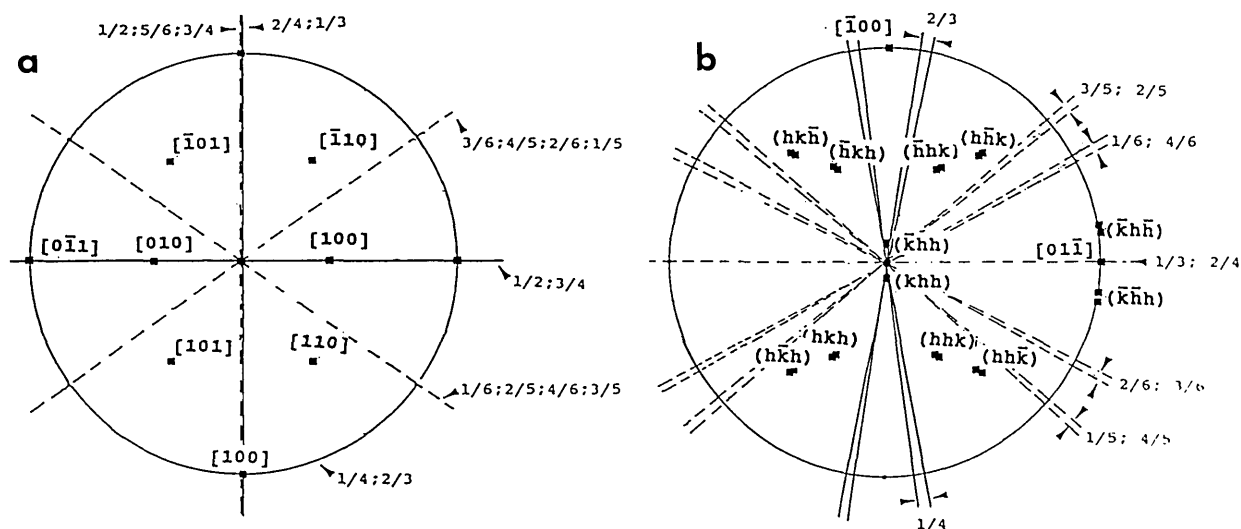


Fig. A.3. Directions of the SFI traces superimposed on the $[011]_c$ stereographic projections, as they would be seen for crystals oriented for TEM at the $[011]_c$ zone axes. (a) traces of the symmetric $\{001\}$ - and $\{110\}$ -type interfaces. (b) traces of the non-symmetric lattice parameter dependent $\{hkh\}$ -type interfaces. A range of possible orientations for the orthorhombic phase having lattice parameters ranging from those of the Ti_2AlNb O-phase (determined in [24] as $a = 0.60893$ nm, $b = 0.95694$ nm, $c = 0.46666$ nm) to those of the hexagonal DO_{19} phase (determined in [4] as $a = 0.578$ nm, $b = 1.001$ nm, $c = 0.646$ nm) is shown as shaded area.

8. References

- [1] S. M. L. Sastry and H. A. Lipsitt, *Met. Trans.* **8A**, 1543 (1977).
- [2] D. Banerjee, A. K. Gogia, T. K. Nandi, and U. A. Toshi, *Acta. Met.* **36**, 871 (1988).
- [3] R. Strychor, T. C. Williams, and W. A. Soffa, *Met. Trans.* **19A**, 1321 (1988).
- [4] H. T. Kestner-Weykamp, C. H. Ward, T. F. Broderick, and M. J. Kaufman, *Scr. Met.* **23**, 1697 (1989).
- [5] T. J. Jewett, J. C. Lin, N. R. Bonda, L. E. Seitzman, K. C. Hsieh, Y. A. Chang, and J. H. Perepezko, in *High-Temperature Ordered Intermetallic Alloys III*, C. T. Liu, A. I. Taub, N. S. Stoloff, and C. C. Koch, eds., Vol. 133, MRS (1989), p. 69.
- [6] R. G. Rowe, in *High Temperature Aluminides and Intermetallics*, S. H. Whang, C. T. Lui, D. P. Pope, and J. O. Stiegler, eds., TMS-AIME, Warrendale PA (1990), pp. 375-401.
- [7] K. Muraleedharan, A. K. Gogia, T. K. Nandi, D. Banerjee and S. Lele, *Met. Trans.* **23A**, 401 (1992).
- [8] K. Muraleedharan, T. K. Nandi, D. Banerjee, and S. Lele, *Met. Trans.* **23A**, 417 (1992).
- [9] D. A. Lukasak and D. A. Koss, *Met. Trans.* **21A**, 1990 (1990).
- [10] A. K. Gogia, D. Banerjee, and T. K. Nandy, *Met. Trans.* **21A**, 609 (1990).
- [11] D. Banerjee, A. K. Gogia, and T. K. Nandy, *Met. Trans.* **21A**, 627 (1990).
- [12] W. Cho, A. W. Thompson, and J. C. Williams, *Met. Trans.* **21A**, 641 (1990).
- [13] R. G. Rowe and M. F. X. Gigliotti, *Scr. Met.* **24**, 1209 (1990).
- [14] R. W. Hayes, *Scr. Met.* **23**, 1931 (1989).
- [15] H. T. Weykamp, D. R. Baker, D. M. Paxton, and M. J. Kaufman, *Scr. Met.* **24**, 445 (1990).
- [16] W. A. Baeslack III and T. Broderick, *Scr. Met.* **24**, 319 (1990).
- [17] J. A. Peters and C. Bassi, *Scr. Met.* **24**, 915 (1990).
- [18] R. S. Mishra and D. Banerjee, *Scr. Met.* **24**, 1477 (1990).
- [19] M. J. Cieslak, T. J. Headley, and W. A. Baeslack, *Met. Trans.* **21A**, 1273 (1990).
- [20] L. A. Bendersky and W. J. Boettinger, *Proc. Mater. Res. Soc. Symp.* **133** (1989).
- [21] D. Banerjee, T. K. Nandy, and A. K. Gogia, *Scr. Met.* **21**, 597 (1987).
- [22] D. Banerjee, T. K. Nandy, A. K. Gogia, and K. Muraleedharan, 6th World Conf. on Titanium, 1988, P. Lacombe, R. Tricot, and G. Beranger, eds., *J. Phys. (Les Ulis, Fr.)*, p. 1091.
- [23] D. G. Konitzer, I. P. Jones and H. L. Fraser, *Scr. Met.* **20**, 265 (1986).
- [24] B. Mozer, L. A. Bendersky, W. J. Boettinger, and R. G. Rowe, *Scr. Met.* **24**, 2363 (1990).
- [25] L. A. Bendersky, W. J. Boettinger, and A. Roytburd, *Acta Metall. Mater.* **39** 1959 (1991).
- [26] L. D. Landau and E. M. Lifschitz, *Statistical Physics*, Addison-Wesley (1958).
- [27] *International Tables of Crystallography*, Vol. A, T. Hahn, ed., Reidel Publishing Co., Dordrecht (1978).
- [28] Yu. A. Izyumov and V. N. Syromyatnikov, *Phase Transitions and Crystal Symmetry*, Kluwer Academic Publ. (1990).
- [29] A. Bagaryatski, T. V. Tagunova, and G. I. Nosova, *Dokl. Akad. Nauk SSSR* **122**, 539 (1958).
- [30] J. W. Cahn, *Acta Met.* **25**, 721 (1977).
- [31] R. Portier and D. Gratias, *J. Phys.* **43**, C4-17 (1982); M. Guymont, D. Gratias, R. Portier, and M. Fayard, *Phys. Stat. Sol.* **38**, 629 (1976).

- [32] L. A. Bendersky, W. J. Boettinger, B. Burton, F. S. Biancaniello, and C. B. Shoemaker, *Acta Metall. Mater.* **38**, 931 (1990).
- [33] A. L. Roitburd, *Sov. Phys.—Solid State* **10**, 2870 (1969).
- [34] J. W. Christian, *Theory of Phase Transformations in Metals and Alloys*, Pergamon (1975).
- [35] A. G. Khachaturian, *Theory of Structural Transformations in Solids*, J. Wiley and Sons, New York (1983).
- [36] J. Sapriel, *Phys. Rev. B*, **12**, 5128 (1975).
- [37] A. L. Roytburd, in *Solid State Physics*, Vol. 33, Academic Press (1978).
- [38] T. Saburi and C. M. Wayman, *Acta Met.* **27**, 979 (1979).
- [39] M. S. Wechsler, D. S. Lieberman and T. A. Read, *Trans. AIME* **197**, 1503 (1953).
- [40] C. M. Wayman, *Introduction to Crystallography of Martensitic Transformations*, MacMillan, New York (1964).
- [41] J. W. Cahn, *Acta Met.* **25**, 1021 (1977).

About the authors: L. A. Bendersky and W. J. Boettinger are metallurgists in the Metallurgy Division of the NIST Materials Science and Engineering Laboratory. A. Roytburd is a professor in the Department of Materials and Chemical Engineering of the University of Maryland. The National Institute of Standards and Technology is an agency of the Technology Administration, U.S. Department of Commerce.

Transformation of BCC and B2 High Temperature Phases to HCP and Orthorhombic Structures in the Ti-Al-Nb System. Part II: Experimental TEM Study of Microstructures

Volume 98

Number 5

September–October 1993

L. A. Bendersky and
W. J. Boettinger

National Institute of Standards
and Technology,
Gaithersburg, MD 20899-0001

Possible transformation paths that involve no long range diffusion and their corresponding microstructural details were predicted by Bendersky, Roytburd, and Boettinger [J. Res. Natl. Inst. Stand. Technol. 98, 561 (1993)] for Ti-Al-Nb alloys cooled from the high temperature BCC/B2 phase field into close-packed orthorhombic or hexagonal phase fields. These predictions were based on structural and symmetry relations between the known phases. In the present paper experimental TEM results show that two of the predicted transformation paths are indeed followed for different alloy compositions. For Ti-25Al-12.5Nb (at%), the path includes the formation of intermediate hexagonal phases, A3 and DO₁₉, and subsequent formation of a metastable domain structure of the low-temperature O phase. For alloys close to Ti-25Al-25Nb (at%), the path involves an intermediate B19 structure and sub-

sequent formation of a translational domain structure of the O phase. The path selection depends on whether B2 order forms in the high temperature cubic phase prior to transformation to the close-packed structure. The paper also analyzes the formation of a two-phase modulated microstructure during long term annealing at 700 °C. The structure forms by congruent ordering of the DO₁₉ phase to the O phase, and then reprecipitation of the DO₁₉ phase, possibly by a spinodal mechanism. The thermodynamics underlying the path selection and the two-phase formation are also discussed.

Key words: domain interfaces; phase transformations; thermodynamics; Ti-Al-Nb phases; transmission electron microscopy.

Accepted: May 14, 1993

1. Introduction

Bendersky, Roytburd, and Boettinger [1] have analyzed different phase transformation sequences and corresponding microstructures that may be possible in the course of transformations with no long-range diffusion (partitionless) of a BCC-based high temperature phase to close-packed phases for Ti-Al-Nb alloys. The analysis is based only on the crystallography of the equilibrium low and high temperature phases existing near the (Ti,Nb)₃Al binary join. Based on formal maximal group/subgroup relations, possible connections spanning the

high and low temperature phases (corresponding to high and low symmetry) have been found. These relations give different sequences involving symmetry-decreasing subgroups and one symmetry increasing-supergroup that might be considered to represent possible transformation paths. The transformation paths involve intermediate transitional structures, possibly metastable or unstable.

Assuming that the formal transformation steps actually occur as phase transitions, different transformation paths will result in different sequences

of domain formation, i.e., in different final microstructures. The final single phase microstructures can be distinguished by the type and hierarchy of domain interfaces. Analysis of the interfaces is essential for understanding the transformation path, and is the major subject of this paper.

Transformation paths, derived from group/subgroup relations, can only be applied to transitions where no long range diffusion occurs, i.e., when a single phase transforms to a single phase of the same composition. For equilibrium transformation in multi-component systems, this can only occur at special compositions (consolute points) or for second or higher order transitions [2]. However, partitionless transformations can also occur during cooling for first order transitions (for alloys with equilibrium multiphase fields) when sufficient undercooling of the high temperature phase is achieved that a limit of metastability is reached. This limit defines a temperature where the metastable undercooled phase becomes unstable and spontaneous transformation occurs with no long-range diffusion requirement (congruent ordering) [3–5]. Experimentally, such congruent ordering could occur during continuous cooling if the cooling rate is fast enough to prevent competing transformations involving long-range diffusion. Clearly a mechanism for fast transformation kinetics must be available for these partitionless transformations, i.e., fast short-range diffusion in chemical (substitutional or interstitial) ordering or mobile defect motion producing the necessary atomic displacements in displacive (martensitic) ordering.

In this paper, experimentally observed microstructures of three alloys from and near the pseudo-binary $(\text{Ti,Nb})_3\text{Al}$ section will be analyzed. The alloys are Ti-25Al-12.5Nb (at%) (Alloy 1), Ti-25Al-25Nb (at%) (Alloy 2) and Ti-28Al-22Nb (at%) (Alloy 3). The alloys are close in composition to some alloys studied by different research groups in attempts to develop titanium aluminides for aerospace high temperature structural applications (see Refs. [1–22] in [1]). We believe that the approach used here where the transitions are viewed as a sequence of symmetry changes will provide a unified view of the complex microstructural transitions in these materials. The microstructures studied, as represented by the distribution, type and morphology of interfaces induced by the transformations, will be compared with the interfaces predicted by the theoretical considerations of [1]. The predictions represent idealized transfor-

mations, without taking into account such complications as the temporary coexistence of parent and transformed phases, or the mobility of the interfaces created. Therefore the predictions will be considered primarily as a point of reference for comparison to the details of the actual transformation process. The main goal of the paper is to demonstrate that the microstructures of the alloys studied correspond very closely to two of the possible transformation paths predicted:

For Alloy 1—with intermediate hexagonal phases, $[\text{Im}\bar{3}\text{m}(\text{A}2) \rightarrow \text{Cmcm}(\text{A}20) \rightarrow \text{P}6_3/\text{mmc}(\text{A}3) \rightarrow \text{P}6_3/\text{mmc}(\text{D}0_{19}) \rightarrow \text{Cmcm}(\text{O})]$,

For Alloys 2 & 3—with possible intermediate orthorhombic B19 structure $[\text{Pm}\bar{3}\text{m}(\text{B}2) \rightarrow \text{Pm}(\text{B}19) \rightarrow \text{Cmcm}(\text{O})]$.

In addition to the study of the diffusionless transformations, the effect of prolonged annealing, which results in a compositional phase separation, has been also investigated for the Ti-25Al-12.5Nb alloy. In this case the mechanism of microstructure formation becomes clear when the thermodynamic principles of both ordering transformations and phase separation in systems where both order and composition parameters variables are used [3,5].

2. Experimental

2.1 Specimen Preparation

Three alloys with the compositions Ti-25Al-12.5Nb (at%) (Alloy 1), Ti-25Al-25Nb (at%) (Alloy 2) and Ti-28Al-22Nb (at%) (Alloy 3) were prepared by arc melting. A minimum of ten remelts was necessary to ensure mixing of the components. All samples received a homogenization treatment at 1400 °C for 3 h in a vacuum tight furnace under 2/3 atm of gettered Ar. During heat treatment samples rested on a Y_2O_3 -coated Al_2O_3 substrate supported on a moveable pedestal which could be lowered out of the hot zone of the furnace into a lower chamber. The cooling rate of the samples during such cooling was estimated to be about 400 °C/min. SEM microprobe of these samples using elemental standards gave the following compositions: (Alloy 1) Ti-24.7Al-12.6Nb (at%) (Alloy 2) Ti-23.2Al-25.8Nb (at%); and (Alloy 3) Ti-27.9Al-22.8Nb (at%). Typical oxygen, nitrogen and hydrogen levels for this procedure were less than 500, 350, 40 wppm, respectively.

For the study of the partitionless transformations, samples were examined after additional annealing at 1100 °C for 4 d and cooling to room temperature at two rates: at about 400 °C/min in the furnace described above or by water quenching. These latter samples were heat treated in another furnace in evacuated and He-backfilled quartz tubes after being wrapped in Ta foil. As the results will show, the 400 °C/min cooling rate was slow enough to permit complete transformation to the orthorhombic phase for Alloy 1. However only partial transformation occurs for Alloys 2 and 3. Therefore samples of these two alloys were given a subsequent annealing at 700 °C for 15 min in quartz tubes. To determine the phase equilibrium at 700 °C, the samples annealed at 1100 °C were additionally annealed at 700 °C for different lengths of time, up to 26 d in quartz tubes.

TEM foils were prepared by a standard twin-jet electropolishing procedure using a 300 ml methanol, 175 ml *n*-butanol and 30 ml HClO₄ electrolyte at 0 °C. Optical metallography was performed by mechanical polishing and subsequent etching with Kroll's reagent.

2.2 The Problem of Artifact Structures in Ti Alloy Thin Foil (TEM) Specimens

The formation of artifact structures in different Ti alloys during electropolishing of TEM specimen has been discussed in the literature [6–13]. Charging of thin foils by hydrogen in the course of electrochemical thinning was found to be possible. The concentration of hydrogen may be sufficient to cause formation of either different hydrides and/or hydrogen-stabilized martensites. Artifact structures such as fcc, fct, hcp and orthorhombically distorted α_2 have been reported. The amount of the accumulated hydrogen depends on a specimen's thickness prior to electropolishing, and on the type and temperature of the electrolyte. It was claimed [7] that the charged hydrogen may escape from a thin foil after electropolishing, unless the foil is protected by an oxide layer. If hydrogen escapes the specimen, the reversion of the hydride may result in the formation of $1/2\langle 111 \rangle$ dislocation loops in the BCC phase.

In order to be confident that microstructures observed by TEM in this study do not contain the described artifacts, several TEM specimens of the same material were prepared for comparison by two additional thinning techniques, presumably not affected by hydrogen contamination. The first technique was twin-jet electropolishing with non-acid

electrolyte containing a solution of CaCl₂ in methanol [14]. The second technique was mechanical grinding to a 30 μm thickness with a dimpler followed by ion-milling. Specimens prepared by these two techniques show microstructures similar to those of the specimens prepared by an acid-based electrolyte.

3. High-Temperature Phases: Microstructure After Water Quenching From 1100 °C

The identity of the high temperature phase was evident from the microstructural examination of specimens water quenched from 1100 °C. Optical examination revealed large equiaxed grains that appeared a single phase. According to selected area electron diffraction (SAD) at room temperature, the phase has B2 order for all three alloys.

For Alloy 1 the presence of a high density of anti-phase boundaries (APBs) (observed using a dark-field image with a superlattice 100 reflection) suggests that at 1100 °C the high temperature phase was disordered BCC. The cooling rate during quenching was fast enough to prevent formation of the low temperature phases but not the ordering and coarsening of the anti-phase domains (APDs). Typical of B2 ordering, the APBs have a two-domain interconnected morphology with isotropically curved interfaces. From these studies it is not clear whether the BCC to B2 transition in the Ti-Al-Nb system is first order (with a BCC + B2 two phase field) or second order.

For Alloys 2 and 3 no APBs due to the BCC \rightarrow B2 ordering were observed after quenching. This fact suggests that the B2 order for these compositions exists at 1100 °C (in fact up to 1400 °C [15]).

We have referred here to the quenched-in phase as being cubic B2. However this is strictly correct only if local displacements of atoms from positions of cubic symmetry are ignored. The effect of such displacements are readily observed as an overall "tweed" contrast in TEM images for all three alloys (This tweed is known in the literature for different alloy systems as pre-martensitic, or pre-transformation phenomena [16]). Due to these displacements, the SAD patterns from all three alloys contain diffuse scattering: distortion of the cubic reflections, streaking along $\langle 011 \rangle^*$ and $\langle 1\bar{1}2 \rangle^*$ directions, and loci of diffuse intensity close to $1/2\langle 011 \rangle^*$ and $1/2\langle 1\bar{1}2 \rangle^*$ positions in reciprocal space. As will be seen later, these are the positions where reflections from different crystallographic variants of the

O phase will occur. For Alloy 3 additional weak diffuse scattering near $1/2(111)^*$ positions is probably due to ω -type distortions [17,18]. In addition to the “tweed”, defects similar in contrast to dislocation loops are seen occasionally for all three alloys and are believed to be related to the nucleation mechanism of the low temperature phases.

4. Microstructures Due to the Diffusionless Transformation of the High Temperature Cubic Phase to the Orthorhombic O Phase

4.1 Microstructure of Alloys 2 and 3 Corresponding to the Transformation Path $Pm\bar{3}m(B2) \rightarrow Pmma(B19) \rightarrow Cmcm(O)$

From the transformation paths suggested by the symmetry considerations in [1], the $Im\bar{3}m(A2) \rightarrow Pm\bar{3}m(B2) \rightarrow Pmma(B19) \rightarrow Cmcm(O)$ path (2) is the only one expected when B2 ordering precedes the transition to the close-packed structure. Here we will demonstrate that the experimental evidence from TEM supports this formal supposition for both Alloys 2 and 3 which have the B2 structure as the high-temperature parent phase. The observed distribution and type of interfaces of the O phase correspond to those shown schematically in Fig. 9 of Ref. [1], with the exception that this schematic presumed the parent phase was BCC and thus includes the APBs due to the BCC \rightarrow B2 ordering. Microstructures similar to those observed here, but with B2 APBs, have been observed recently for a Ti-24Al-15Nb (at%) alloy where the parent phase was indeed disordered BCC (Ref. 8 from [1]).

4.1.1 Formation of the Plate-Like Domains of the O Phase For Alloys 2 and 3 the kinetics of transformation of the B2 phase to a low temperature phase was found to be relatively sluggish as is evident from optical micrographs, Fig. 1a, b. The micrographs show regions of partially transformed material, differing in their volume fraction according to the differences in cooling rates of the specimens. Annealing of the water quenched specimens (with 100% retained B2 phase) at 700 °C for 15 min was sufficient to produce complete transformation (Fig. 1c). Apparently the transformation proceeds by copious nucleation where the transformed regions grow uniformly outward until impingement. The transformation is partitionless without measurable difference in composition between the parent and transformed regions.

From TEM observations of the partially transformed specimens it is evident that the transformed regions have a complex microstructure of plate-like domains (Fig. 2). The smallest plates typically form an alternating sequence packed in a region named a polytwin in Ref. [1]. The polytwins themselves often have a plate-like shape and alternate with similar polytwin plates, as shown in Fig. 3a, b. Growth of the plate-like structure into the B2 phase matrix appears to have a common but ragged and diffuse transformation front (Fig. 2). Only occasionally were independently grown single-domain plates observed. Therefore in most cases the growth of a plate is not independent but is correlated with the formation and growth of neighboring plates having rotational variants able to accommodate transformation strains.

Selected area electron diffraction (SAD) (Figs. 3c and 4) combined with convergent beam (CB) electron diffraction and powder neutron diffraction [19] confirm the plates to be the O phase. No other phases were found in the samples that were continuously cooled or in those annealed at 700 °C. From the SAD patterns of Fig. 4 a lattice correspondence between the B2 and the O phase is evident as the common one for BCC and close-packed structures [20]:

$$[001]_o \parallel [011]_c \text{ and } [100]_o \parallel [100]_c$$

(c—cubic; o—orthorhombic).

The correspondence is the same as that used for the subgroup scheme of Ref. [1]. It gives six rotational variants of the orthorhombic phase (either B19 or O for path 2), each with its basal $(001)_o$ plane parallel to one of the six $\{110\}_c$ planes of the parent cubic structure. Small mutual rotations of the contacting variants are necessary to accommodate the transformation strains (self-strains) by creating stress-free interfaces (SFIs), as discussed in [1].

The microstructure of sufficiently large volume has an average cubic symmetry due to the presence of all six rotational variants of the O phase. The symmetry is clearly seen in the SAD patterns of Fig. 4a, b, c showing (a) 4 mm, (b) 3 mm and (c) 2 mm average Laue symmetries corresponding to the major zone axes of the cubic symmetry, $[100]_c$, $[111]_c$ and $[110]_c$. These average axes indicate the orientation of the parent (transformed) B2 phase lattice.

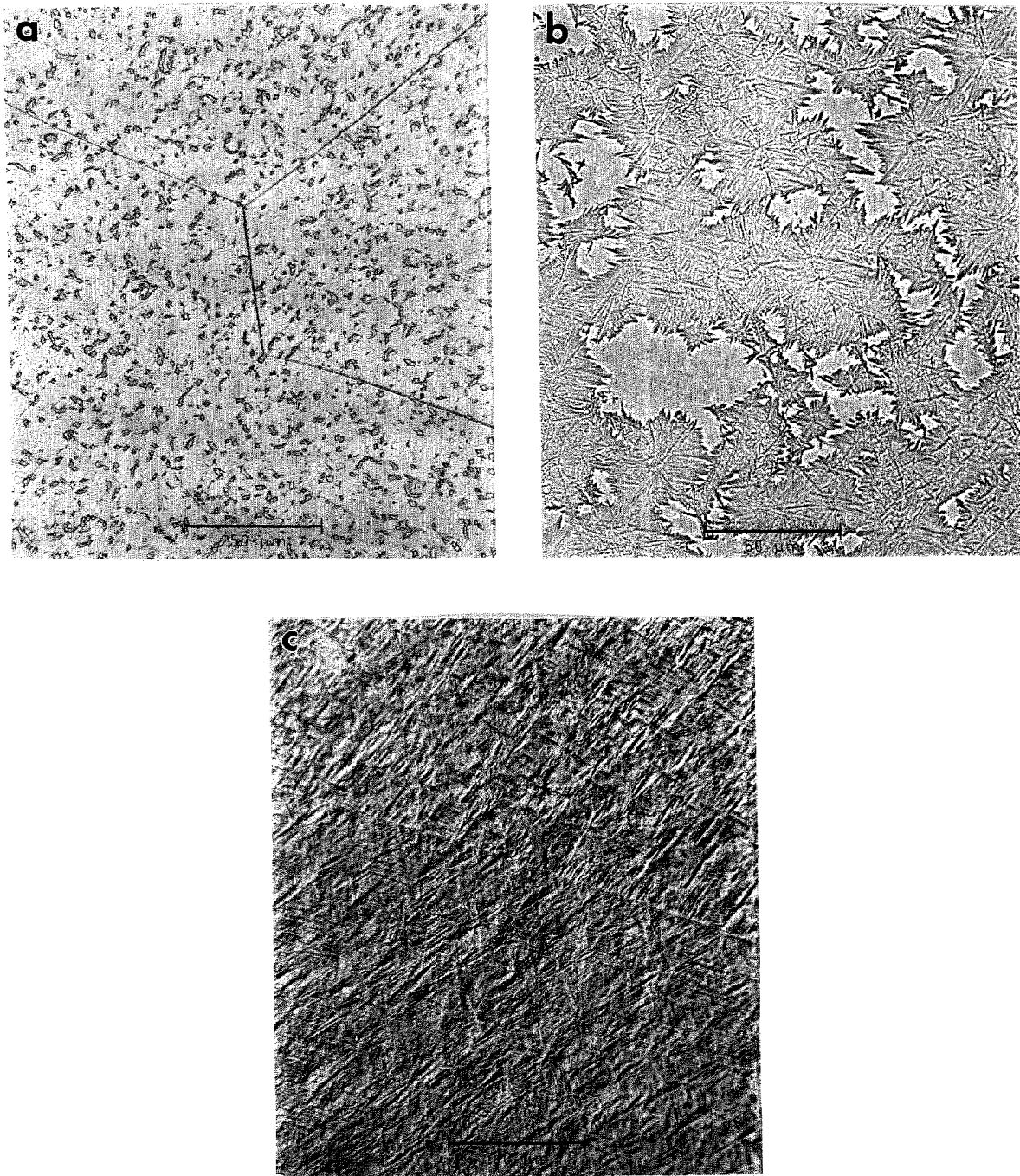


Fig. 1. Optical micrographs of Alloy 3 specimens cooled from 1100 °C at different cooling rates. Regions with different volume fractions transformed according to (a) a higher and (b) a slower cooling rate. (c) Annealing of the water quenched specimens (with retained B2) for 15 min at 700 °C was sufficient to produce complete transformation.

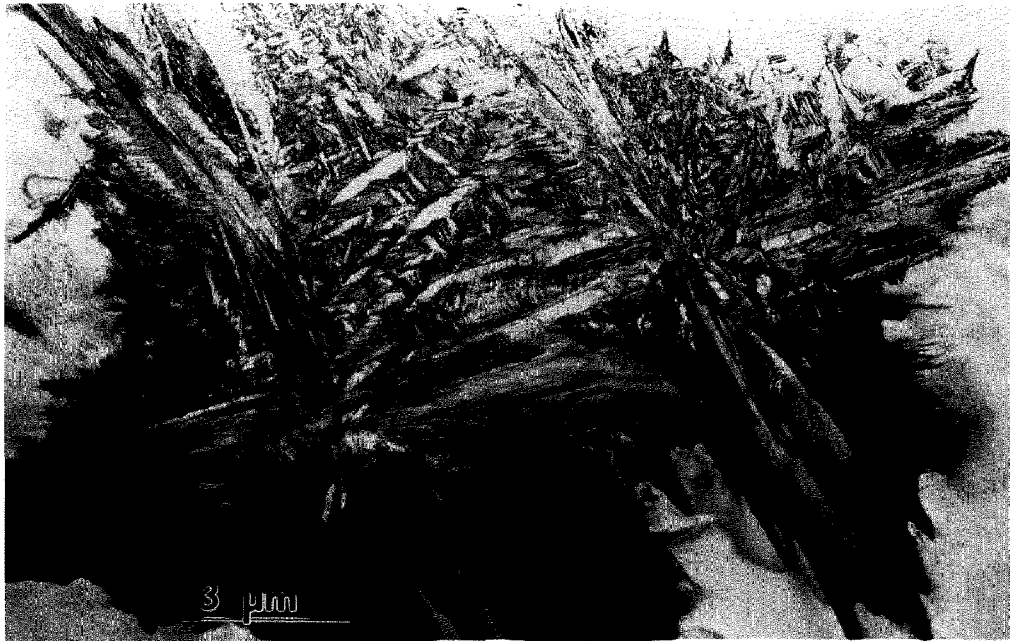


Fig. 2. The TEM microstructure of the Alloy 3 specimen corresponding to Fig. 1a. The TEM image shows islands of transformed material, surrounded by a B2 phase matrix. The islands consist of a complex plate-like structure of the O phase. The phases do not differ in composition.

4.1.2 Stress Accommodating Morphology of the O Phase All interfaces between the pairs of variants in and between the polytwin plates are expected to be SFIs, as discussed in [1]. The pair of polytwins shown in Fig. 3 will be analyzed in order to demonstrate that the interfaces are indeed described as SFI. The analysis will be performed in coordinates of the parent cubic lattice. Two polytwin plates are seen in Fig. 3a, with the planar A-A interface between them [for a $[011]_c$ orientation of the thin foil, (Fig. 3c)]. The A-A interface has $(01\bar{1})_c$ orientation and is “edge-on.” The individual plates in the polytwins have nearly parallel inclined interfaces (B-B and C-C sets) between the variants. The interface traces are approximately $\pm 45^\circ$ to the $[100]_c$ direction. The plates in each polytwin are nearly mirror related across the $(011)_c$ plane, and therefore there is an apparent continuity of the plates across the A-A polytwin interface.

Dark field imaging with the 020_o reflection (Fig. 3b) proves that the plates labeled 5 and 5' in Fig. 3a from each polytwin belong to the same variant 5 (the variant labeling follows the scheme described in [1]). The variant is oriented with $[001]_o$ parallel to $[011]_c$ (the beam direction) and the 020_o , 200_o and 110_o reflections of the variant do not overlap with reflections from the other variants. Misorientation between the 5 and 5' plates (around a common $[001]_o$) is measured as about 10° (Fig. 3c). According to microdiffraction, the remaining two

plate orientations are close to $\langle 212 \rangle_o$ and belong to any pair chosen from among the 1, 2, 3, or 4 (not 6) variants [1].

If the structure shown in Fig. 3 is coherent and strain accommodating, the observed interfaces are expected to correspond to the SFIs calculated in [1]. Referring to Fig. A.3 in Appendix B of [1] (reproduced here as Fig. 3d,e) where the traces of the SFIs for the $[011]_c$ zone axis are given, we conclude (according to the measured angle of the trace and the widths of the B-B and C-C interface projections) that the B-B interface corresponds to $h\bar{h}k$ (or $hk\bar{h}$) between variants 3/5 (or 2/5) and the C-C interface corresponds to $h\bar{h}k$ (or $hk\bar{h}$) between variants 1/5 (or 4/5) (Fig. 3d, e). The ambiguity of choice between the pair of variants in the polytwin plate can be resolved if one determines what side of the projected B-B and C-C interfaces intersect the upper and lower surfaces of the TEM foil. In order to have the line of intersection of the B-B and C-C planes lie within the A-A plane (as Fig. 3 suggests), the combination of variants must be either 4/5 and 2/5 or 1/5 and 3/5. These interfaces are irrational (twins of the II kind) and therefore their exact orientation depends on the lattice parameter of the orthorhombic phase at the temperature of transformation (Fig. 3e shows the spread of possible orientations for lattice parameters varying between Ti_2AlNb and DO_{19} phases, see Ref. [1]).

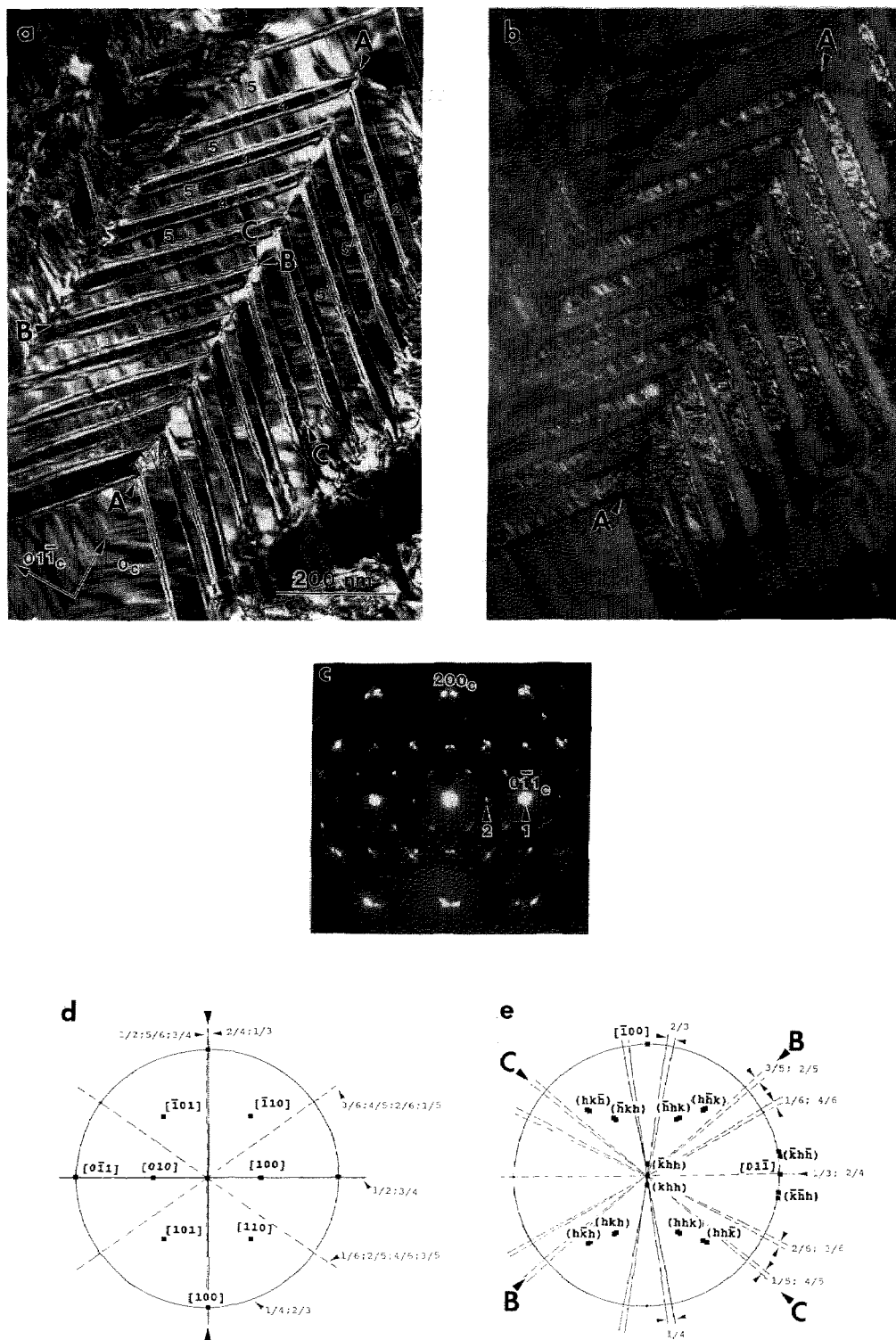


Fig. 3. Higher magnification view of the plate-like structure of Fig. 2 showing the plates to be arranged into a larger size secondary plate (polytwin) which alternates with another variant of polytwin plate. (a) and (b) are dark-field images with the g_1 and g_2 reflections, indicated in the (c) $[011]_k$ SAD pattern. The g_2 reflection, 020_o , images a single variant (S) of the O phase. (d,e) show $[011]_k$ stereographic projections with superimposed calculated $[1]$ traces of the (d) symmetric and (e) non-symmetric SFIs and the corresponding traces of the observed A-A, B-B and C-C interfaces of (a). The solid and dashed traces correspond to edge-on and inclined interfaces respectively.

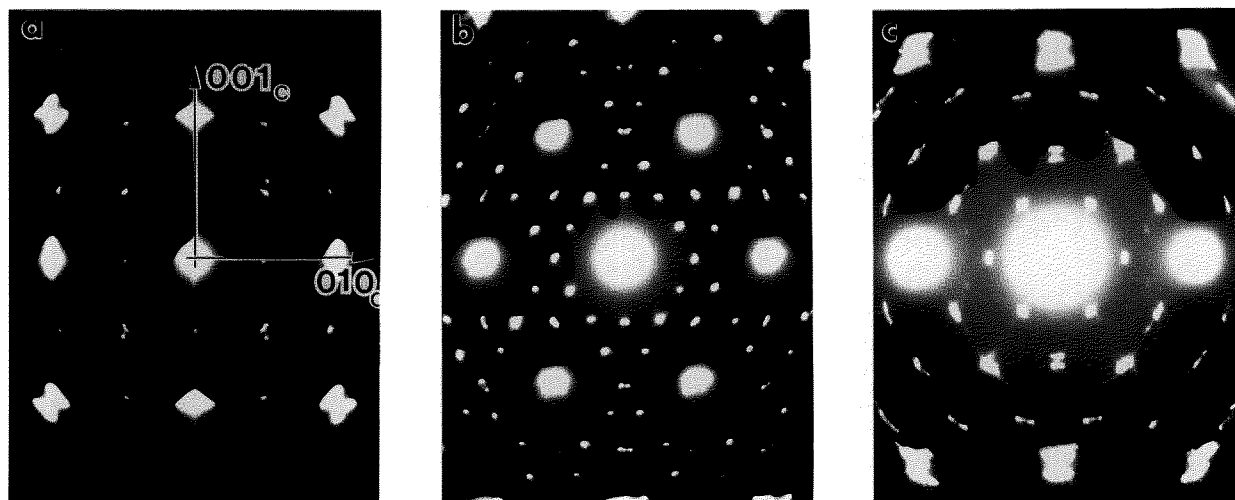


Fig. 4. A series of SAD patterns taken from an Alloy 2 specimen which was water quenched from 1100 °C and then annealed at 700 °C for 15 min. The selected area aperture was large enough to include numerous variants contributing to scattering. The patterns show average Laue symmetries (a) 4 mm, (b) 3 mm and (c) 2 mm corresponding to the major zone axes of the cubic symmetry, [100], [111] and [110], respectively. The strongest reflections (consisting of several reflections from different variants of the O-phase) correspond to the fundamental BCC reflections and determine the orientation relationship between lattices of the transformed B2 phase and the O phase variants.

The A-A interface consists of alternating segments that are structurally different. One type of segment is a $(01\bar{1})_c$ interface between 4 (or 1) and 2 (or 3) variants. This is a symmetric SFI (twin of the I kind). The second type of segment separating variant 5 ($5'$) misoriented plates is a low angle symmetric boundary ($\sim 10^\circ$) which may be relaxed by forming a dislocation wall.

All high angle interfaces in the polytwin microstructure in Fig. 3 are thus shown to be SFIs. Observation of such an elastic energy accommodated arrangement of plates suggests an interacting process during their formation, i.e., a process where the presence of certain combination of variants in one polytwin plate influences the formation of variants in a neighboring plate. Formation of a strain accommodating arrangement of twins, of both the I and II kind, is an important phenomena in martensitic transformations of numerous shape-memory alloys [21–23].

4.1.3 Substructure of the O Phase Primary Plates Closer examination of Fig. 3a, b reveals a substructure of a relatively high density of interfaces (defects) inside the plates of different variants of the O phase. The interfaces are of a translational type since they do not affect the positions of the reflections in each single variant. Dark field imaging was used to determine the R value using standard $R \cdot g = n$ ($n = 0, \pm 1, \pm 2, \dots$) invisibility criteria (R is the translation vector between two domains separated by the interface, g is an operating

dark field reflection). Figure 5a, b, c shows three dark field images taken from a single variant oriented close to the $[110]_o$ zone axis (SAD pattern in Fig. 5d). Two types of interfaces, different in their displacement vector R and morphology, are seen in these images. The presence of these interfaces are in accord with the transformation path 1 in [1].

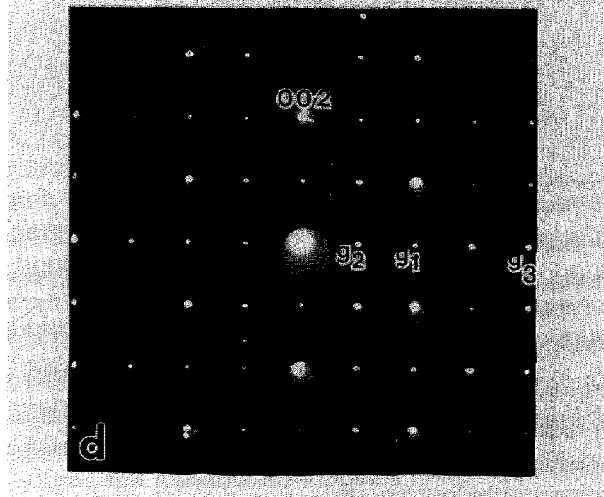
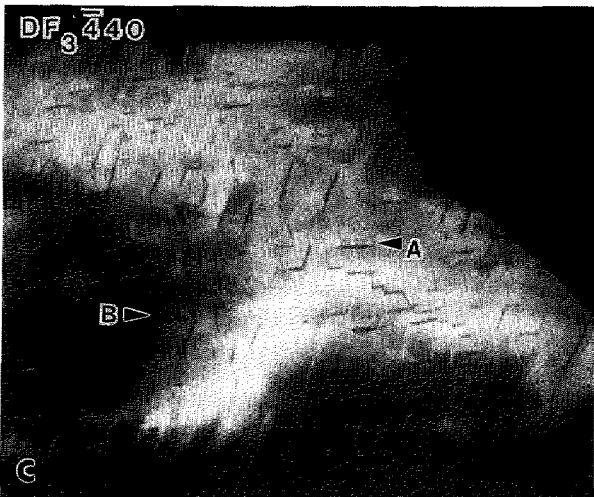
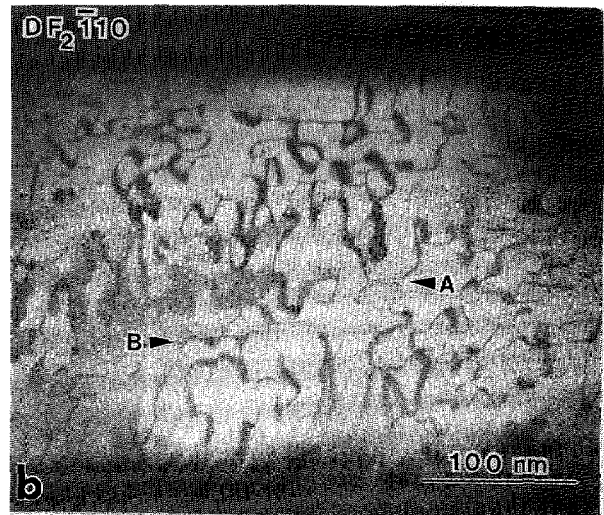
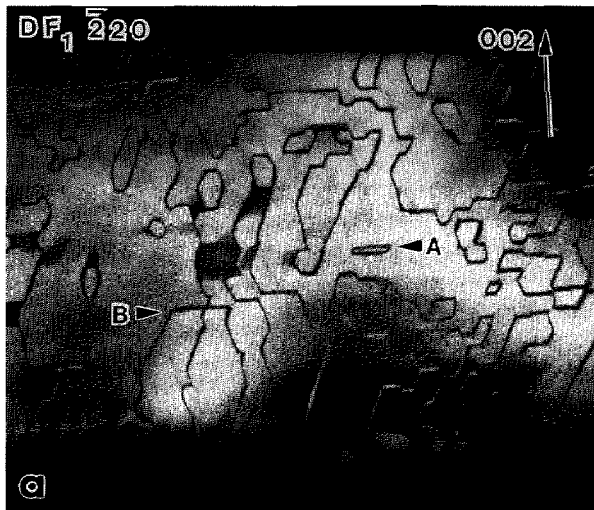
The interfaces of the first type, with a wavy APB appearance, are visible with the superlattice reflections of the O phase, e.g., $\bar{1}10_o$ in Fig. 5b, but are invisible with the fundamentals, e.g., 220_o and 440_o in Fig. 5a,c. The second type has a distinct faceted appearance (clearly seen in Fig. 5a) and is visible with both the superlattice and some fundamental reflections, e.g., 110_o and 220_o (Fig. 5a,b). Both types are invisible with 002_o . For the 440_o reflection the faceted interfaces has only residual contrast (Fig. 5c). The experimental results on the visibility for both interfaces are summarized and analyzed for various displacement vectors in Table 1.

Analysis of the $R \cdot g$ product for the first type suggests that the displacement vector R is $1/2[010]_o$. (C-centering of the $Cmcm$ space group of the O phase makes the $1/2[100]_o$ vector an equivalent one.) This displacement vector is close to the antiphase vector between two differently ordered $4c_1$ and $4c_2$ sites in the pseudo-hexagonal $(001)_o$ plane of the O phase. Such APBs may result after ordering of the B19 orthorhombic structure to the O phase structure (leading to a doubling of the a, b

Table 1. Experimental dark field visibilities and phase factors (Rg) for two types of interfaces forming substructure in the O phase in Alloys 2 and 3 (both g and R are in the O phase coordinates)

g (used in dark field)	002	$\bar{1}10$	$\bar{2}20$	$\bar{1}11$	$\bar{4}40$	400
Type I (curved interfaces)	i	v	i	v	i	i
Rg ($R = 1/2[0\ 1\ 0]$ or $R = 1/2[1\ 0\ 0]$)	0	1/2	1	1/2	2	0
	0	-1/2	1	-1/2	0	2
Type II (faceted interfaces)	i	v	v	v	r	i
Rg ($R = 1/4[0\ 1\ 2]$ or $R = 1/4[0\ 1\ 0]$)	1	1/4	1/2	1/4	1	0
	0	1/4	1/2	1/4	1	0

i – invisible; v – visible; r – residual.

**Fig. 5.** Three dark field (a–c) images taken from a single variant plate in specimen of Alloy 3 continuously cooled from 1100 °C. The dark field images are taken with the plate orientation close to the (d) $[110]_O$ zone axis using (a) $\bar{2}20_O$, (b) $\bar{1}10_O$ and (d) $\bar{4}40_O$ reflections in approximately a two-beam condition. Two type of interfaces with different displacement vectors and morphology are observed. Both types are seen in (b) and only the faceted type in (a). In (c) only residual contrast from the faceted interfaces is seen. Arrow markers A and B identify the same places in all three micrographs.

unit cell parameters) and are expected in the last step of the transformation path 2. The ordering requires a separation of the mixed (Al,Nb) site of the B19 (and B2) structure into predominantly Al ($4c_1$) and Nb ($4c_2$) sites in the O phase (see Fig. 3 of [1]). Such ordering will produce a two domain interconnected morphology with no triple junctions as schematically shown in Fig. 9 of [1]. The morphology is similar to that seen in Fig. 5b, where the curved APB interfaces appear as either closed loops (with enclosed volume) or are attached to other interfaces. The presence of the $1/2[010]_O$ APBs provides the only evidence for the existence of the possible transient B19 structure.

The invisibility of the second type of interfaces with the 002 reflection suggests that their displacement vector, R_2 , has a z-component that is either 0 or 1/2. Other visibility conditions (Table 1) correspond to the $[0\ 1/4\ 1/2]_O$ (or $[0\ 1/4\ 0]_O$) displacement vector of a two-domain structure. Indeed, as Fig. 5a shows, no triple junctions of the faceted interfaces are seen, and the interfaces form either interconnected or closed volumes. The $[0\ 1/4\ 1/2]_O$ vector in the smaller unit cell of the orthorhombic Cmc m (A20) or Pmma(B19) structures (with a and b parameters half of the O phase) corresponds to a unique vector $[1/2\ 0\ 1/2]_{B19}$. As it has been discussed in [1], such displacement between domains

is expected for the B2 to B19 transition, and therefore the faceted interfaces are due to the first step of the transformation path 2.

The B2 to B19 (or similarly BCC to A20) transition is of a displacive type, with both homogeneous and heterogeneous (shuffle) transformation strain components [1]. The homogeneous strain determines the orientation of the six twin variants of the orthorhombic or hexagonal structure, as was discussed in Sec. 4.1.1. The translational $[1/2\ 0\ 1/2]_{B19}$ domains result from shuffles acting in opposite directions ([24], Ref. [8] in [1]). An interface between such translational domains is expected to have structural relaxation toward the close-packed stacking faults. This is supported by the observation of residual contrast for the 440_O reflection (Fig. 5c) suggesting small displacements in addition to $[0\ 1/4\ 1/2]_O$. The faceted interfaces were analyzed by trace analysis in order to find their orientations. Two different crystallographic planes for the facets were found: the basal $(001)_O$ and close to the $\{221\}_O$.¹

When the twin plates are thin, the faceted interfaces appear as a sequence of stacking fault planes rather than domain boundaries. Dark field imaging of the interfaces (Fig. 6a) shows that they are $(001)_O$ planes. The APBs are seen as stretched between the twin boundaries (Fig. 6b), probably

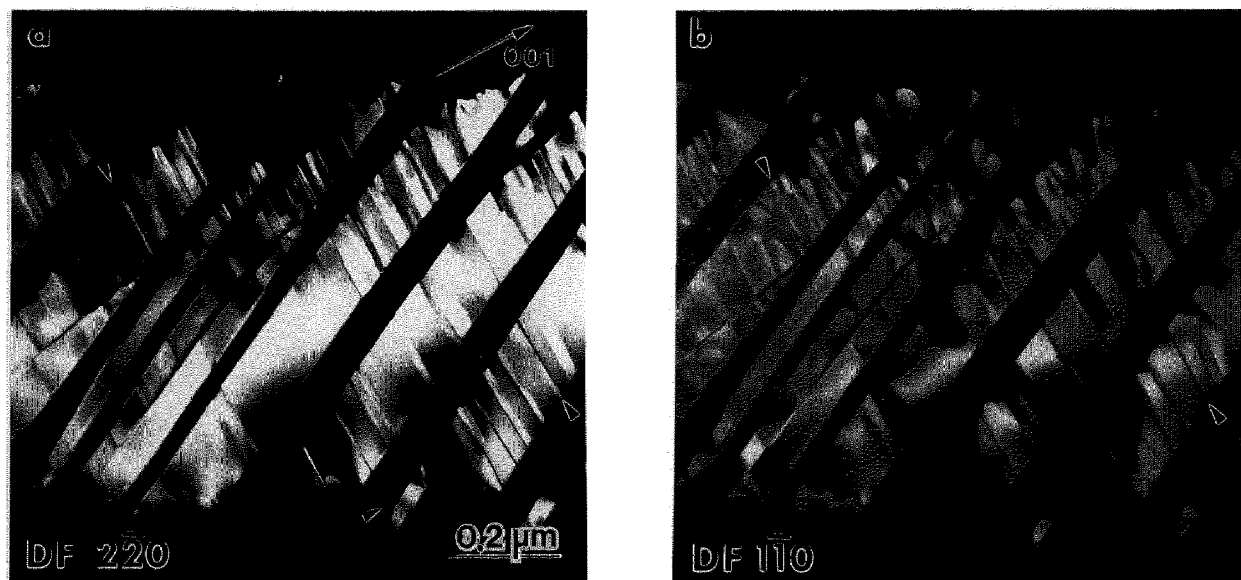


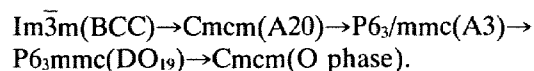
Fig. 6. Dark field images of (a) stacking fault (SF) type and (b) both SF and APB interfaces in thin plates of an O phase variant oriented with $[110]_O$ parallel to the electron beam. In (a) and (b) $2\bar{2}0_O$ and $1\bar{1}0_O$ reflections were used respectively.

¹ Similar crystallographic planes have been observed in the 2H martensite of Cu-Al alloys. Because the unit cell of the martensite is different from that described here, the indices of the observed planes are different [24].

because of surface energy considerations (balance of interfacial energies of APB and twin-type interfaces at a triple-junction).

4.2 Microstructure of Alloy 1 Corresponding to the Transformation Path $\text{Im}\bar{3}\text{m}(\text{BCC}) \rightarrow \text{Cmcm}(\text{A20}) \rightarrow \text{P6}_3/\text{mmc}(\text{A3}) \rightarrow \text{P6}_3\text{mmc}(\text{DO}_{19}) \rightarrow \text{Cmcm}(\text{O Phase})$

Alloys with compositions close to Alloy 1 exist at high temperature as a disordered BCC phase [15,25]. According to the theoretical considerations of [1], if the BCC does not order to B2 prior to the displacive transition to a close-packed structure, two transformation paths, 1 and 3, are possible. Here we will show evidence supporting the transformation path 1 for Alloy 1:



The main feature of the path is the formation of intermediate hexagonal symmetry phases. This causes the O-phase rotational variants to be related to each other not only by the cubic symmetry of the parent phase but also by hexagonal symmetry.

4.2.1 Transformation to the Coarse Needle-Like Structure During Continuous Cooling For Alloy 1 the transformation kinetics are significantly faster than are those for Alloys 2 and 3, and therefore cooling from 1100 °C to room temperature at a rate of 400 °C/min was slow enough to complete the transformation of the high temperature phase to the close-packed structure. The transformed microstructure has a morphology resembling a martensite structure when observed by optical metallography (Fig. 7). The TEM micrograph in Fig. 8 shows in more detail that the morphology is rather needle-like. The needles have very irregular interfaces (not resolved in Fig. 7), and no crystallographic habit plane. This is in great contrast to the mostly regular plate-like structure seen in Alloys 2 and 3. The blocky grains surrounding an elongated needle in Fig. 8 are probably cross-sections of needles oriented with their long axes parallel to the electron beam direction. The wavy character of the interfaces seems to be the result of impingement of needles during their independent growth. In a few regions, grains were found to be separated from each other by a thin layer identified as the BCC phase (Fig. 9). Enrichment of Nb in the BCC layer was detected by EDS for this and similar alloys [25]. The observed morphology suggests that near

impingement, some diffusion does occur during the growth of the needles. We presume that in these regions the competing transformation with long range diffusion is marginally possible. Thus the cooling rate of these samples is on the lower limit for the dominance of the partitionless transformation.

Selected area diffraction from individual needles correspond to the reciprocal lattice of the DO_{19} ordered hexagonal structure. The orientation relationship between different variants of the hexagonal structure and the previously existing BCC phase can be inferred from Fig. 10, which is taken from three neighboring grains forming a triple junction. The present pattern is indexed as three variants of the DO_{19} phase (h) with $[10\bar{1}0]_h \parallel [111]_c$ and $(0001)_h \parallel (110)_c$. This is the known Burgers orientation relationship [21].

Close examination of the SAD patterns reveals splitting of the spots and diffuse streaking in and normal to the $(0001)_h$ plane. These diffraction effects come from the substructure inside the needles, which is seen as dark contrast in Fig. 8. The nature of the spot splitting indicates the existence of orthorhombic distortions in the basal

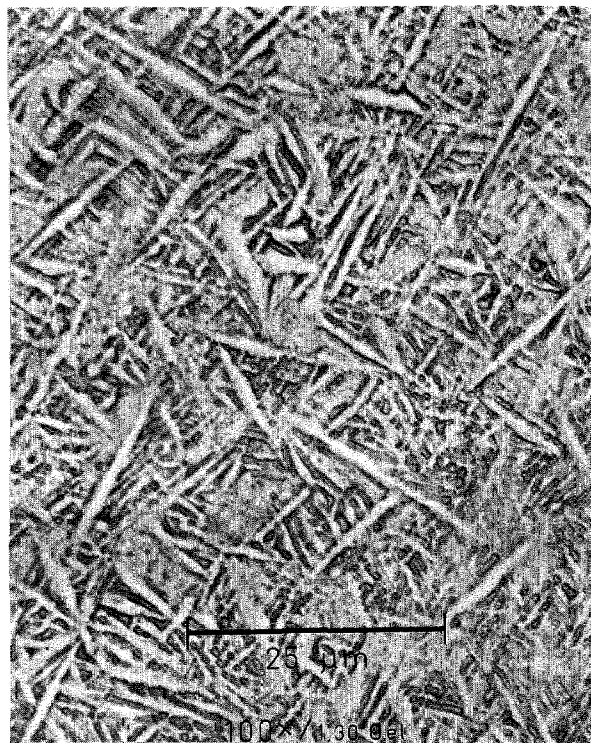


Fig. 7. Optical micrograph showing a needle-like transformed microstructure of Alloy 1 continuously cooled from 1100 °C at 400 °C/min.



Fig. 8. Bright field TEM micrograph showing the detailed morphology of the needles shown in Fig. 8. The needles have very irregular interfaces. Blocky grains between elongated needles are most probably cross-sections of the needles with their long axes normal to the TEM foil.

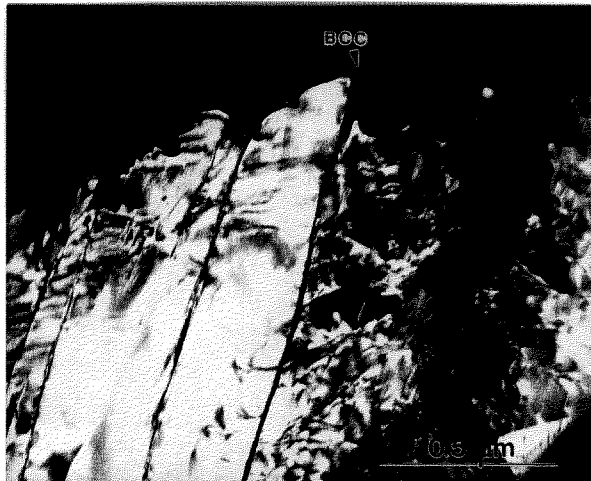


Fig. 9. Thin (dark) layers of the BCC phase separating transformed phase grains. The dark-field image is taken with a DO_{19} reflection which is well separated from the BCC's. Dark contrast in the upper-left part of the photograph belongs to a different grain.

plane of the DO_{19} phase and suggests the presence of O phase domains. Therefore the hexagonal indexing that we use describes only the average symmetry and orientation of the needles.

The needle-like structure is not a stress accommodating plate-like structure as observed in Alloys 2 and 3. This difference may perhaps be understood by considering the possibility that the transformation of the BCC phase of Alloy 1 may occur at higher temperature than Alloys 2 and 3 as indicated by the occurrence of some small level of

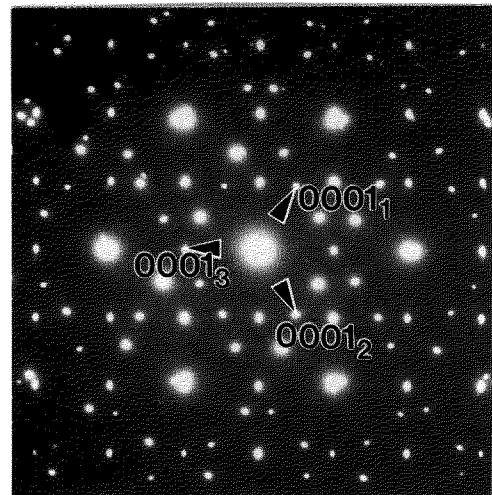


Fig. 10. SAD pattern taken from three grains forming a triple junction in the Alloy 1 cooled from 1100 °C. The pattern has $[10\bar{1}0]_b \parallel [111]_c$ (three 60° rotated $\langle 10\bar{1}0 \rangle_b$ patterns around $[111]_c$) and $(0001)_h \parallel \{110\}_c$ in support of the Burgers OR found for the Alloys 2 and 3.

long-range diffusion near impingement. At higher temperatures the ductility of the phases may be sufficient to accommodate the transformation stresses by plastic deformation (including formation of the observed stacking faults) and negate the requirement to form a stress accommodating structure. Indeed a dependence of morphology on cooling rate has been observed for alloys similar in composition to Alloy 1 [25] that range from those accommodating stress at high cooling rates to those

similar to the morphologies described here at lower cooling rates. The occurrence of similar orientation relationships in both diffusionless and diffusion controlled (precipitation) transformations is well known and is in fact observed in some other Ti-Al-Nb alloys [15].

4.2.2 Substructure of the Needles Similar to the result found for Alloys 2 and 3, the substructure of the needles has two types of interfaces associated with the translational domains. The interfaces have been imaged in dark field with different reflections belonging to three zone axes, $[11\bar{2}0]_h$, $[01\bar{1}0]_h$ and $[\bar{1}210]_h$, by tilting a single grain around the $[0001]_h$ direction, starting from the $[11\bar{2}0]_h$ zone axis (Fig. 11). As with Alloys 2 and 3, two types of interfaces are morphologically distinct: one has curved isotropic APB-type interfaces (Fig. 11h) and the other has planar interfaces. However the planar interfaces only occur in $(0001)_h$ planes for Alloy 1 (Fig. 11f) as compared to the closed (or interconnected) surfaces observed for the Alloys 2 and 3. The observed visibility conditions for both types of interface are similar to those reported in [8] (see Ref. [1]).

The wavy isotropic interfaces are APBs between the domains formed by ordering of the disordered hexagonal structure to the DO_{19} structure [26]. The APBs have $R = (1/6)\langle 11\bar{2}0 \rangle_h$ displacement vectors. For the three such R vectors equivalent under the 6-fold symmetry operation, there are three different APBs and four distinct translational domains. (Compare this to the single APB and two domains observed in Alloys 2 and 3). When the APBs are imaged with superlattice reflections, only two of the three APBs are visible according to the R_g conditions. Therefore no triple junctions of the APBs can be seen. Comparison of the two dark field micrographs shown in Figs. 11e and 11h, show that some APB segments are visible for both of these imaging conditions (for $R = 1/6[\bar{1}210]_h$), while some segments are visible for only one of the imaging conditions. Therefore, the presence of the disordered hexagonal A3 as an intermediate state is established by the presence of the $1/6\langle 11\bar{2}0 \rangle_h$ APBs, which can only be due to the $P6_3/mmc(A3) \rightarrow P6_3/mmc(DO_{19})$ transition.

The second type of interface, with a planar morphology, was identified as having $1/6\langle 20\bar{2}3 \rangle$ displacement vector. These interfaces give rise to the $[0001]^*$ streaking. Because the interfaces terminate inside the needles, they are rather stacking fault defects than boundaries of translational domains (like in the Alloys 2 and 3). The stacking faults may

provide an inhomogeneous shear necessary to satisfy conditions of the invariant plane strain [21,22].

4.2.3 Congruent Ordering of the DO_{19} to O Phase The presence of domains of the O phase (as a part of the primary needle substructure) is manifest in the splitting of the DO_{19} reflections and in the complex contrast showing $[0001]_h$ directionality as seen in Fig. 11f, i, l. The domains with plate-like morphology can only clearly be seen in the $[0001]_h$ zone axis orientation where the domain interfaces are “edge-on”, as shown in Fig. 12a. (In order to obtain maximum contrast, the TEM foil must be slightly off of the exact $[0001]_h$ zone axis in order to have a different excitation error and accordingly contrast for different domains.) In Fig. 12 two directions of interface trace, $\langle 1\bar{1}00 \rangle_h$ (A-A) and $\langle 11\bar{2}0 \rangle_h$ (B-B), are observed corresponding to $(11\bar{2}0)_h$ and $(\bar{1}100)_h$ interfacial “edge-on” planes. The SAD patterns (Fig. 12b, c) were taken from areas with only one type of interface, A or B in Fig. 12a, respectively. The corresponding SAD patterns are given in Figs. 12b, c. The patterns show splitting and streaking of reflections in directions normal to the interfaces. The SAD patterns from Fig. 12 can be reasonably well explained as belonging to two variants of the O phase, with coinciding (a) $(130)_{O(1)} \parallel (1\bar{3}0)_{O(2)}$ planes (A-A interfaces) and (b) $(110)_{O(1)} \parallel (1\bar{1}0)_{O(2)}$ planes (B-B interfaces) as seen in Fig. 13. SAD from a region of bright uniform contrast (upper left side of Fig. 12) shows the hexagonal symmetry of the pattern without the splitting of the peaks. This suggests that this region is untransformed DO_{19} phase.

In a single grain (needle) most often only one orthogonal set of such interfaces (plates) was observed, e.g., $(\bar{1}100)_h$ and $(11\bar{2}0)_h$ in Fig. 12. Neighboring grains in the same $[0001]_h$ orientation have similar orthogonal sets of plates but rotated 60° or 120° . Occasionally the rotated sets are observed in different locations of the same grain, as is seen in Fig. 14. These sets of interfaces, related to each other by the hexagonal symmetry of the parent phase, belong to other pairs of variants of the orthorhombic phase. The presence of the O phase domains related to each other by the hexagonal symmetry clearly indicates the occurrence of the last step in the transformation path 1; viz., the DO_{19} to O phase transition. As was discussed in [1], the $\{1\bar{1}00\}_h$ and $\{11\bar{2}0\}_h$ interfaces are SFIs accommodating transformation strains in the hexagonal to orthorhombic symmetry transitions. In this transition the SFIs are always symmetric.

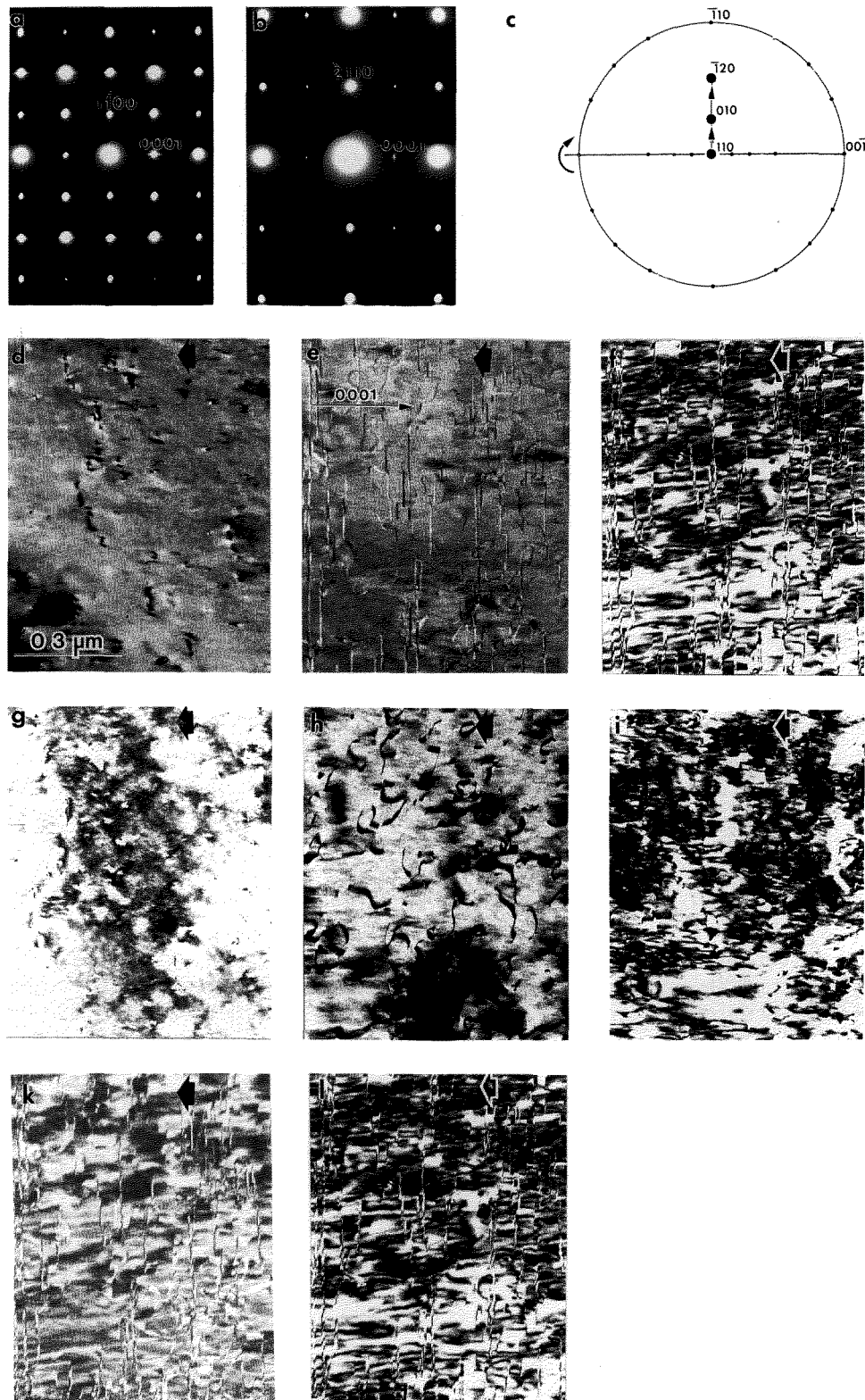


Fig. 11. Series of dark field images taken from a single grain of the transformed Alloy 1 in the $[1\bar{1}20]_h$, $[01\bar{1}0]_h$ and $[\bar{1}210]_h$ zone axis orientations (SAD patterns of $[1\bar{1}20]_h$ and $[01\bar{1}0]_h$ patterns are shown in (a) and (b)). The sequence of orientations was obtained by tilting the grain around the $[0001]_h$ direction as shown in the stereographic projection (c). The dark field images are taken close to a two-beam condition using the following reflections: (d) 0002 , (e) $1\bar{1}00$ and (f) $2\bar{2}00$ from the $[1\bar{1}20]_h$ ZA; (g) 0002 , (h) $2\bar{1}\bar{1}0$ and (i) $4\bar{2}20$ from the $[01\bar{1}0]_h$ ZA; (k) $10\bar{1}0$ and (l) $20\bar{2}0$ from the $[\bar{1}210]_h$ ZA.

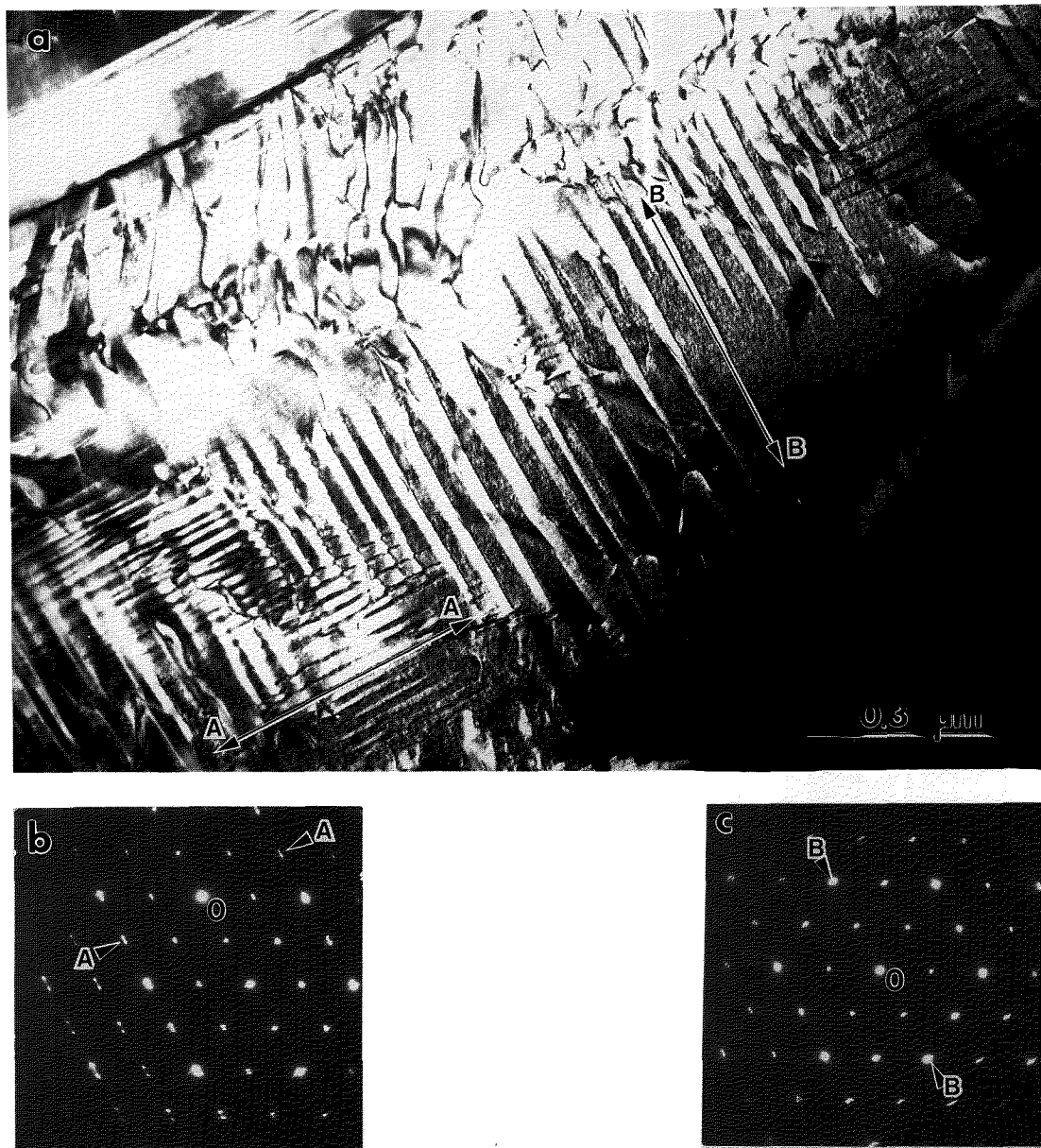


Fig. 12. (a) TEM dark field image of a continuously cooled Alloy 1 specimen, slightly off the $[0001]_h$ zone axis in order to give different excitation errors for different domains. Two orthogonal directions of the interface traces, $[\bar{1}\bar{1}00]_h$ (A-A) and $[\bar{1}\bar{1}\bar{2}0]_h$ (B-B), correspond to $(1\bar{1}\bar{2}0)_h$ and $(\bar{1}\bar{1}00)_h$ interfacial planes between two variants of the O phase with coinciding $130_{O(1)}/\bar{1}30_{O(2)}$ and $(110)_O/(\bar{1}\bar{1}0)_O$ planes. (b,c) SAD patterns taken from areas where only one type of interface is present (area A and B on Fig. 15a).

5. Decomposition of the Metastable O Phase in Alloy 1 After Prolonged Annealing at 700 °C

Long term annealing of specimens of Alloy 1 at 700 °C for 26 d produces a third level of microstructure finer than that produced during the initial cooling from 1100 °C. The coarser two levels of microstructure (shown in Figs. 8 and 12) are re-

tained during this heat treatment.² The third level is contained within the second level shown in Fig. 12. A typical example of the second and third level microstructure is shown in Fig. 15. The structure within each first level needle remains coherent and

² The microstructure produced during cooling is more resistant to coarsening and recrystallization as compared to Alloys 2 and 3 under the same annealing conditions [15].

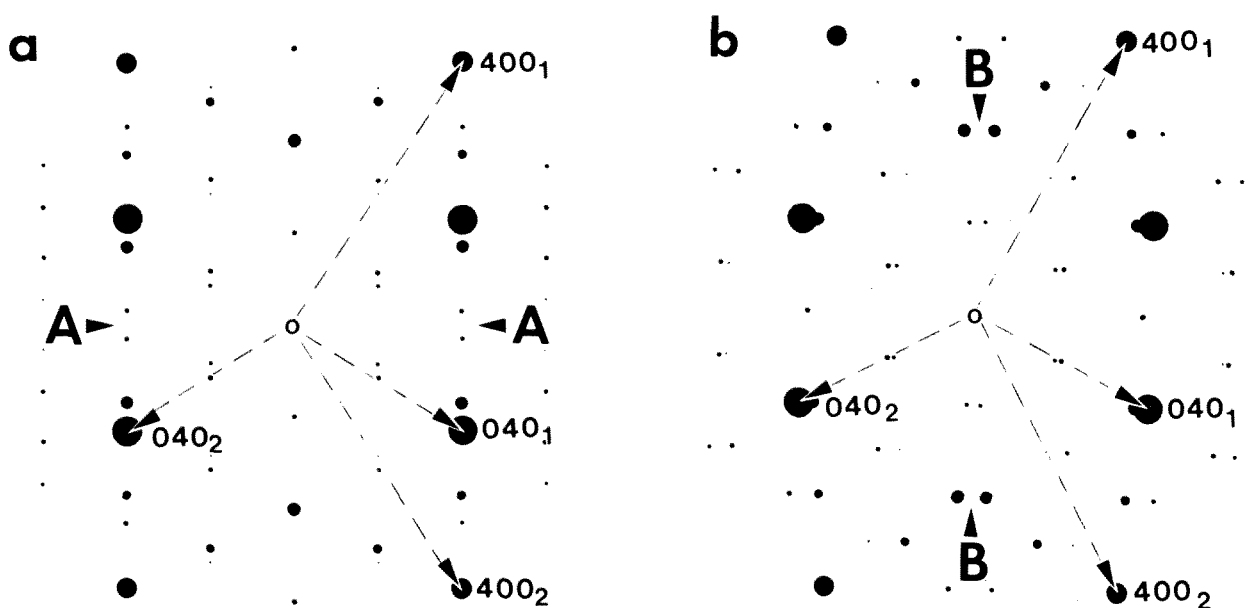


Fig. 13. The superimposed $[001]_O$ diffraction patterns of two variants of the O phase rotated 120° to each other, with a coinciding row of (a) $130_{O(1)}$ and $\bar{1}30_{O(2)}$ (plane A) and (b) $110_{O(1)}$ and $\bar{1}\bar{1}0_{O(2)}$ (plane B) reflections, corresponding to the experimental SAD of Fig. 15b, c, respectively. The kinematical intensities (size of the reflections) are calculated according to the O phase structure parameters in Ref. [19].

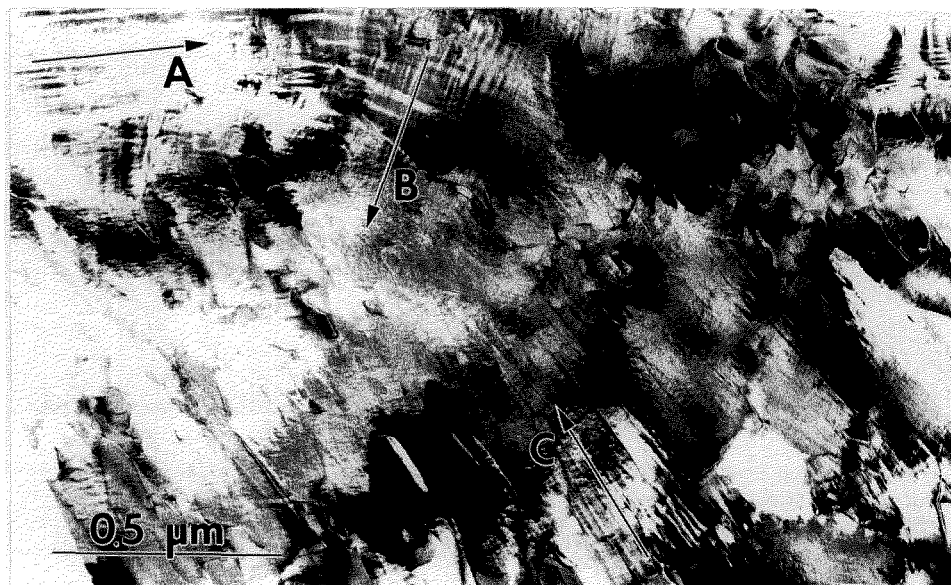


Fig. 14. Bright field image of a continuously cooled Alloy 1 specimen, slightly off the $[0001]$ zone axis, where all three orthogonal sets of the O phase variant pairs (shown as A, B and C) rotated with respect to each other by 60° are observed in a single grain.

preserves the average hexagonal symmetry and the ordering of the transient parent DO_{19} of path 3.1 as the SAD pattern in Fig. 15e shows.

Different dark field images (Fig. 15b, c, d) taken with the same diffuse 1100 reflection but in a slightly different TEM foil orientation reveal fine

scale domains and their interfaces (tilting changes the excitation errors for different domains). Therefore the diffuse reflections are in fact clusters of a few reflections very close to each other (additional diffuse intensities from the presence of a high density of interdomain interfaces and lattice strain

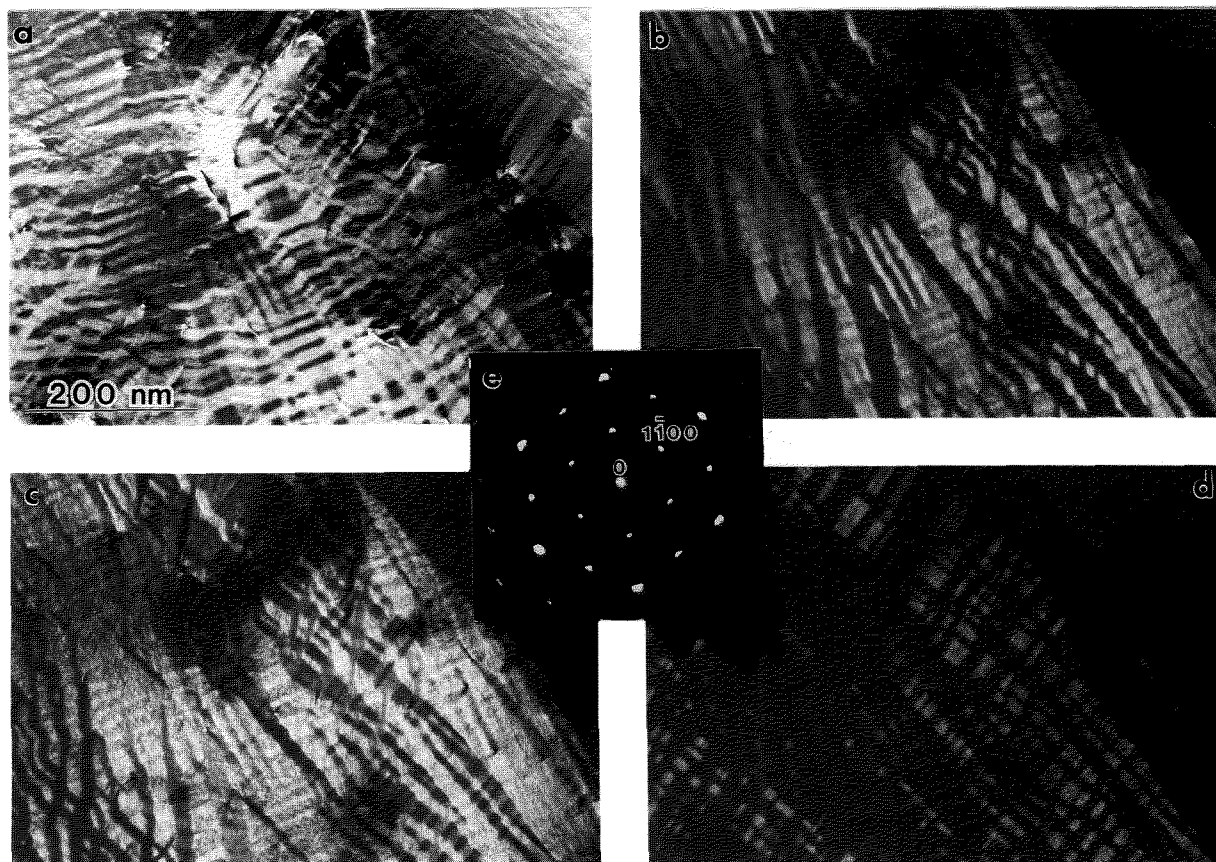


Fig. 15. Microstructure of the Alloy 1 after annealing at 700 °C for 26 d. Bright field (a) and three dark field (b–d) images, all slightly different in a TEM foil tilt, show a complex morphology of coherent domains.

make it difficult to resolve them). The SAD pattern, Fig. 15e, can be explained by a structure consisting of either three variants of the O phase formed from the DO₁₉ phase (as was observed in the specimens cooled from 1100 °C, Fig. 12) or co-existing domains of the O and DO₁₉ phases.

Because of experimental difficulties related to the similarity of the reciprocal lattices of the phases, the fineness of the domains and possible elastic distortions due to the coherency of interfaces, we were unsuccessful in providing direct TEM evidence of the identity and distribution of the phases. Analysis of the broadening and position of peaks in a neutron diffraction pattern obtained from a specimen similar to that of Fig. 15 has indicated the presence of both O and DO₁₉ phases (unpublished research, [19]). Indirect evidence for the phase constitution can be obtained by analyzing the possible orientations for strain-free coherent interfaces which would be expected between the O phase domain variants or between domains of the DO₁₉ phase and a variant of the O phase.

For a domain structure of the O phase formed from the DO₁₉ phase, as was shown in [1] and confirmed experimentally in Sec. 4.2, the interfaces have locked-in symmetry and have either $\{1\bar{1}00\}_h$ or $\{11\bar{2}0\}_h$ planes (of the average hexagonal lattice). For contacting domains of the O and DO₁₉ phases, the interface orientations depend on the lattice parameters at the temperature of formation, and in general are irrational (non-symmetric). Because the *c*-parameters of the O and DO₁₉ phases are similar [19,27], the interfaces are expected to contain the $[0001]_h$ direction.

Measurement of the directions of the interface traces with respect to the average hexagonal lattice in Fig. 15 are sufficient to establish a significant deviation from the $\{1\bar{1}00\}_h$ and $\{11\bar{2}0\}_h$ planes despite the relatively large measurement error due to the diffuseness and shortness of the interface segments. We consider this deviation as evidence for the existence of a coexisting two-phase mixture. Such non-symmetric interfaces are often seen lying parallel within a second level plate where the

neighboring second level plate also has non-symmetric parallel interfaces but with different orientation. The observation is illustrated in Fig. 16a, b where two dark field images (using the same cluster of reflections, $(4\bar{4}00)_h$, but with different small tilts of the TEM foil) show two second level plates, A and B, separately. The interface between them has a zigzag shape but on average is close to the $(11\bar{2}0)_h$ plane (Fig. 16c). The zigzag shape is formed by two segments of interfaces between the DO_{19} and O phase domains located in neighboring second level plates A and B. The segment planes also seem to be in irrational orientation. The interpretation of the distribution of domains and phases in the microstructure of Fig. 16 is depicted schematically in Fig. 17a,b. Another plausible two-phase morphology of domains with SFIs is shown schematically in Fig. 17c (and perhaps microstruc-

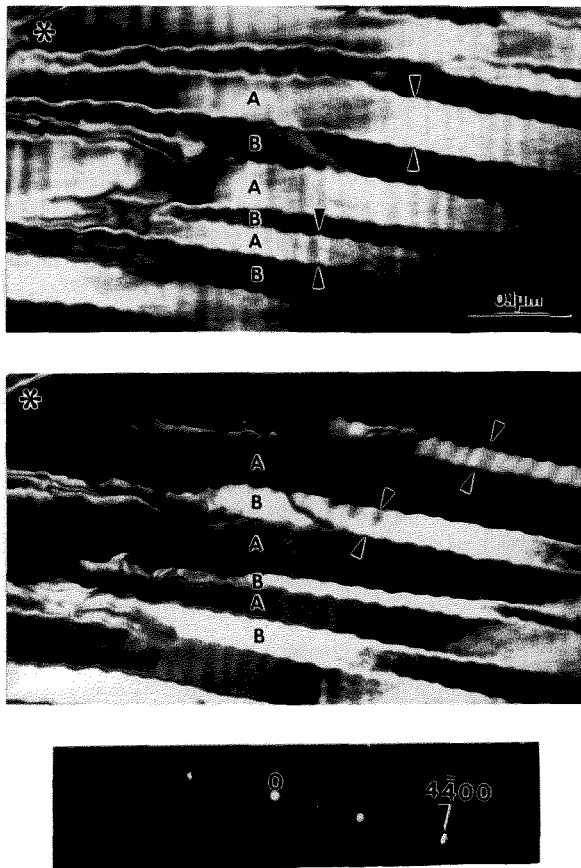


Fig. 16. Two dark field images, a and b, taken with the same cluster of reflections $(4\bar{4}00)_h$ (c) but different in a small tilt (close to $[0001]$) show two second level plates, A and B, separated by a zigzag shape interface close to the $(11\bar{2}0)_h$ plane. The zigzag shape is formed by two segments of interfaces between the DO_{19} and O phase domains located in neighboring second level plates A and B. The segment planes are irrational orientations.

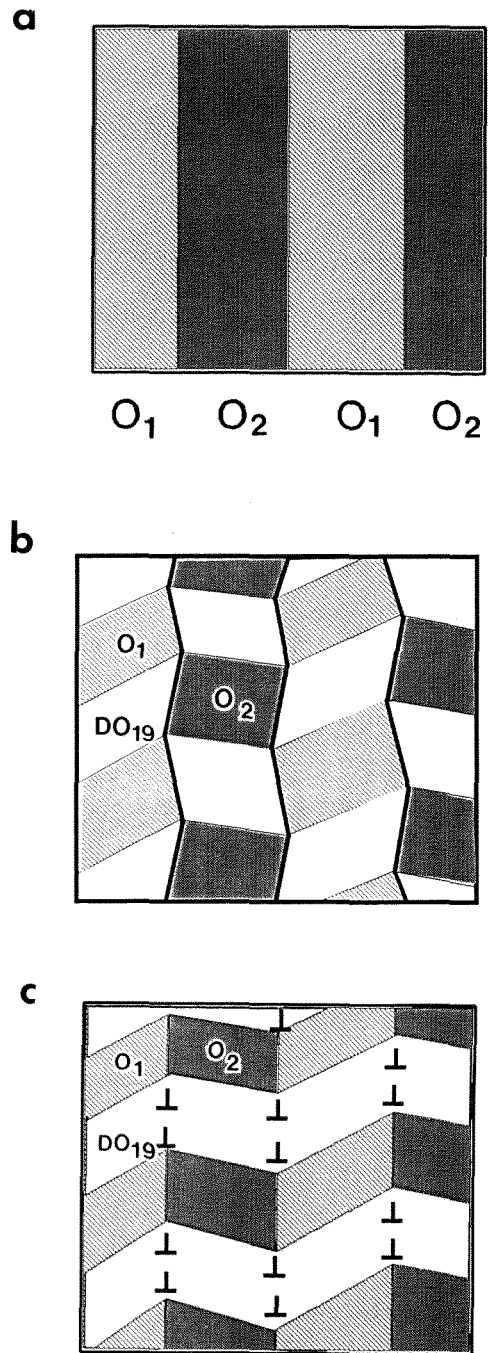


Fig. 17. Schematic drawing showing the two-phase (O and DO_{19}) domain distribution based on interpretation of the experimental images (Figs. 16, 17). The two-phase structure is formed by reprecipitation of the DO_{19} phase from the initial O phase twinned plates (a). Two morphologies are shown: (b) one with a chess-board distribution of domains surrounded by SFIs. (c) another with the DO_{19} phase forms zigzagged ribbons traveling continuously through the second level plates in a modulated manner. The DO_{19} phase ribbon-like domains have internal low angle boundaries (dislocation walls) and faceted SFIs with two variants of the O phase.

turally in Fig. 15). In this case the DO_{19} phase forms zigzag ribbons traveling continuously through the second level plates in a modulated manner. The DO_{19} phase ribbon-like domains have internal low angle boundaries (dislocation walls) and faceted SFIs with two variants of the O phase.

Therefore, the variety of interface orientations observed in Fig. 15 is due to the fact that the initial structure consisted of a three variant domain structure of the metastable O phase as seen in Fig. 14 (second level microstructure). Subsequent reformation of the hexagonal DO_{19} phase takes place in the plate-like structure of the O phase (corresponding to A and B plates in Fig. 16). The DO_{19} phase layers can have two equivalent stress-free habit planes for each variant of the O phase. The DO_{19} phase appears as a modulation of plates inside the orthorhombic phase domains. Because the 700 °C annealing results in reprecipitation of the DO_{19} phase, Alloy 1 is believed to be in an equilibrium two-phase field at this temperature.

6. Thermodynamics of Phase Formation

At the present time, neither the phase diagram nor its associated free energy functions are sufficiently well known to permit *a priori* prediction of the T_0 curves for the various BCC/B2 to close-packed transitions in the Ti_3Al-Nb_3Al pseudobinary section. These T_0 curves would provide the thermodynamic framework necessary to understand the partitionless transformations observed in the present work; viz., why there is a change in path from 1 to 2 for $(Ti,Nb)_3Al$ alloys as the Nb content is increased (from that of Alloy 1 to Alloys 2 and 3). However we can use the transformation path results of this paper, some knowledge of the ordering tendencies of BCC and HCP systems, and the limited phase diagram results from other researchers to construct a *self-consistent* pseudobinary section, a T_0 diagram, and a 700 °C free energy-composition diagram as shown in Fig. 18. It will be seen that paths including and excluding the intermediate HCP phase are quite reasonable. The construction of the three diagrams was performed concurrently, adjusting curves to be consistent with the details described below.

The free-energy composition diagram (Fig. 18c) should be viewed as a superposition of BCC-based ordering diagram (BCC and B2) and an HCP-based ordering diagram (HCP, DO_{19} , B19, and O). The relative heights (energies) of these two subsidiary diagrams have been adjusted to be consis-

tent with the fact that Nb is a beta (BCC) stabilizer, i.e., the HCP phase has a lower free energy at small Nb content than the BCC phase, and conversely at higher Nb content. In fact the intersection of the BCC and HCP free-energy curves (which gives the T_0 composition for the BCC to HCP transition) and the intersection of the BCC and B2 curve (which gives the composition for the BCC to B2 transition) were adjusted to agree with the experimental results of this paper. The individual BCC-based and the HCP-based free energy diagrams are sketched using reasonable assumptions about the ordering tendencies and preferred stoichiometries for the BCC- and HCP-based phases in this alloy system.

The BCC-based diagram is quite simple and consists of BCC and B2 curves. The BCC→B2 transition is assumed to be second order and thus the B2 free energy curve merges smoothly with that of the parent BCC curve and no two-phase BCC+B2 field exists in the phase diagram. (Thus the T_0 curve and the ordering critical curve are the same). It is reasonable to assume that the composition range of B2 stability exits at intermediate Nb content, probably centered around the Ti_2AlNb composition for the following reason. The two sublattices (or Wyckoff sites) of the B2 structures of Ti-Al-Nb are known to be preferentially occupied by Ti and a mixture of (Al,Nb) respectively (Ref. 21 in [1]). In the absence of competing non-BCC-based phases, the maximum order is most likely to be centered along the region of the ternary system where the atomic percent of Ti is equal to the sum of the atomic percents of Al and Nb. This region for maximum B2 order and hence for maximum stability intersects the $(Ti,Nb)_3Al$ section under consideration here at the Ti_2AlNb composition.³ The maximum in the ordering curve is 1400 °C or higher [15].

The free energy curves for the HCP-based phases, A3, B19, DO_{19} , and O, are more complex. The HCP→ DO_{19} , HCP→B19, B19→O and DO_{19} →O transitions are all required to be first order transitions under equilibrium conditions [28]. For first order transitions, shapes for free energy vs composition curves that contain end points and concave curvature have been described in detail by Soffa and Laughlin [5] and this shape was used for the orthorhombic ordering in Fig. 18c. The DO_{19} and

³ The possibility of achieving B2 order decreases as one moves from the TiAl composition to the TiNb composition because of the known positive heat of mixing of the BCC phase in the Ti-Nb binary.

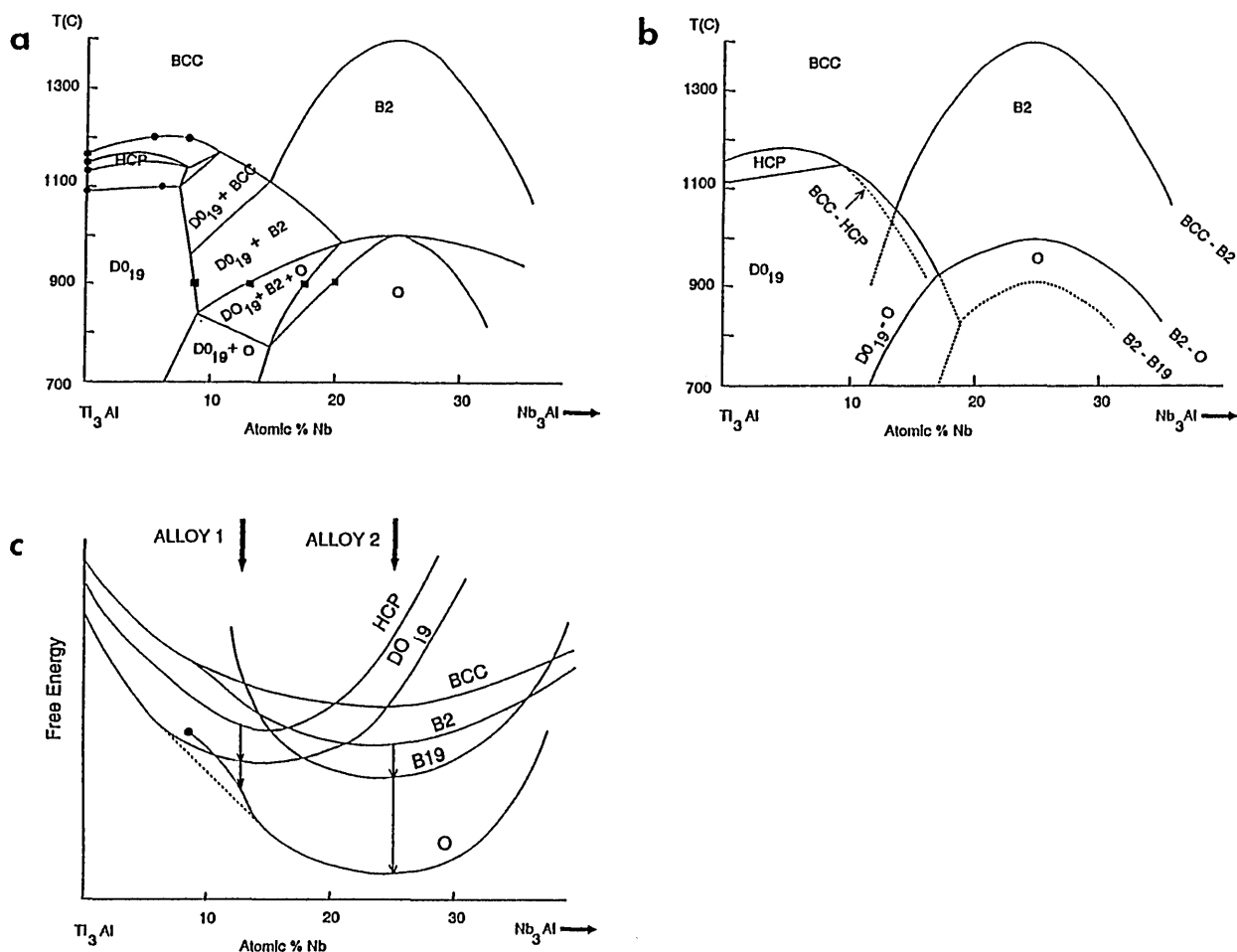


Fig. 18. Schematic (a) pseudobinary equilibrium phase diagram, (b) T_0 diagram for partitionless transformations, and (c) 700 °C free energy vs composition curves for the Ti_3Al - Nb_3Al section of the Ti-Al-Nb system. The free energy diagram shows the superposition of the BCC (B2) and HCP (DO_{19} , B19, and O-phase) families of phases. For Alloy 2, an intermediate HCP or DO_{19} phase cannot form during partitionless transformation from cubic to the O-phase.

orthorhombic Ti_2AlNb phases are assumed to be the equilibrium phases at 700 °C as indicated by the lowest common tangent, giving a tie line that would nearly lie in this pseudobinary section. Generally the tie lines will not lie in the $(\text{Ti,Nb})_3\text{Al}$ section. If, after cooling, an O phase alloy finds itself at a composition and temperature with a concave free energy curve, spontaneous growth of composition fluctuations can occur. If the local composition of a region of that alloy reaches the end point composition, then in that region the ordered phase will spontaneously disorder, in this case, to the DO_{19} phase.

The B19 phase is an AB phase having only two Wyckoff sites with occupancies similar to B2 and would therefore be expected to have maximum stability in the same composition region where the B2 phase has maximum stability, i.e., along the 50% Ti line, which intersects the $(\text{Ti,Nb})_3\text{Al}$ section near the Ti_2AlNb composition. Thus the B19 free energy

curve is centered around this composition as indicated in Fig. 18c. The B19 phase has never been observed as an equilibrium phase in this system and is thus metastable at all temperatures and compositions and does not appear in the phase diagram. Finally the site occupancy of the ordered A_2BC orthorhombic phase [19] clearly indicates that its compositional range of stability should also be centered around Ti_2AlNb .

The DO_{19} phase, an A_3B phase, is known to have a preference for Al on the B sites and a mixture of (Ti,Nb) on the A sites (Ref. 23 in [1]) in Ti-Al-Nb alloys. Thus stability of this phase with respect to HCP is expected across the entire $(\text{Ti,Nb})_3\text{Al}$ section at 700 °C and hence the free energy curve for DO_{19} is drawn below the HCP. Near the composition Ti_2AlNb , it is likely that the B19 phase would have a lower free energy than DO_{19} because of the presence of equal amounts of Al and Nb at this composition.

The pseudo-binary phase diagram section (Fig. 18a) was constructed using information on the BCC, HCP and DO_{19} equilibria from the calculated binary Ti-Al and from isothermal sections of Ti-Al-Nb at 1100 and 1200 °C [29]. The positions of phase boundaries between the DO_{19} , B2, and O phases at 900 °C were taken from the 900 °C isothermal section of Ref. 7 of [1]. The maximum in the B2 to O transition was placed at 1000 °C according to Ref. 25 of [1]. The remainder of the diagram was sketched to be consistent with Fig. 18 b, c.

The T_0 diagram (Fig. 18b) contains solid curves that correspond to the equilibrium two-phase fields in the phase diagram (Fig. 18a). The T_0 triple points (intersections of solid curves) correspond to three-phase triangular regions in the phase diagram.⁴ Also indicated are dashed extrapolations of the important BCC to HCP and BCC to B2 curves. A possible location for the T_0 curve for B2→B19 is also given. These dashed curves only have meaning if the high temperature BCC or B2 parent phase is retained for kinetic reasons during cooling through the higher T_0 curve(s).

We now discuss the observed results using these diagrams. Water-quenched samples of all three alloys in the present work are ordered B2. This rapid quench apparently suppresses the BCC→ DO_{19} and the BCC→HCP transformations for Alloy 1 and permits access to the BCC to B2 ordering curve at ~900 °C as shown in Fig. 18b. At a slower cooling rate (~400 K/s), the BCC→ DO_{19} transformation is bypassed for the kinetically simpler BCC→HCP transformation that requires only displacive ordering. Once the HCP phase forms, subsequent partitionless transformation to B2 is not possible. The formation of the HCP phase sets the stage for all of the subsequent transformations of Alloy 1. Alloys with higher Nb content can not escape ordering to the B2 at any cooling rate because the ordering temperature is relatively high. Indeed Alloy 2 is B2 at 1200 °C. The presence of the B2 phase sets the stage for the subsequent transformations of Alloys 2 and 3. For Alloys 2 and 3 the transformation BCC→HCP is not possible because of the way the T_0 curve plunges to low temperature.

For simplicity of discussion, the subsequent transformation paths for each alloy are considered as occurring isothermally at 700 °C as indicated by the arrows in Fig. 18c starting from the HCP for Alloy 1 and from the B2 for Alloys 2 and 3 follow-

ing the above discussion. The sequence for each alloy class undergoes partitionless transformation down a hierarchy of phases with decreasing free energy. One can see that for the alloys near the composition of Alloy 2, a B2→B19→O path is likely. On the other hand for alloys near the composition of Alloy 1, an HCP→ DO_{19} →O is likely. Thus we have constructed a set of thermodynamic relationships between the phases that is consistent with the experimentally observed paths for the partitionless transitions.

A later stage of transformation occurs for the low Nb content alloy shown in Fig. 18c that involves long-range diffusion. The concave curvature of the free energy curve indicates that the O phase formed for this composition by partitionless transformation is unstable on a longer time scale with respect to small fluctuations of composition (spinodal decomposition). This kind of process is termed conditional spinodal decomposition [3]. The Nb-poor regions of this decomposition will approach the end point of the O phase free energy curve and will spontaneously disorder (relative to the O phase) to the DO_{19} phase. This process is thought to lead to the third level of domain structure described in Sec. 5.

7. Conclusion

During cooling from 1100 °C, the high temperature BCC-based phase of $(Ti,Nb)_3Al$ alloys decomposes into low temperature orthorhombic phase by two different partitionless paths depending on Nb content. Microstructurally the two paths are differentiated by the substructure of domain boundaries and the number of variants of the orthorhombic phase. For alloys with ~12.5 at% Nb, the transient formation of a hexagonal precursor occurs while at ~25 at% Nb ordering to the B2 precludes the hexagonal phase. In the latter case, defects are found that suggest the transient existence of a B19 phase. However the B19 phase itself was never observed in cooled samples. In the former case formation of the O phase from the ordered DO_{19} was observed along with defects indicating the hexagonal to the DO_{19} ordering. These two different paths are seen as feasible after an examination of subgroup/supergroup relations between the crystal structures of the various phases. The paths are also feasible based on reasonable assumptions regarding the thermodynamic relationships among the free energy curves for the phases involved.

⁴ The intersection point of two T_0 curves necessarily requires the intersection of a third T_0 at the same point.

Detailed examination of the interfaces between the rotational domains/variants of the B2 to O phase transformation steps (for Alloys 2 and 3) and the DO₁₉ to O phase transformation steps (for Alloy 1) showed they are determined by the minimization of elastic strain energy through the formation of stress-free interfaces with special orientations of twins of the I and II kind. For the Alloy 2 and 3 the twins are often arranged in a self-accommodating polytwin group consisting of three variants of the O phase.

A two-phase modulated microstructure is observed after long term annealing at 700 °C of the Alloy 1. The structure morphology is determined first by a formation of the metastable O phase (by congruent ordering of the DO₁₉ phase), and then by reprecipitation of the DO₁₉ phase. The thermodynamics underlying the two-phase formation, possibly by a spinodal mechanism, are discussed.

Acknowledgment

The authors would like to thank F. S. Biancianiello for the alloy melting and the heat treatments and M. E. Williams for the TEM specimen preparation and the photographic work. The support of DARPA under Order #7469 is greatly appreciated.

8. References

- [1] L. A. Bendersky, A. Roytburd, and W. J. Boettinger, *J. Res. Natl. Inst. Stand. Technol.* **98**, 561 (1993).
- [2] L. D. Landau and E. M. Lifshitz, *Statistical Physics*, Pergamon Press, London (1980).
- [3] S. M. Allen and J. W. Cahn, *Acta Met.* **23**, 1017 (1975); **24**, 425 (1976).
- [4] A. G. Khachatryan, T. F. Lindsey, and J. W. Morris, *Metall. Trans.* **19A**, 249 (1988).
- [5] W. A. Soffa and D. E. Laughlin, *Acta Met.* **37**, 3019 (1989).
- [6] R. A. Spurling, *Met. Trans.* **6A**, 1660 (1975).
- [7] G. M. Pennock, H. M. Flower, and D. R. F. West, *Metallography* **10**, 43 (1977).
- [8] D. Banerjee and J. C. Williams, *Scr. Met.* **17**, 1125 (1983).
- [9] D. Banerjee, C. G. Shelton, B. Ralph, and J. C. Williams, *Acta Met.* **36**, 125 (1988).
- [10] D. S. Shih, G. K. Scarr, and G. E. Wasielewski, *Scr. Met.* **23**, 973 (1989).
- [11] K. Muraleedharan, S. V. Nagender Naidu, and D. Banerjee, *Scr. Met.* **24**, 27 (1990).
- [12] R. A. Spurling, C. G. Rhodes, and J. C. Williams, *Met. Trans.* **5**, 2597 (1974).
- [13] H. J. Rack, D. Kalish, and K. D. Fike, *J. Mater. Sci. Eng.* **6**, 181 (1970).
- [14] R. A. Spurling, private communication.
- [15] L. A. Bendersky and W. J. Boettinger, *Mat. Res. Soc. Symp. Proc.*, Vol. 133, p. 45 (1989); L. A. Bendersky, W. J. Boettinger, and A. Roitburd, *Acta Met.* **39**, 1959 (1991).
- [16] See papers in ASM Symposium on Pretransformation Behavior Related to Displacive Transformations, L. E. Tanner and W. A. Soffa, Eds., *Metall. Trans.* **19A** (1988).
- [17] R. Strychor, T. C. Williams, and W. A. Soffa, *Met. Trans.* **19A**, 1321 (1988).
- [18] L. A. Bendersky, W. J. Boettinger, B. Burton, F. S. Biancianiello, and C. B. Shoemaker, *Acta Metall. Mater.* **38**, 931 (1990).
- [19] B. Mozer, L. A. Bendersky, W. J. Boettinger, and R. G. Rowe, *Scr. Met.* **24**, 2363 (1990); B. Mozer, unpublished research, NIST, Gaithersburg, 1991.
- [20] Z. Nishiyama, *Martensitic Transformation*, Academic Press (1978).
- [21] D. S. Liberman in *Phase Transformations*, ASM (1970) p. 1.
- [22] T. Saburi and C. M. Wayman, *Acta Metall.* **27**, 979 (1979).
- [23] S. Ichinose, Y. Funatsu, and K. Otsuka, *Acta Metall.* **33**, 1613 (1985).
- [24] F. C. Lovey, G. van Tendeloo, and S. Amelinckx, *Phys. Stat. Sol.* **85**, 29 (1984).
- [25] W. A. Baeslack III and T. Broderick, *Scr. Met.* **24**, 319 (1990).
- [26] M. J. Marcinkowski in *Electron Microscopy and Strength of Crystals*, eds. G. Thomas and J. Washburn, Interscience, New York (1962), p. 333.
- [27] H. T. Kestner-Weykamp, C. H. Ward, T. F. Broderick, and M. J. Kaufman, *Scr. Met.* **23**, 1697 (1989).
- [28] M. A. Krivoglaz and A. A. Smirnov, *The Theory of Order-Disorder in Alloys*, American Elsevier Publishing Co., New York (1965) p. 120.
- [29] U. R. Kattner and W. J. Boettinger, *Mat. Sci. Eng.* **A152**, 9 (1992).

About the authors: L. A. Bendersky and W. J. Boettinger are metallurgists in the Metallurgy Division of the NIST Materials Science and Engineering Laboratory. The National Institute of Standards and Technology is an agency of the Technology Administration, U.S. Department of Commerce.

Corrosion Characteristics of Silicon Carbide and Silicon Nitride

Volume 98

Number 5

September–October 1993

**R. G. Munro and
S. J. Dapkunas**

National Institute of Standards
and Technology,
Gaithersburg, MD 20899-0001

The present work is a review of the substantial effort that has been made to measure and understand the effects of corrosion with respect to the properties, performance, and durability of various forms of silicon carbide and silicon nitride. The review encompasses corrosion in diverse environments, usually at temperatures of 1000 °C or higher. The environments include dry and moist

oxygen, mixtures of hot gaseous vapors, molten salts, molten metals, and complex environments pertaining to coal ashes and slags.

Key words: ash; ceramics; coal; corrosion; silicon carbide; silicon nitride; slag.

Accepted: May 25, 1993

1. Introduction

The present work is a review of the substantial effort that has been made to measure and understand the effects of corrosion with respect to the properties, performance, and durability of various forms of silicon carbide and silicon nitride. These materials are the primary candidates for the materials to be used in the development of heat exchangers for the Department of Energy's Combustion 2000 program. The review encompasses corrosion in diverse environments, usually at temperatures of 1000 °C or higher. The environments include dry and moist oxygen, mixtures of hot gaseous vapors, molten salts, molten metals, and complex environments pertaining to coal ashes and slags.

The potential applications of advanced structural ceramics have been widely appreciated for several decades [1]. Characteristics such as high maximum use temperature, strength retention at high temperature, and chemical stability have held forth tantalizing possibilities [2,3] for more efficient engines [4], heat exchangers and recuperators [5,6]

and for more durable electronic packaging [7] and chemical processing components [8]. The primary barriers that have impeded [9] the widespread development of these applications have been the susceptibility of structural ceramics to brittle fracture [10] and environmentally sensitive corrosion behavior [11], including the subsequent effects of corrosion on the thermal and mechanical performance of ceramics. The former barrier has received, by far, the greater amount of attention [12]. The corrosion of advanced ceramics, however, has proven to be a complex problem and has been recognized as a critical consideration in attaining high efficiency applications [13].

A schematic illustration of the corrosion process is shown in Fig. 1. The bulk ceramic material usually may be assumed to have a film or scale on its surface that differs chemically from the bulk material. For either silicon carbide or silicon nitride, the film is usually a critically important silica layer. The bulk ceramic and its surface scale form a solid body that is exposed to a hot, flowing,

gaseous environment which may also contain fine particulate matter and from which a deposit may form on the solid body. This deposit may exist in a crystalline, glassy, or molten form at the principal exposure temperature.

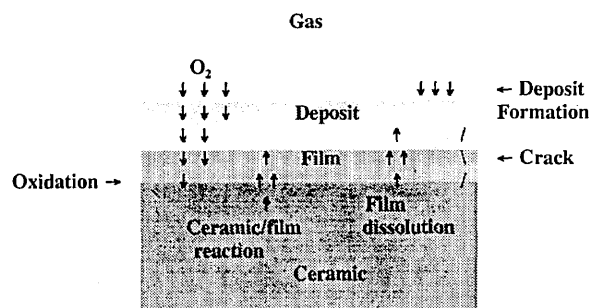


Fig. 1. Schematic illustration of various mechanisms involved in the corrosion of a ceramic material.

In this simple schematic, the corrosion process already can be seen to involve the possibility of a complex series of chemical reactions whose time-dependent course may be influenced by thermal and mechanical properties of the substrate, as well as the chemical composition of the environment. The diffusion of oxygen from the gaseous region to the ceramic, where oxidation can replenish the protective scale, may be dependent on the nature of the deposit, its density, and its thickness. Likewise, the direct and deleterious reaction between the deposit and the bulk ceramic may become possible through the formation of cracks in the protective film as a result of thermal stress gradients, the dissolution of the film in a molten deposit, and localized stress enhancement resulting from the evolution of gaseous reaction products at the interface of the ceramic and film.

The process illustrated by Fig. 1 represents the current view of the corrosion of silicon carbide quite well. For silicon nitride, the oxide scale is actually a double or duplex layer in which an intermediate phase of silicon oxynitride occurs between the outer silica scale and the silicon nitride substrate [14]. Details of the contributing and competing reactions, the formation kinetics, and the physical consequences of the corrosion process are reviewed in the following sections.

2. SiC

The reaction sequences for the corrosion of a material may be strongly affected by either the

major or the minor components of its composition, and the rate of corrosion may be affected by the microstructure of the material. The composition determines what chemical species are available for reaction, and the structure determines how accessible the species are for the potential reactions. Consequently, understanding the corrosion of a material presupposes an understanding of the composition and structure of the material.

Crystalline silicon carbide exists in a large variety of polymorphic forms, or polytypes, that are broadly divided into two classes, α -SiC and β -SiC. The β -SiC class has a cubic structure, while the α -SiC class consists of hexagonal and rhombohedral noncubic structures. All of the varieties of SiC are formed by hexagonal layers of silicon atoms and hexagonal layers of carbon atoms arranged in various stacking patterns that result in each silicon atom being surrounded tetrahedrally by four carbon atoms, and each carbon atom being surrounded tetrahedrally by four silicon atoms. Specific varieties are commonly designated by a notation that (1) specifies the number of layers in the repeating unit and (2) indicates the symmetry of the crystallographic cell by a letter: C for cubic, H for hexagonal, and R for rhombohedral. The forms frequently noted in the literature include the cubic form, 3C of the β -SiC class, and the noncubic forms 2H, 6H, and 15R of the α -SiC class.

Powders in the β -SiC form may be produced at relatively low temperature, 1500–1600 °C, using polycarbosilanes and polyborosiloxanes in polymer conversion reactions [18], gaseous mixtures of silane, hydrogen chloride, propane, and hydrogen in vapor phase reactions [19], or low-temperature carbothermic reduction of silica and carbon with boron and titanium as additives [20]. The production of α -SiC is usually conducted at temperatures above 2500 °C and is most commonly produced using the carbothermic method known as the Acheson process [21]. Gas phase synthesis can also be used to produce α -SiC. At temperatures above 2000 °C, β -SiC may convert to α -SiC.

Bulk SiC ceramics are usually derived from SiC powders using various processing stages. As a result, SiC ceramics are generally polycrystalline materials that may consist of more than one polytype of SiC plus additional material phases resulting from the use of sintering aids or other components of the starting powders. The processing of the powders usually involves sintering, hot pressing, or reaction bonding. The sintering or hot pressing of SiC commonly requires the use of sintering aids such as boron or aluminum or their

oxide, nitride, or carbide compounds. In the reaction bonding technique, carbon, silicon metal, silicon nitride, or other powders may be mixed with silicon carbide powder and allowed to react at high temperature. The resulting ceramic is generally a multiphase material that also may have a bimodal SiC grain size distribution.

It is evident that silicon carbide materials that are nominally the same may have significantly different impurities, grain size distributions, grain boundary phases, and types and extent of porosity. These differences are significant in the context of corrosion because of their influence on the possible reaction sequences, the diffusion rates of the reactants and products, and the occurrence of either localized pitting or uniform surface recession.

2.1 Oxidation of SiC

The oxidation of SiC has been a subject of considerable interest for many decades [24]. Over this period, the research efforts have shown a progression from studies of the coarser aspects of oxidation to more detailed investigations of contributing mechanisms. It was noted in an early work that the formation of SiO₂ on the surface, Fig. 2, was probably the rate-controlling process in the normal oxidation of SiC [25]. According to the free energy changes, Table 1, the formation of SiO₂ should result predominantly from the reaction

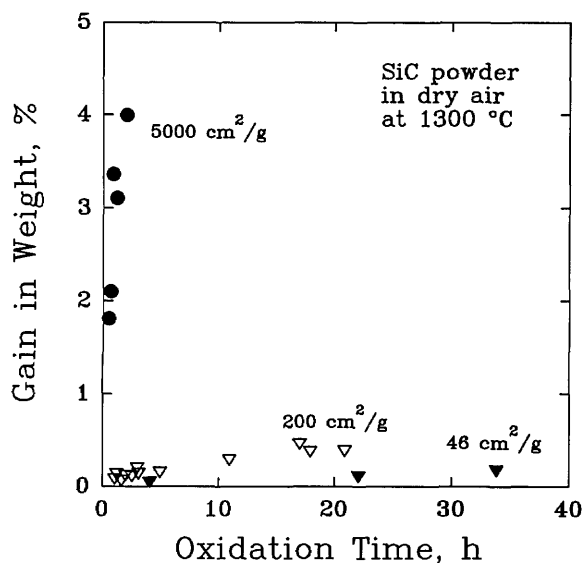
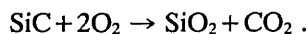


Fig. 2. The oxidation of SiC powders, of various specific surface areas, in dry air at 1300 °C. (After G. Ervin, Jr., J. Am. Ceram. Soc. 44 (9), 347–352 (1958).)

Table 1. Reactions of SiC with O₂ and associated free energy changes, ΔF^a

	ΔF (kJ/mol)	
	25 °C	1627 °C
SiC + 2 O ₂ → SiO ₂ + CO ₂	– 1168.0	– 901.2
SiC + (3/2) O ₂ → SiO ₂ + CO	– 910.9	– 783.2
SiC + O ₂ → SiO ₂ + C	– 773.6	– 505.0
SiC + (3/2) O ₂ → SiO + CO ₂	– 460.7	– 604.6
SiC + O ₂ → SiO + CO	– 203.3	– 486.6
SiC + (1/2) O ₂ → SiO + C	– 66.1	– 208.4
SiC + O ₂ → Si + CO ₂	– 342.7	– 361.9
SiC + (1/2) O ₂ → Si + CO	– 85.4	– 243.9

^a After G. Ervin, Jr., J. Am. Ceram. Soc. 44 (9), 347–352 (1958).

In that same work, a weight loss, rather than a weight gain, was observed, Table 2, when SiC was heated in a vacuum. The suggestion was made that the formation of SiO gas was most likely responsible for the latter result, primarily from the reaction

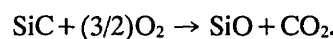
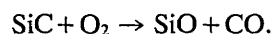


Table 2. The oxidation of high purity, 100–200 mesh SiC at low pressure^a

Air pressure (Pa)	Temperature (°C)	Exposure	
		time (h)	Mass change (%)
0.001	1600	16	– 4.2
0.133	1600	17	– 19.9
13.332	1440	4	– 2.5

^a After G. Ervin, Jr., J. Am. Ceram. Soc. 44 (9), 347–352 (1958).

In a later investigation of the kinetics of SiC oxidation, the oxidation process was resolved into passive and active processes as was done for the oxidation process of silicon [26]. The occurrence of a passive oxidation process, involving weight gain, or an active oxidation process, involving weight loss, Table 3, depended on the magnitude of the oxygen partial pressure [27]. The weight loss was again related to the formation of SiO gas, but the key reaction producing the SiO gas was thought to be



More generally, for a given temperature, it was found that the oxidation of SiC was passive unless the partial pressure of oxygen was less than a critical value. Alternatively, for a given partial pressure of oxygen, an active-to-passive transition temperature could be defined, Table 4, such that passive oxidation would occur at temperatures less than the transition temperature, while active oxidation would occur at higher temperatures [28].

Table 3. Oxidation rate of high purity SiC^a

Pressure (Pa)	Temperature (°C)	O ₂ Flow rate (10 ¹⁷ molecules per second)	Mass gain (μg/s)
1.2	1150	1.02	0.04
1.2	1200	1.32	0.05
1.2	1200	0.64	0.02
1.2	1250	1.10	-0.19
1.2	1300	1.13	-1.56
1.2	1350	1.04	-1.65
1.2	1400	0.62	-1.31
5.3	1150	8.4	0.52
5.3	1200	7.4	0.06
5.3	1250	10.5	0.97
5.3	1300	8.7	-0.75
5.3	1350	9.3	-0.86
5.3	1400	8.1	-5.22
13.3	1150	52.5	3.6
13.3	1200	56.5	0.2
13.3	1250	56.5	0.8
13.3	1300	56.5	0.2
13.3	1350	64.0	3.9
13.3	1400	66.5	-9.3
66.7	1150	6.3	0.2
66.7	1250	8.0	1.1
66.7	1300	7.6	0.6
66.7	1350	8.4	4.8

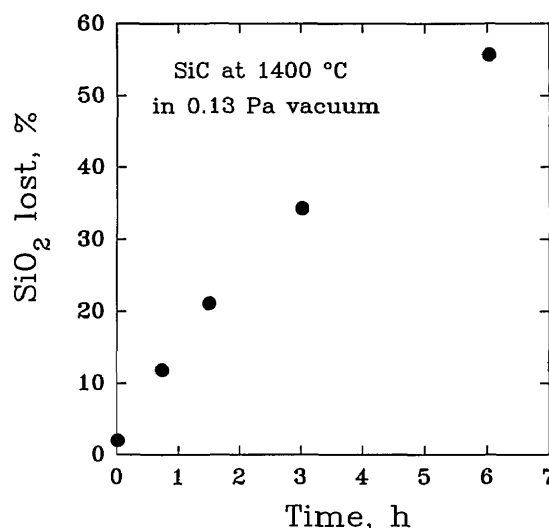
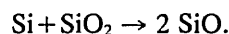
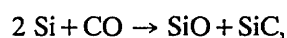
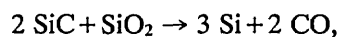
^a After E. A. Gulbransen et al., *J. Electrochem. Soc.* **113** (12), 1311–1314 (1966).

Table 4. Active-to-passive transition temperature, T_{ap} , for sintered α -SiC at various values of the partial pressure of oxygen, $P(O_2)^a$

Flow rate (cm ³ /s)	$P(O_2)$ (Pa)	T_{ap} (°C)
1.66	18.2	1403
1.66	18.8	1405
1.66	65.8	1532
1.66	125.1	1542
0.83	10.2	1389
0.83	55.6	1496
0.83	123.2	1543
0.56	7.3	1373
0.56	16.8	1392
0.56	61.6	1507
0.17	2.5	1347
0.17	17.6	1372
0.17	57.4	1468
0.17	115.9	1532

^a After W. L. Vaughn et al., *J. Am. Ceram. Soc.* **73** (6), 1540–1543 (1990).

An additional complication was noted in another high temperature study of kinetics where it was found that the oxide layer itself could react with SiC, Fig. 3, resulting in a loss of SiO₂ along with the production of SiO gas [29] by the reaction sequence:

**Fig. 3.** The reaction of silica with silicon carbide in vacuum at 1400 °C. (After W. W. Pultz et al., *Trans. Farad. Soc.* **62**, 2499–2504 (1966).)

From these early works, it rapidly became clear that the oxidation mechanisms for SiC were quite complex, and that understanding the mechanisms would require careful examination of the phase equilibria relations among the primary constituents and reaction products [30,31,32]. Further, it was noted that there were large, quantitative differences among the results of kinetics studies that had to be explained, such as the variation of activation energies by an order of magnitude and the occurrence of time-dependent oxidation mechanisms as suggested by Fig. 4. Thus, the roles of materials processing [33,34,35,36], Table 5, and specific molecular transport mechanisms [37,38], had to be considered as integral parts of the analysis of the oxidation of SiC.

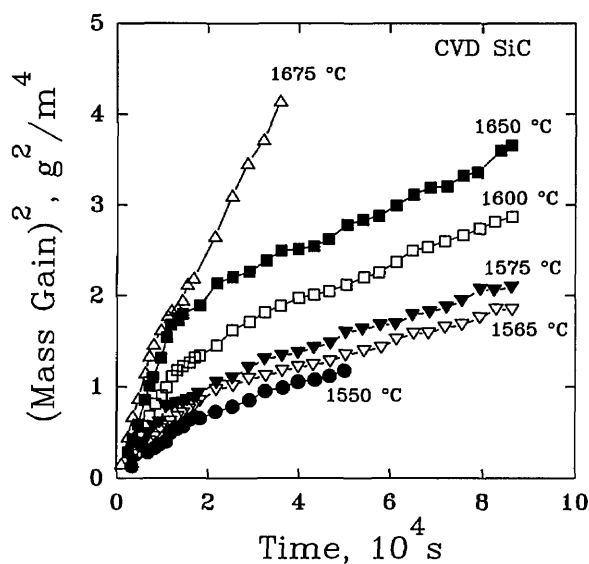


Fig. 4. The oxidation of CVD-SiC showing a two-step parabolic oxidation process. (After T. Narushima et al., J. Am. Ceram. Soc. **72** (8), 1386–1390 (1989).)

Table 5. Parabolic rate parameters, K_{par} , and activation energies, E_{act} , for the oxidation of SiC in dry oxygen.^a SCSC=single crystal SiC; BL=black; F=fast growth face; SL=slow growth face; GR=green; CNTD=controlled nucleation thermal deposition SiC; SASC=sintered α -SiC; HPSC=hot pressed SiC

Material	Temperature (°C)	K_{par} (nm ² /min)	E_{act} (kJ/mol)
SCSC BL F	1200	712 ± 58	134–197
	1300	620 ± 36	
	1400	1040 ± 76	
	1450	1920 ± 61	
	1500	2310 ± 395	
	1200–1500		
SCSC BL SL	1200	19 ± 5	372
	1300	175 ± 91	
	1400	848 ± 228	
	1450	1640 ± 412	
	1500	1770 ± 278	
	1200–1500		
SCSC GR F	1200	346 ± 47	121–297
	1300	658 ± 38	
	1400	1150 ± 160	
	1450	2310 ± 1060	
	1500	3840 ± 1040	
	1200–1500		
SCSC GR SL	1200	41 ± 6	339
	1300	331 ± 72	
	1400	943 ± 179	
	1450	2860 ± 784	
	1500	4970 ± 793	
	1200–1500		

Table 5. Parabolic rate parameters, K_{par} , and activation energies, E_{act} , for the oxidation of SiC in dry oxygen.^a SCSC=single crystal SiC; BL=black; F=fast growth face; SL=slow growth face; GR=green; CNTD=controlled nucleation thermal deposition SiC; SASC=sintered α -SiC; HPSC=hot pressed SiC—Continued

Material	Temperature (°C)	K_{par} (nm ² /min)	E_{act} (kJ/mol)
CNTD	1200	344 ± 53	142–293
	1300	745 ± 203	
	1400	1370 ± 255	
	1450	2690 ± 537	
	1500	4510 ± 758	
	1200–1500		
SASC	1200	175 ± 87	217–289
	1300	540 ± 71	
	1400	949 ± 272	
	1450	1770	
	1200–1450		
HPSC	1200	220 ± 82	221
	1300	695 ± 211	
	1400	1860	
	1200–1400		

^a After Costello et al., J. Am. Ceram. Soc. **69** (9), 674–681 (1986).

Finally, it was recognized that the mechanical performance of a corroded material could be significantly different from the original, uncorrupted material. The principal concern was that the brittle failure behavior of a ceramic could be affected by changes in the surface, or near surface, flaw population. Passive oxidation could, in fact, have a beneficial effect by healing surface cracks and increasing the average flexural strength, while active oxidation could lead to new surface flaws that would decrease the average flexural strength [39]. The roles of material processing and composition were found to be important factors for both the distribution of strength [40], Tables 6 and 7, and the retention of strength, Fig. 5, under long-term exposures to oxidizing environments [41]. Time-dependent effects such as creep and slow crack growth were also noted as important factors in determining high-temperature materials reliability [42].

2.2 SiC in Hot Gases

The potential applications of silicon carbide include metal and chemical processing industries, coal gasification, and various heat treatment applications that frequently contain H₂, H₂O, and N₂ at

temperatures above 1000 °C. Under these gases, the protective silica layer may deteriorate, Fig. 6, thereby exposing the SiC to active oxidation. Under gaseous H₂, solid silica may be reduced to gaseous products by the reaction [43]:

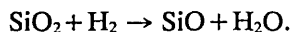


Table 6. Room temperature Weibull parameters, σ_0 and m from four-point bend tests of oxidized silicon carbide; SASC = sintered α -SiC; HPSC=hot pressed SiC. σ_{ave} is the average bend strength, and R^2 is squared correlation coefficient of the least squares fit to the data^a

Material	Static load (MPa)	Ox. time (h)	σ_{ave} (MPa)	σ_0 (MPa)	m	No. of samples	R^2
SASC	0	0.0	575	130	6.8	50	0.97
	0	0.5	600	176	8.3	11	0.95
	0	1.0	580	175	8.4	55	0.95
	0	12.0	560	227	11.4	10	0.92
	0	20.0	555	228	11.5	11	0.93
	0	50.0	570	220	10.7	11	0.95
	160	1.0	500	134	7.7	28	0.98
	330	1.0	540			21	
HPSC	0	0.0	550	177	8.9	49	0.95
	0	0.5	605	218	9.9	11	0.97
	0	1.0	845	279	9.1	49	0.98
	0	12.0	620	252	11.4	11	0.94
	0	20.0	670	361	16.6	10	0.91
	0	50.0	700	502	30.9	10	0.95
	190	1.0	735			15	
	270	1.0	845	277	9.1	15	0.98

^a After Easler et al., J. Am. Ceram. Soc. 64, (12), 731–734 (1981).

Table 7. Weibull parameters, σ_0 and m , from four-point bend tests of siliconized silicon carbide materials oxidized in dry O₂ at 1150 °C. σ_{ave} is the average bend strength \pm one standard deviation, and R^2 is squared correlation coefficient of the least squares fit to the data^a

Material	Oxidation time (h)	Bend test temperature (°C)	σ_{ave} (MPa)	σ_0 (MPa)	m	R^2	
NC430	0	25	203 \pm 15	210	13.7	0.94	
	0	1000	213 \pm 16	222	12.6	0.94	
	0	1150	213 \pm 14	220	14.9	0.95	
	0	1300	214 \pm 9	219	21.1	0.85	
	10	1000	234 \pm 15	242	15.1	0.96	
	10	1150	222 \pm 16	230	13.2	0.93	
	10	1300	222 \pm 12	228	17.7	0.95	
	50	1000	221 \pm 23	232	9.2	0.99	
	50	1150	224 \pm 17	233	12.5	0.79	
	50	1300	228 \pm 17	237	13.3	0.97	
	HD530	0	25	165 \pm 13	172	12.6	0.99
		0	1000	170 \pm 16	178	10.4	0.95

Table 7. Weibull parameters, σ_0 and m , from four-point bend tests of siliconized silicon carbide materials oxidized in dry O₂ at 1150 °C. σ_{ave} is the average bend strength \pm one standard deviation, and R^2 is squared correlation coefficient of the least squares fit to the data^a—Continued

Material	Oxidation time (h)	Bend test temperature (°C)	σ_{ave} (MPa)	σ_0 (MPa)	m	R^2
CS101K	0	1150	179 \pm 18	187	9.6	0.96
	0	1300	190 \pm 17	198	11.2	0.94
	10	1000	161 \pm 11	167	14.8	0.98
	10	1150	171 \pm 12	177	13.9	0.87
	10	1300	195 \pm 8	199	24.6	0.96
	50	1000	58 \pm 6	161	25.9	0.97
	50	1150	174 \pm 13	180	12.8	0.94
	50	1300	189 \pm 13	195	13.7	0.96
	0	25	224 \pm 44	243	5.3	0.95
	0	1000	234 \pm 14	242	14.6	0.87
	0	1150	215 \pm 15	223	14.0	0.98
	0	1300	225 \pm 13	231	16.3	0.80
10	1000	242 \pm 18	250	13.1	0.95	
10	1150	213 \pm 19	223	10.8	0.99	
10	1300	232 \pm 8	236	27.6	0.92	
50	1000	244 \pm 17	257	8.6	0.97	
50	1150	222 \pm 17	230	12.9	0.95	
50	1300	253 \pm 17	262	13.0	0.75	

^a After Y. Tsai et al., EM-5274, Final Report for Research Project 2260-2, Electric Power Research Institute (1987).

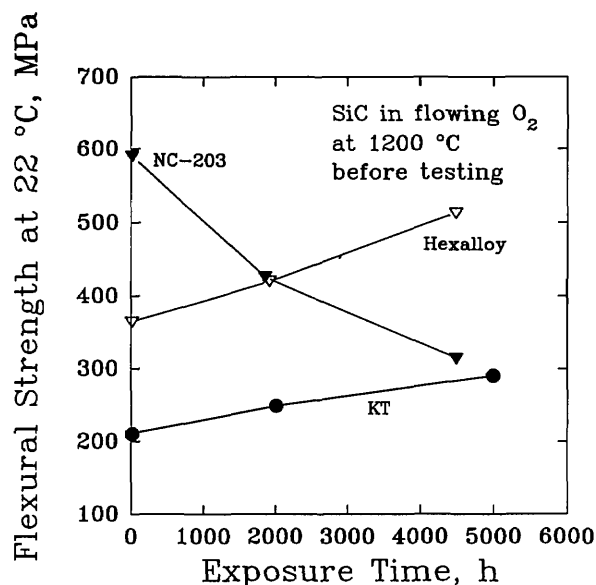


Fig. 5. The room-temperature flexural strength of commercial silicon carbide materials after the materials were exposed to flowing oxygen at 1200 °C. (After P. F. Becher, J. Am. Ceram. Soc. 66 (8), C-120–C-121 (1983).)

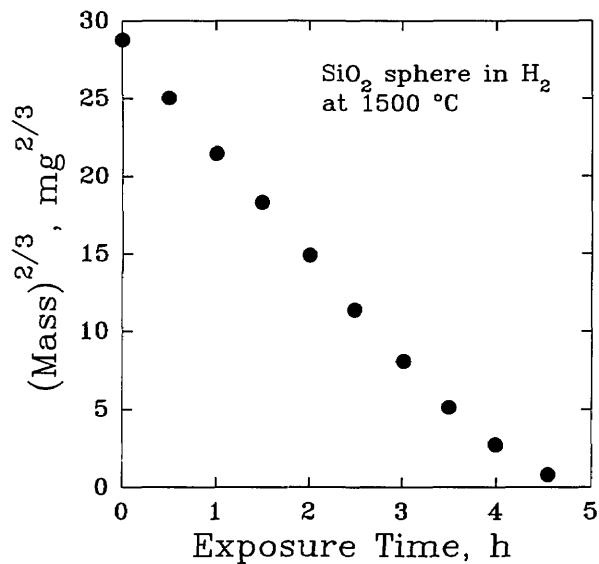
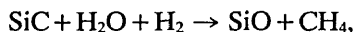
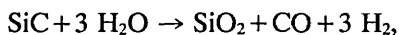


Fig. 6. The hydrogen reduction of silica at 1500 °C. (After D. W. Readey, *Ceram. Trans.* 10, 53-80 (1989).)

In the presence of gaseous H₂O, the solid SiC may experience active oxidation according to [44]:

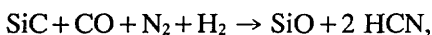


The primary consequence of such reactions is not the reduced thickness of the component, but rather the increased population of surface flaws that result from the loss of silicon in the form of gaseous SiO. The strength of the material generally decreases as the population of surface flaws increases. Results on the flexural strength of sintered α-SiC, Fig. 7, indicate that when the partial pressure of H₂O is sufficiently large, the formation of a protective silica layer by the reaction:



may become dominant among the various possible reactions between SiC and H₂O.

Nitrogen-containing environments, Fig. 8, may also result in the active oxidation of SiC [45]. At low gas pressure, SiC may be lost according to:



while at higher pressures, the reaction products may involve solid carbon, silicon nitride, or silicon

oxynitride:

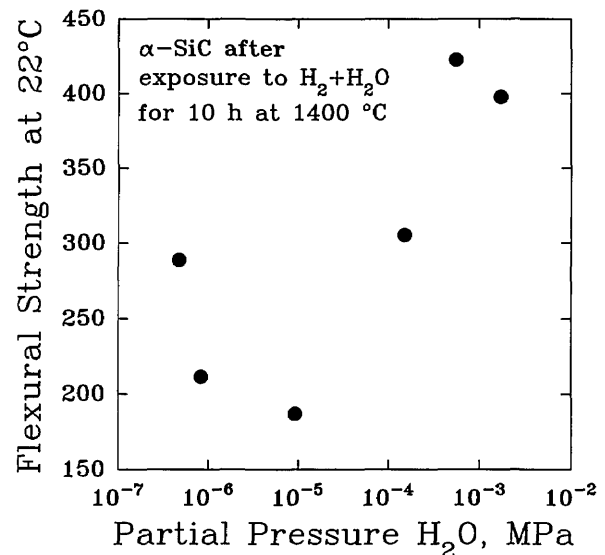
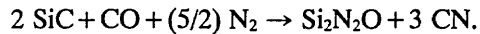
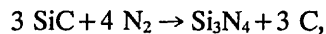
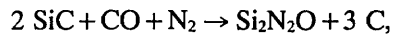


Fig. 7. The variation of the room-temperature flexural strength of sintered α-SiC under hydrogen gas with various partial pressures of H₂O for 10 h at 1400 °C. (After H. Kim et al., *Ceram. Trans.* 10, 81-96 (1989).)

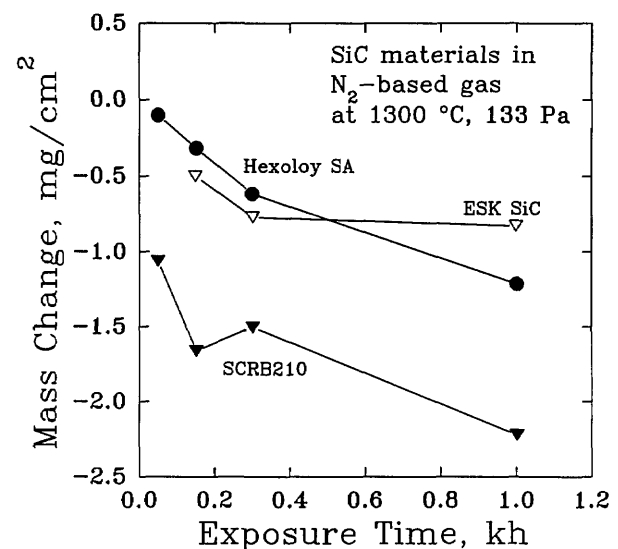
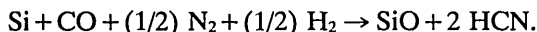
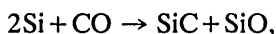


Fig. 8. Changes in the mass of commercial silicon carbide materials heated in a nitrogen gas (98.2 vol % N₂) at 1300 °C. (After D. P. Butt et al., *CAM Newslett.* 5 (1), 1 (1991).)

Siliconized SiC may also experience a selective attack against the silicon phase according to:



In each of these cases, the strength of the material, Fig. 9, can be affected adversely.

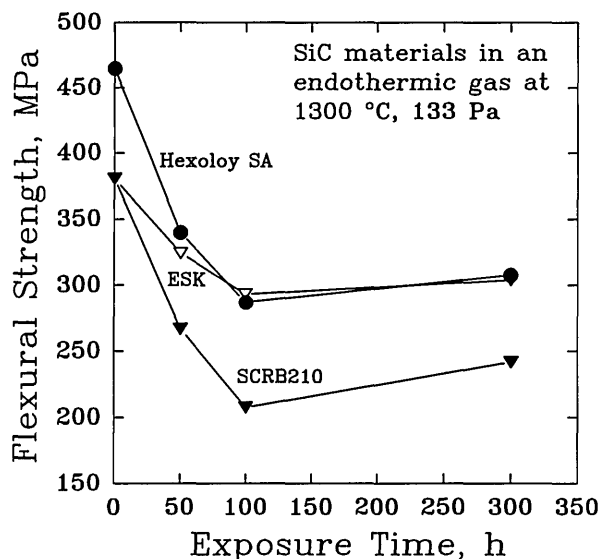


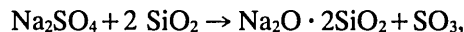
Fig. 9. The variation of the room-temperature flexural strength of commercial silicon carbide materials after exposure to an endothermic gas (41.1 vol% H₂, 37.8 vol% N₂, 21.1 vol% CO) at 1300 °C. (After D. P. Butt et al., CAM Newslett. 5 (1), 1 (1991).)

2.3 SiC in Molten Salts

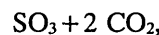
Materials used in industrial flue gases, gas turbine environments, aluminum remelting operations, and coal gasification conditions may be exposed to molten salts such as Na₂SO₄ and Na₂CO₃ which promote the deterioration of the silica layer [46]. The dissolution of the silica layer by Na₂CO₃ is thermodynamically favorable and may proceed directly according to the reaction



with a free energy change of -79.9 kJ/mol [47]. In high concentrations, Na₂SO₄ can be very corrosive also, Fig. 10, for materials such as reaction sintered SiC. However, the direct reactions of Na₂SO₄ and SiO₂



occur with free energy changes of $+110$ kJ/mol and $+135$ kJ/mol, respectively, and therefore are not thermodynamically favorable under equilibrium conditions [48]. While the direct reaction of Na₂SO₄ and SiC is highly favorable



with free energy change -1855 kJ/mol and -845 kJ/mol, respectively, the silica layer prevents this direct reaction [49]. Instead, two indirect reaction schemes by which Na₂SO₄ may corrode SiC are considered more probable. The first scheme involves reaction with carbon, either from the aggressive environment or from excess free carbon in the SiC material, to form basic Na₂O or Na₂S according to

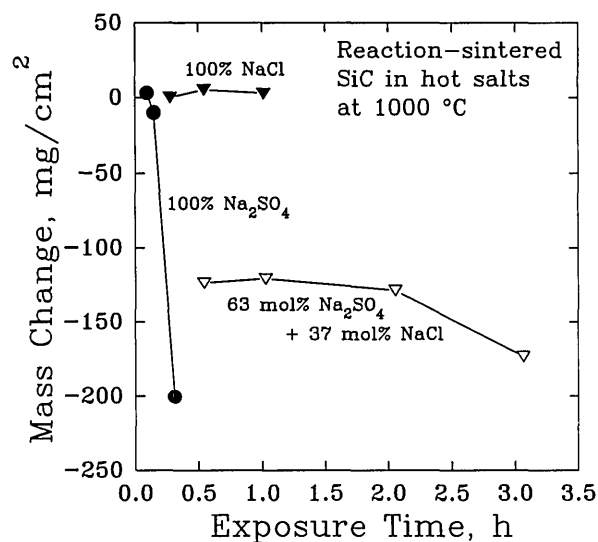
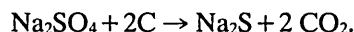
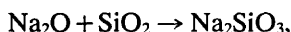


Fig. 10. The change in the mass of reaction-sintered silicon carbide exposed to various salts at 1000 °C. (After R. E. Tressler et al., J. Am. Ceram. Soc. 59 (5-6) 278-279 (1976).)

These compounds then attack the protective silica layer according to



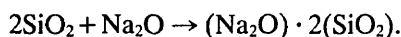
and, hence, lead to the active corrosion, Table 8, of the SiC material [50].

Table 8. Active corrosion of pressureless sintered SiC under the linear corrosion kinetics of a salt at 900 °C and 100 kPa (1 atm) of gas^a

Gas	Salt	Corrosion rate ($\text{mg} \cdot \text{cm}^{-2} \cdot \text{h}^{-1}$)
Air	Na ₂ SO ₄	-17
Air	Na ₂ SO ₄ · 5% C	-29
Air	Na ₂ SO ₄ · 10% C	-28
Air	Na ₂ SO ₄ · 1% NaNO ₃	-34
Air	Na ₂ SO ₄ · 1% Na ₂ O	-37
Air	Na ₂ SO ₄ · 1% Na ₂ S	-35
Air	Na ₂ SO ₄ · 1% Na ₂ CO ₃	-34
Air	Na ₂ SO ₄ · 5% Na ₂ CO ₃	-39
O ₂	Na ₂ SO ₄ · 1% Na ₂ CO ₃	-18
O ₂	Na ₂ SO ₄ · 2% Na ₂ CO ₃	-16
O ₂	Na ₂ SO ₄ · 10% Na ₂ CO ₃	-17
O ₂	Na ₂ CO ₃	-45

^a After D. W. McKee et al., *J. Am. Ceram. Soc.* **59** (9-10), 441-444 (1976).

In the second scheme, liquid Na₂SO₄ dissociates into solid Na₂O and gaseous SO₃, and the Na₂O subsequently interacts with the silica to form a liquid sodium silicate [51]:



It is also possible for a hybrid of these two schemes to occur to form a self-sustaining fluxing mechanism when the hot gaseous environment contains a small partial pressure of SO₃. In this case, the Na₂SO₄ reacts with the free carbon in the substrate to produce Na₂O or Na₂S which subsequently reacts with the silica layer to form Na₂SiO₃. The latter product may subsequently react with the SO₃ from the atmosphere to produce Na₂SO₄.



In each scheme, the corrosive pitting of the SiC material results in a degradation of the flexural

strength, Table 9, of the material to an extent that depends, Fig. 11, on the severity of the pitting [52].

Table 9. Four-point bend strength (± 1 standard deviation) of α -SiC (Hexoloy) after exposure to a salt corrodent at 1000 °C for 48 h^a

Gas	Salt	Average strength (MPa)
Air	None	409 \pm 62
Air	Na ₂ SO ₄	251 \pm 45
SO ₃	Na ₂ SO ₄	207 \pm 72
CO ₂	Na ₂ CO ₃	355 \pm 70

^a After J. L. Smialek et al., *J. Am. Ceram. Soc.* **69** (10), 741-752 (1986).

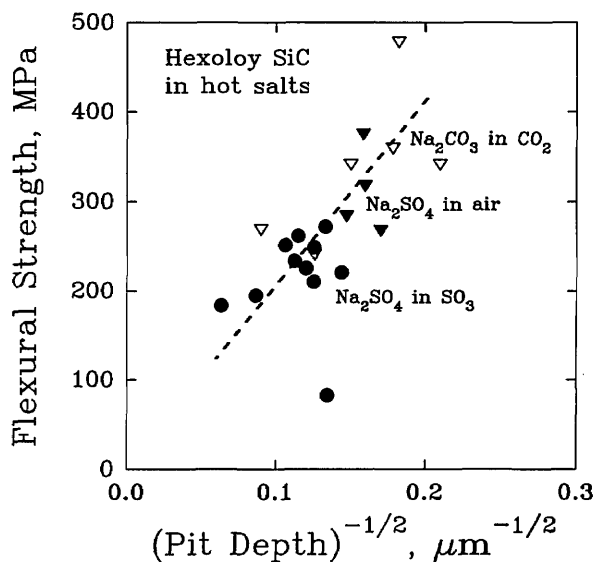
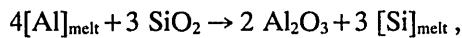


Fig. 11. The correlation of flexural strength with the corrosion pit depth for a commercial silicon carbide material exposed to various hot salts. (After J. L. Smialek et al., *J. Am. Ceram. Soc.* **69** (10), 741-752 (1986).)

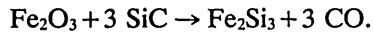
2.4 SiC in Molten Metals

Corrosion of ceramics by molten metals is not as well described in the literature as corrosion in other environments, although corrosion by molten metals is a concern in the design of heat exchangers for use in aluminum remelt industries, steel reheating furnaces and soaking pits, and other flue gas environments containing metallic species. The primary ceramic being considered for these applications is SiC because of its high thermal conductivity and thermal shock resistance and its potential resistance to corrosion by the molten metals.

The metallic species in the melt principally attack the oxide layer in reactions such as [53]



thereby exposing the SiC to direct corrosion by gaseous halide or other species in the combustion environment and possibly by metal-containing compounds as in the reaction [54]



Sintered SiC, recrystallized SiC, and siliconized SiC were found to have active corrosion rates, Tables 10 and 11, in aluminum remelt and steel soaking pit furnaces, while passive deposits were formed in a steel forge furnace. The mechanical strengths, Table 12, were generally degraded as a result of the increased surface flaws [55].

Table 10. Surface recession rates for commercial SiC materials exposed to industrial furnace environments. A number greater than zero indicates that a deposit grew on the surface^a

Furnace environment	Maximum temperature (°C)	Recession rate (mm/yr)		
		Hexoloy SA	NC400	NC430
Aluminum remelt No. 1	1040	-0.28	-0.14	-0.42
Aluminum remelt No. 2	1150		-3.78	-1.89
Steel soaking pit No. 1	925	-0.05	-0.03	-0.17
Steel soaking pit No. 2	1250	-3.53		-4.32
Steel reheat	1100	-0.05		-0.69
Forge	1175	+0.05	+0.31	-0.13

^a After J. I. Federer et al., *Adv. Ceram.* **14**, 315–334 (1985).

Table 11. Surface recession rates for various SiC materials exposed to industrial furnace environments^a

Furnace environment	Temperature range (°C)	Recession rate (mm/yr)			
		Hexoloy SA	CS101	CS101K	Hot pressed
Aluminum remelt No. 1	750–1250	-2.8	-7.15	-7.00	-7.00
Aluminum remelt No. 2	750–1200		-2.07	-1.94	-1.12
Steel soaking pit	1150–1175	-0.4	-0.90	-0.15	-0.15

^a After J. I. Federer, *Ceram. Trans.* **10**, 425–443 (1989).

Table 12. Room temperature fracture strength of Hexoloy SA determined by c-ring tests after exposure to industrial furnace environments

Furnace environment	Number of samples	Average strength (MPa)
^a Air	18	280 ± 50
^a Aluminum remelt	12	243 ± 23
^b Aluminum remelt No. 1	12	213 ± 39
^b Steel soaking pit	11	246 ± 56
^b Steel reheat	12	221 ± 34
^b Forge	9	286 ± 43

^a After J. Luyten et al., *High Temperature Corrosion of Technical Ceramics* (1900) pp. 161–168.

^b After J. I. Federer et al., *Adv. Ceram.* **14**, 315–334 (1985).

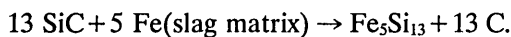
2.5 SiC in Complex Environments

Heat exchangers in coal combustion or coal gasification environments may be exposed to a combination of hot gases, Table 13, and molten slags, Table 14, simultaneously. Such complex environments increase the number of reaction paths that may be involved in the degradation of the protective silica layer and the active corrosion of the substrate. As should be expected, the experimental results produced in such environments are difficult to interpret precisely and may result in apparent contradictions. For example, compared to silicon carbide, alumina has been found to be both less resistant [56] and more resistant [57] to corrosion in slags nominally characterized as acidic.¹ The significance of this apparent contradiction is not that the results differ, but that a more precise characterization of the environment and the materials is needed along with consideration of the possible transport phenomena, such as fluxing, that can affect the overall nature of the corrosive process. In general, it can be noted that the corrosion of structural ceramics in complex environments tends to result in a net loss of material, Table 15, and the extent of the loss varies with the relative amount of basic and acidic components in the slag [58,59]. Acidic slags typically produce recession rates on the order of 1 mm/yr for silicon carbide at high temperature, while the recession rates from basic slags are on the order of 10–100 mm/yr.

¹ Acidic components are taken as SiO₂, Al₂O₃, and TiO₂, while basic components are Fe₂O₃, CaO, MgO, Na₂O, and K₂O.

Part of the dependence on the acidity or basicity of the slag may result from the order of magnitude difference in the viscosities of these slags at high operating temperature. The viscosity of an acidic slag is estimated to be approximately 60 Pa · s (600 poise), while being only 5 Pa · s (50 poise) for a basic slag [60]. The lower viscosity of the basic slag should be more conducive to the diffusion of the reactant and product species and thus to a more extensive material loss.

Specific chemical contributions to the differences between acidic and basic slags are thought to result from the greater presence of iron and calcium compounds in the basic slags. CaO may interact with the silica layer to form calcium silicate compounds, thereby reducing the effectiveness of the silica layer [61]. Localized, active corrosion of the SiC may occur when the iron compounds react directly with the SiC substrate to form iron silicides with an effective reaction of the form [62]:



This localized corrosion mechanism is thought to be important particularly for a slag thickness of 100 μm or greater and a temperature of 1250 °C or higher. Under these conditions, bubble formations from the evolution of gaseous SiO and CO may disrupt the silica layer, thereby providing the means for a direct reaction between the slag and the substrate.

Corrosion affects the lifetime of a material under in-service conditions not only through the loss of material, but also through the variation of the strength of the material. Corrosion increases the population of surface flaws which degrades the strength of the material and reduces its lifetime by increasing the probability of fracture under a mechanical or thermally induced stress. The strengths of SiC materials at elevated temperature were measured by C-ring tests, Table 16 [63], and four-point bend tests, Table 17 [64], after exposing the

materials to coal slags at various temperatures for various amounts of time. From these results, it may be readily inferred that the degradation of the strength of the material due to a temperature rise is compounded by oxidation, and both of these effects are significantly compounded by reaction with the slag. It is also significant that corrosion pits were cited as the primary failure sites of the exposed samples in both the C-ring tests and the four-point bend tests.

Table 13. Simulated gas composition for a medium-energy coal gasification environment^a

Gas:	H ₂	CO	CO ₂	N ₂	H ₂ S	H ₂ O
Vol. %	30	44	10	1.4	0.6	14

^a After T. E. Easler et al., in *High Temperature Corrosion in Energy Systems* (1985) pp. 269–280.

Table 14. Composition (percent by weight) of various coal slags

Component	Slag 1 ^a	Slag 2 ^b	Slag 3 ^c	Slag 4 ^c	Slag 5 ^d	Slag 6 ^d
SiO ₂	45.77	50.80	50	30	54	56
Fe ₂ O ₃	10.72	16.28	25	15	21	4
Al ₂ O ₃	14.17	23.93	20	10	19	31
CaO	18.75	2.72	5	25	0.1	0.5
MgO	7.08	0.72		20	0.9	0.8
NiO	0.01					
SO ₃	0.055	1.65				
P ₂ O ₅	0.51	0.27				
Na ₂ O	1.10	0.47			0.6	2.5
K ₂ O	0.52	1.60			1.7	2.6
TiO ₂	0.27	0.62			1.3	0.8
SrO + BaO	0.16					
V ₂ O ₅	0.03					
Base/Acid	0.63	0.29	0.43	1.5	0.33	0.12

^a After M. K. Ferber et al., *J. Am. Ceram. Soc.* **68** (4), 191–197 (1985).

^b After M. K. Ferber et al., *Ceram. Bull.* **62** (2), 236–243 (1983).

^c After T. E. Easler et al., in *High Temperature Corrosion in Energy Systems* (1985) pp. 269–280.

^d After P. F. Becher, *J. Matls. Sci.* **19**, 2805–2814 (1984).

Table 15. Corrosion rates for various commercial grades of SiC exposed to various environments for 200 h at 1250 °C. (See Table 14 for slag compositions)^a

Material	Condition	No slag (air)	Acidic slag (Slag 3)	Basic slag (Slag 4)
		($\mu\text{g} \cdot \text{cm}^{-2} \cdot \text{h}^{-1}$)	($\mu\text{g} \cdot \text{cm}^{-2} \cdot \text{h}^{-1}$)	($\mu\text{g} \cdot \text{cm}^{-2} \cdot \text{h}^{-1}$)
Hexoloy SA	Slip-cast	+0.7	–174	–657
Hexoloy SA	Extruded	–0.4	–50	–412
NC430	Slip-cast	+1.6	–117	–412
NC430	Extruded	+5.7	–50	–136

^a After T. E. Easler et al., in *High Temperature Corrosion in Energy Systems* (1985) pp. 269–280.

Table 16. High-temperature c-ring fracture strength of Hexoloy SA SiC after exposure to various environments. (See Table 14 for the slag composition.)^a

Environment	Temperature (°C)	Exposure time (h)	Fracture strength (MPa)
Air	1200	0	397 ± 7.6
Air	1200	24	375 ± 6.6
Air	1300	0	354 ± 8.9
Air	1300	24	361 ± 9.3
Slag 1	1200	24	335 ± 9.3
Slag 1	1300	24	285 ± 3.6

^a After M. K. Ferber et al., *J. Am. Ceram. Soc.* **68** (4), 191–197 (1985).

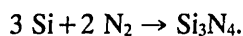
Table 17. Four-point flexural strengths of silicon carbide materials after exposure to various environments. Materials were exposed to the slag for 1150 °C for 350 h. (See Table 14 for the composition of the slag.)^a

Material	Environment	Temperature	Flexural strength (MPa)
NC203	Air	22	707
NC203	Air	1000	621
NC203	Air	1200	550
NC203	Air	1300	493
NC203	Slag 6	22	386
NC203	Slag 6	1000	414
NC203	Slag 6	1150	429
NC203	Slag 6	1300	371
Hexoloy SA	Air	22	407
Hexoloy SA	Air	1000	464
Hexoloy SA	Air	1300	471
Hexoloy SA	Slag 6	22	286
Hexoloy SA	Slag 6	1150	343
Hexoloy SA	Slag 6	1300	429
KT	Air	22	200
KT	Slag 6	22	186
KT	Slag 6	1150	221
KT	Slag 6	1300	214

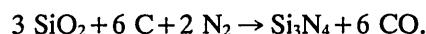
^a After P. F. Becher, *J. Matls. Sci.* **19**, 2805–2814 (1984).

3. Si₃N₄

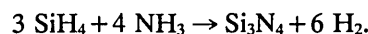
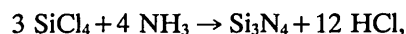
Silicon nitride exists in two crystallographic phases, denoted α -Si₃N₄ and β -Si₃N₄ [65]. The α -Si₃N₄ phase transforms to the β -Si₃N₄ form at approximately 1500 °C. Silicon nitride powders may be prepared by several different methods. The direct nitridation of silicon powder produces silicon nitride by the reaction



The carbothermic reduction of silica may also be used according to



Amorphous silicon nitride with very fine particle sizes can be produced by vapor phase methods using reactions such as



Silicon nitride powders can be processed by a variety of methods to produce bulk materials for structural applications. Common methods include hot pressing, sintering, hot isostatic pressing, and sintering of reaction-bonded compacts [66]. Sintering aids such as MgO and Y₂O₃ are usually used with all of the methods to produce high density products. In hot pressing, uniaxial stresses on the order of 15–30 MPa may be applied to the powder for several hours at temperatures in the range 1650 to 1850 °C. Pressureless sintering, in contrast, is conducted in a nitrogen atmosphere of approximately 0.1 MPa in the temperature range 1600 to 1800 °C. In both cases, boron nitride may be used for various purposes in containing or manipulating the product material with the result that the surface of the product may have a small boron nitride contamination. The final product is generally a polycrystalline material consisting primarily of elongated, fiber-like, β -Si₃N₄ grains and a secondary, intergranular phase that may be either glassy MgO or crystalline Y₂O₃. When MgO is used as an additive in quantities greater than 5 wt. %, crystalline Mg₂SiO₄ may also be present. For reaction-bonded silicon nitride fired in a lower temperature range, 1150 to 1400 °C, the final product may consist predominantly of α -Si₃N₄ grains with a lower bulk density and a significantly larger porosity, on the order of 10%–30%.

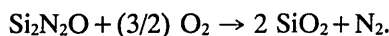
3.1 Oxidation of Si₃N₄

The oxidation of silicon nitride is a complex process that depends significantly on the sintering aids and the impurities in the material [67]. The primary protective scale is silica which may be formed directly from the reaction of silicon nitride and oxygen:

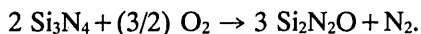


This reaction may be most significant during the initial oxidation of the substrate. Subsequently, multistep reaction sequences may be more important.

In the case of chemical vapor deposited (CVD) silicon nitride without sintering aids [68], the formation of a duplex oxide scale has been reported. The scale was found to consist of an outer layer of silica and an inner layer of silicon oxynitride. The oxidation process in this case could be described by two reaction steps. First, oxygen diffused through the silica layer to the silicon oxynitride layer where part of the oxygen reacted to form additional silica according to:



The unreacted oxygen continued to diffuse to the substrate material where additional silicon oxynitride was formed:



Diffusion through the silicon oxynitride layer was identified as the rate-controlling process because the molecular oxygen diffusivity, Table 18, was significantly smaller for $\text{Si}_2\text{N}_2\text{O}$ than for SiO_2 . The overall oxidation process, though, followed parabolic kinetics,

$$x^2 = 2 k_p t,$$

in which the square of the scale thickness is proportional to the time of exposure, with a parabolic rate constant, k_p , of $66 \text{ nm}^2/\text{min}$.

Table 18. Molecular oxygen diffusivities of silica and silicon oxynitride^a

Material	Temperature (°C)	Diffusivity ($10^{-8} \text{ cm}^2/\text{s}$)
SiO_2	1100	1.42
SiO_2	1200	2.78
SiO_2	1300	5.00
SiO_2	1400	8.37
$\text{Si}_2\text{N}_2\text{O}$	1200	0.00240
$\text{Si}_2\text{N}_2\text{O}$	1300	0.00927
$\text{Si}_2\text{N}_2\text{O}$	1400	0.110

^a After R. E. Tressler et al., in *High Temperature Corrosion of Technical Ceramics* (1990), pp. 69–89.

When sintering aids or impurities have been present, the composition of the scale has been

found to be more complex. For hot-pressed Si_3N_4 containing MgO and CaO as additives, the scale consisted of glassy SiO_2 , in which crystalline α -cristobalite also formed, plus magnesium silicates and magnesium-calcium silicates [69]. A similar study analyzed the composition of the scale, Table 19, and found that MgSiO_3 could be clearly identified as a principal component of the scale [70]. Other compounds, while evidently present, could not be identified conclusively. The oxidation kinetics relation was parabolic, Fig. 12, as has been found to be common for most MgO-containing silicon nitrides [71], with an activation energy of approximately 440 kJ/mol [72].

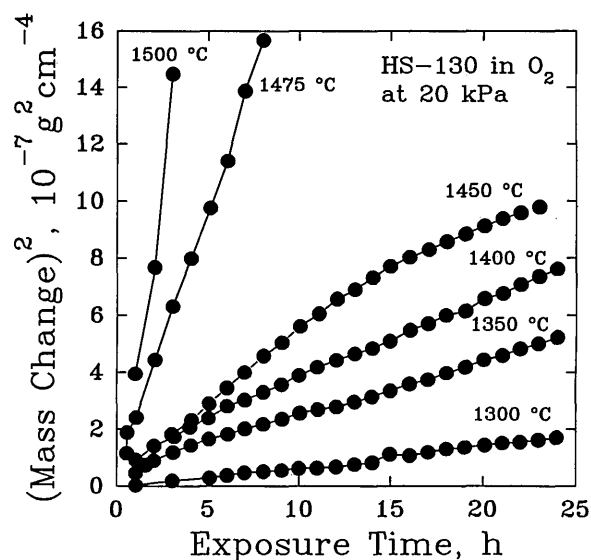


Fig. 12. The oxidation of a commercial silicon nitride material in dry oxygen showing parabolic oxidation kinetics. (After W. C. Trip et al., *J. Am. Ceram. Soc.* 59 (9–10), 399–403 (1976).)

The oxide scale formed on sintered silicon nitride containing yttria as a major sintering aid has been found to differ both substantially and morphologically from the scale on Si_3N_4 prepared either by hot pressing with MgO or by the CVD technique [73]. The scale itself was found to be a layered structure in which each layer had an outer region of crystalline silica, an intermediate glassy region, and an inner thin layer of $\text{Y}_2\text{Si}_2\text{O}_7$. The glassy region was porous, often containing large bubble formations that most likely resulted from the evolution of N_2 gas during oxynitride formation. Thin layers of $\text{Y}_2\text{Si}_2\text{O}_7$ were also found at the interface between the substrate and the scale, and at the outer surface of the scale.

Table 19. Composition of the oxide scale formed on hot-pressed HS-130^a

Temperature (°C)	Exposure time (h)	O ₂ Pressure (kPa)	Si (wt%)	Mg (wt%)	O (wt%)
1300	24	80	27.4±2	17.37±2.8	55.2
1350	194	20	28.1±0.8	16.8±0.5	55.12
1400	24	10	28.0±0.3	23.15±0.8	48.89
1400	24	20	29.0±3.5	22.0±4.0	49.0
1400	24	40	27.9±0.5	21.61±0.8	50.53
1400	24	80	27.9±0.5	21.96±0.5	50.15
1450	21	20	30.0±0.6	26.68±1.5	46.26
1475	24	20	28.6±0.5	21.9±1.5	49.49
1500	24	20	39	10	51

^a After W. C. Tripp et al., *J. Am. Ceram. Soc.* **59** (9–10), 399–403 (1976).

It was suggested that the morphology of the scale had a direct effect on the apparent oxidation kinetics of the material. Initially, the scale growth was logarithmic rather than parabolic, such that

$$x = k_1 + k_2 \ln(t),$$

for constants k_1 and k_2 . It was reasoned that such a relation would be appropriate if the effective cross section through which diffusion could occur diminished with time, as might have occurred when gas bubbles grew in the scale. Subsequently, when a sufficient cristobalite layer had formed, the slow diffusion rate through that layer would be rate-controlling, and the kinetic relation would become parabolic. A behavior consistent with this scheme was also observed in a study using silicon nitride sintered with Y₂O₃ and Fe₂O₃ [74]. In that work, the kinetics relation was described as being asymptotically parabolic with an apparent activation energy of 470 kJ/mol.

At sufficiently low oxygen partial pressure, the passive oxidation of silicon nitride may change to active oxidation [75]. The temperature at which this transition occurs for a given oxygen pressure, Table 20, increases with increasing oxygen pressure [76].

The strength of both sintered and hot pressed silicon nitride materials have been found to decrease for oxidation times of one hour or longer [77]. A brief increase in strength was noted for very short oxidation times, approximately 30 min, which was thought to be due to the blunting of crack tips. For longer times, Table 21, the oxidation of the material

resulted in the generation of new flaws that caused the average strength to decrease. Oxidizing the two materials under static load, however, resulted in distinct behaviors. The sintered material had an increase in strength, while the hot-pressed material suffered a decrease in strength.

Table 20. Active-to-passive transition temperature, T_{ap} , for hot pressed HS-130 and sintered 6Y-14 silicon nitride at various values of the partial pressure of oxygen, $P(O_2)$.^a

Material	Flow rate (cm ³ /s)	$P(O_2)$ (Pa)	T_{ap} (°C)
HS-130	0.56	7.1	1366
HS-130	0.56	27.4	1436
HS-130	0.56	205.5	1520
6Y-14	0.56	7.0	1365
6Y-14	0.56	28.5	1446
6Y-14	0.56	111.0	1480

^a After W. L. Vaughn et al., *J. Am. Ceram. Soc.* **73** (6), 1540–1543 (1990).

Table 21. The room temperature Weibull parameters for sintered SNW-1000 and hot-pressed NCX-34 silicon nitride ceramics after oxidation at 1370 °C in air under various loads. σ_0 = Weibull characteristic strength, m = Weibull modulus, and R^2 = correlation coefficient^a

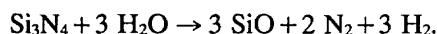
Material	Load during oxidation (MPa)	Oxidation time (h)	Number of samples	σ_0 (MPa)	m	R^2
SNW-1000	0	0	50	300	8.2	0.98
SNW-1000	0	0.5	10	325	7.7	0.97
SNW-1000	0	1	53	290	10.9	0.94
SNW-1000	0	12	11	275	17.2	0.97
SNW-1000	0	20	11	215	8.3	0.90
SNW-1000	0	50	10	225	19.6	0.98
SNW-1000	23	1	15	390	10.2	0.99
SNW-1000	45	1	15	295	7.0	0.97
NCX-34	0	0.5	10	555	7.0	0.96
NCX-34	0	1	54	575	14.1	0.96
NCX-34	0	12	11	400	7.0	0.92
NCX-34	0	20	12	500	14.3	0.96
NCX-34	0	50	12	435	7.6	0.94
NCX-34	45	1	14	490	9.7	0.93
NCX-34	158	1	13	385	7.9	0.93

^aAfter T. E. Easler et al., *J. Am. Ceram. Soc.* **65** (6), 317–320 (1982).

3.2 Si₃N₄ in Hot Gases

The passive oxidation of hot-pressed silicon nitride has been found to be enhanced by water vapor in oxygen atmospheres [78], with the parabolic rate constant, Table 22, being larger than for dry oxygen. The activation energy for oxidation was 488 ± 30 kJ/mol in wet oxygen and 375 ± 25 kJ/mol in dry oxygen.

The presence of gaseous H₂O in H₂ gaseous environments has been found to cause an active oxidation of Si₃N₄ according to [79]:



Under these conditions, the average flexural strength of the material, Table 23, decreased. When the partial pressure of H₂O was greater than about 10 Pa, a protective silicate layer may have formed as a result of a reaction between the gaseous reaction product, SiO, and the sintering aid, Y₂O₃. Concurrently, the flexural strength of the material increased.

Table 22. Parabolic rate parameter, K_p , for the oxidation of hot-pressed HS-130 silicon nitride in O₂ with a partial pressure of water vapor of 3.3 kPa (0.033 atm)^a

Temperature (°C)	log K_p (g ² · cm ⁻⁴ · s ⁻¹)
1200	-12.6
1260	-12.0
1315	-11.3
1370	-10.8

^a After S. C. Singhal, *J. Am. Ceram. Soc.* **59** (1-2) 81–82 (1976).

Table 23. Room-temperature flexural strength, σ , of hot isostatically pressed AY6 silicon nitride after exposure at 1400 °C for 10 h in H₂ atmospheres with various partial pressures $P(\text{H}_2\text{O})$ of water vapor^a

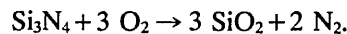
$P(\text{H}_2\text{O})$ (Pa)	σ (MPa)
0.26	580 ± 35
0.45	525 ± 60
3.6	515 ± 30
20	460 ± 40
100	690 ± 60
520	800 ± 80

^a After H. Kim et al., *Ceramic Transactions* **10**, 81–96 (1989).

3.3 Si₃N₄ in Molten Salts

The corrosion of silicon nitride by molten salts has been found to occur in three stages. For sodium carbonate on reaction-bonded Si₃N₄, the first stage is a very brief process, lasting only minutes, during which sodium silicate is formed. The second stage follows diffusion-limited parabolic reaction kinetics resulting from the inward diffusion of molecular oxygen to the silicon nitride surface where the subsequent reaction forms silica. The silica material, though, partially dissolves into the silicate glass until a saturation limit is reached. Thereafter, oxidation produces a growing silica layer. Oxygen diffusion through this layer is very slow, and becomes the rate limiting step for the third stage of the corrosion process [80].

A similar study on hot isostatically pressed reaction-bonded Si₃N₄ obtained very similar results [81]. The brief first stage was found to be a period of weight loss controlled by two reactions. In the first, gaseous oxygen reacted with the silicon nitride to form a solid silica layer according to:

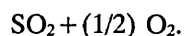
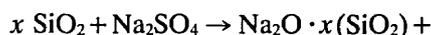
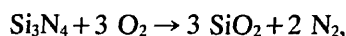


Subsequently, the silica dissolved in the molten salt layer to form a liquid sodium silicate:



The first stage process was completed after approximately 5 min after which weight gain occurred primarily due to the formation of silica.

Corrosion of silicon nitride by sodium sulfate was found to have a similar corrosion process consisting, however, of only two stages, an initial lengthy period of slow weight loss followed by a process of slow weight gain. The weight loss appeared to be mostly the result of the vaporization of the Na₂SO₄. The primary reaction sequence for corrosion was a coupled oxidation-dissolution process such that:



Silica formation and dissolution proceeded with the silica layer growing at a rate that was faster than what was expected for normal oxidation. Eventually, the silica layer became sufficiently thick that

further oxidation of the silicon nitride substrate was limited by the slow diffusion of oxygen through the silica layer.

3.4 Si₃N₄ in Molten Metals

Hot pressed silicon nitride materials, with either Y₂O₃ or MgO as sintering aids, have been exposed to the flue gas of an aluminum remelting furnace in which the flue gas consisted mainly of CO₂, CO, O₂, and H₂O, plus small amounts of Cl, F, SO₂, SO₃, NO, and NO₂. After exposure, the silicon nitride specimens were found to be coated with a vitreous deposit in which β-Si₃N₄, Si, and Al₂O₃ were found [83]. The Si₃N₄ material apparently diffused or dissolved from the substrate and was absorbed into the deposit, while the Si and Al₂O₃ were derived from the aluminum melt. The deposit also showed evidence of trapped gas bubbles, and some depletion of the sintering aid components was found in the surface region of the substrate material adjacent to the vitreous deposit. The latter result indicated that it was primarily the intergranular phases that were corroded. Specimens with MgO as the sintering aid appeared to be less resistant to corrosion than specimens with Y₂O₃ as the sintering aid, as was reflected in the variations of the flexural strengths of the materials, Table 24. While both materials had significantly reduced flexural strengths, the residual strength of Si₃N₄(Y₂O₃) was nearly twice that of Si₃N₄(MgO).

Table 24. Four-point bend strengths of hot-pressed silicon nitride materials after exposure to an aluminum remelting furnace^a

Sintering Aid	Exposure time (h)	Number of samples	Average strength (MPa)
Y ₂ O ₃	0	20	610 ± 39
Y ₂ O ₃	100	8	437 ± 62
MgO	0	10	610 ± 54
MgO	100	8	282 ± 38

^a After J. Luyten et al., *High Temperature Corrosion of Technical Ceramics* (1990) pp. 161–168 (1990).

3.5 Si₃N₄ in Complex Environments

An extensive penetration of coal slag into hot pressed NCX-34 silicon nitride was found as a result of corrosion in simulated coal combustion environments (slags 5 and 6 in Table 14) [84]. This material had WC and β-Y₅Si₃O₁₂N as minor phases in the material. It was noted that the oxidation of

Y₅Si₃O₁₂N to form Y₂SiO₅, cristobalite SiO₂, or RY₅Si₆O₂, where R may be H, Na, Mn, Fe, Al, Th, or Zr, would occur with a large increase in molar volume. The resulting tensile stress could cause microcracking and thus would promote slag penetration and the formation of subsurface pits. These microcracks and pits were cited as being responsible for the strength degradation, Table 25, observed in these environments. When the corroded layer of the surface was removed by diamond grinding, the strength of the material returned to approximately 95% of its original, as-received value. Thus the strength-reducing defects were limited to the surface of the specimens and did not involve internal compositional changes in the substrate.

Table 25. Room-temperature four-point flexural strengths of silicon nitride materials after exposure to various environments. (See Table 14 for the composition of the slag.)^a

Material	Environment	Temperature (°C)	Exposure time (h)	Flexural strength (MPa)
NC-132	Air	22	0	850
NC-132	Slag 5	1220	500	325
NC-132	Slag 6	1150	350	430
NCX-34	Air	22	0	810
NCX-34	Slag 5	1220	500	300
NCX-34	Slag 6	1150	350	325

^a After P. F. Becher, *J. Matls. Sci.* **19**, 2805–2814 (1984).

4. Coating Systems

The primary corrosion resistance of both silicon carbide and silicon nitride results from the oxide layer formed on the surface of the material. It is reasonable, therefore, to consider the possibility of enhancing the corrosion resistance of these materials by modifying their surfaces with specially prepared oxide coatings. For such coatings, there would be chemical, thermal, and mechanical requirements beyond the need to resist corrosion by combustion gases, slag, and ash. The coating and substrate materials would need to be well bonded but otherwise would have a low rate of subsequent reaction, and their coefficients of thermal expansion would need to be compatible to prevent thermally induced stresses and subsequent cracking. The coating also would need to have adequate toughness and thermal shock resistance, as well as a sufficiently high thermal conductivity, so that the performance of the system would not be affected adversely.

Initial insight into the selection of candidate coating materials may be derived from a consideration of the phase equilibria relations between the slag and ash constituents and the candidate oxide coatings. For slagging conditions in particular, the major slag constituents are silica, alumina, and iron oxide; hence, coatings of these same oxides would be expected to be dissolved by the slag. Other slag constituents such as alkali and rare earth oxides could also react with these coatings to produce lower melting point compositions which would degrade the performance of the coatings. Consequently, silica, alumina, and iron oxide would not be expected to be well suited as protective coatings in these coal-fueled applications.

Little work appears to have been reported on the use of ceramic coatings on ceramics. However, preliminary indications of the potential for such coatings may be gained from current studies of refractory oxide coatings and from ceramic coatings on metal alloys in turbine engines.

Refractory oxide coatings have been used successfully in the radiant heater sections of pulverized coal-fueled boilers to protect low-alloy water walls. In these slagging applications, a layer of solidified slag underlies the molten deposit and limits the solution of the refractory coating into the slag deposit. General summaries of research on the behavior of refractory oxides in coal gasification systems indicate that alumina refractories [85] might be suitable for use in dry ash systems to 1100 °C and that magnesia-chromia refractories [86] might be useful in slagging systems at temperatures of 1500 °C. However, it should be noted that these applications exhibit lower oxygen partial pressures and higher water partial pressures than would be expected in combustion systems, and the refractories examined in these studies were in brick or castable forms with significant amounts of other phases present.

There is a significant body of research on the stability of oxide-forming elements in alloys in coal gasification and combustion applications. Much of this research has been conducted with a focus on the propensity for sulfidation [87]. The results have clarified the regimes of oxygen, sulfur [88], and chlorine [89] partial pressures in which protective oxides are stable and have helped to understand alloy corrosion mechanisms [90].

Table 26 shows the lower partial pressure limits of stability for several oxides in oxygen and sulfur. The values shown in the table are many orders of magnitude lower than any value that might be expected to be encountered in combustion systems.

As a result, none of these oxides would have an intrinsic problem in terms of stability.

Table 26. The partial pressures of oxygen, P_{O_2} , above which selected oxides are stable. The concurrent partial pressure of sulfur, P_S , is also shown^a

Oxide	$T = 1150 \text{ K (877 } ^\circ\text{C)}$		$T = 1450 \text{ K (1177 } ^\circ\text{C)}$	
	$\log_{10}(P_{O_2})$ (P in Pa)	$\log_{10}(P_S)$ (P in Pa)	$\log_{10}(P_{O_2})$ (P in Pa)	$\log_{10}(P_S)$ (P in Pa)
SiO ₂	-27	0	-18	2
Al ₂ O ₃	-34	13	-24	-8
ZrO ₂	-35	-17	-25	-11
Ce ₂ O ₃	-40	-31	-28	-21
Cr ₂ O ₃	-20	-7	-13	-3
MgO	-39	-23	-26	-15

^a After E. A. Gulbranson and G. H. Meier, DOE/FE/13547-01, UC-90h (May 1980).

Among the materials listed in Table 26, the relatively high coefficient of thermal expansion of zirconia has encouraged its use as a thermal barrier coating on metallic gas turbine components. This application has required investigation of the corrosion of zirconia-based coatings in combustion environments. Typically, low velocity burner rig tests have been conducted on compositionally graded coatings [91]. In these experiments, corrosive alkali sulfates and sulfates with vanadium were deposited on zirconia containing 8% yttria as a stabilizing oxide. No significant reaction of zirconia with sodium sulfate was noted. However, the addition of vanadium and magnesium, at the level of 50 parts per million, was shown to foster corrosive reactions and the destabilization of the zirconia. Significantly, the porosity of the coating also was shown to foster coating failures due to the penetration of liquid sodium sulfate into the coating [92]. Under thermal cycling, the liquid sodium sulfate was thought to have frozen and expanded, thereby mechanically opening cracks in the coating. Failure in these experiments, Table 27, was determined as the onset of cracking or spallation. Coating lifetimes greater than 500 h were reported.

Concern over the role of vanadium in the deterioration of stabilized zirconia coatings has resulted in research on the reactivity of indium oxide, scandium oxide, yttria, and magnesia stabilizers. Thermogravimetric analyses of these oxides in molten sodium vanadate equilibrated in an SO₃ environment has shown indium oxide and scandium oxide to be more resistant to attack than the conventional stabilizers, yttria and magnesia [93].

Table 27. Burner rig corrosion test results of thermal barrier coatings^a

Coating	Intermediate layer	Overcoat	Time to failure (h)
PS ZrO ₂	NiCrAlY Bond Coat	Pt	242
PS ZrO ₂	NiCrAlY Bond Coat	AlPt	> 500
PS ZrO ₂	NiCrAlY Bond Coat + ZrO ₂ /NiCrAlY	Pt	> 500
PS ZrO ₂	NiCrAlY Bond Coat + ZrO ₂ /NiCrAlY	AlPt	500
PVD ZrO ₂	none	none	22–70

^a C. A. Anderson et al., NASA Report CR-65919 (February, 1982).

Notes:

PS = Plasma spray

Bond Coat = 127 μm thick

ZrO₂ = 380 μm thick

PVD = Electron Beam Physical Vapor Deposition

ZrO₂/NiCrAlY = 50 vol% ZrO₂-8Y₂O₃ + 50 vol% NiCrAlY

Pt: 31 μm thick sputter deposited

AlPt: 14 μm thick sputter deposited

Test Conditions:

Fuel: No. 2 Distillate with:

Element	Na	Mg	Cl	K	Ca	S
Amount (ppm)	100	10	180	3	4	2

Nominal gas temperature = 1204 °C

Maximum metal temperature = 843 °C

Test duration = 500 h

Cycle = 55 min. heating + 5 min. air cooling

Finally, attempts are being made to improve the compatibility of ceramic coatings and metal substrates. The effort is specifically designed to reduce the thermal stresses caused by the different amounts of thermal expansion experienced by metals and ceramics. The approach being taken is to use intermediate layers of materials to provide a gradual transition in the coefficient of thermal expansion across the interface region [94]. For metallic substrates, the intermediate layers typically have consisted of mixed ceramic and metallic compositions which unfortunately provides an opportunity for corrosion to occur beneath the ceramic overlayer. At the present time, therefore, the use of ceramic coatings metallic interlayers does not appear to offer a significant advantage for coal-fueled applications.

5. Conclusion

Significant progress towards a comprehensive understanding of the oxidation of both silicon carbide

and silicon nitride has been made over the past several decades. Models have been advanced to account for the quantitative effects of competing chemical reactions, required mass transport mechanisms, and changes in surface and microstructural morphologies. In contrast, models describing the corrosion of these materials in complex environments are considerably more speculative. Few studies have been made to isolate the effects of specific components of either the complex atmosphere or the material. Most recent studies involving complex environments have been focused on the more immediate concerns of engineering design, viz., does the given material have adequate corrosion resistance for the given design objective? Important clues towards the development of better materials can be provided by such studies, particularly when analyses of the compositions of the starting materials and environments are given along with the compositions of the reaction products. However, the development of detailed models must rely on known results of specific interactions. Consequently, much of the understanding of corrosion in complex environments is based on detailed studies of oxidation or of corrosion in simplified environments.

The silica layer, for example, that develops at the surface of the SiC or Si₃N₄ substrate, is known to play a key, multifaceted role in the corrosion resistance of both materials. The frequently observed parabolic corrosion kinetics may be directly related to the diffusion of oxygen through an oxide layer, but there are numerous reaction sequences that can contribute to that result.

For silicon carbide, silica forms a protective barrier that prevents the direct reaction of the substrate with an attacking species. The diffusion of oxygen through the silica results in parabolic reaction kinetics. The oxide barrier, however, may be sacrificial in the sense that the silica itself may be dissolved in a molten deposit. Replenishment of the silica layer then depends on the diffusion of oxygen to the substrate where additional silica can be formed by the oxidation of the substrate. If the attacking deposit or the silica layer impedes the flow of oxygen to the substrate, such that the partial pressure of oxygen is very low, then the silica itself may react directly with the substrate causing both reactants to be diminished.

For silicon nitride, the oxidation of the substrate forms silicon oxynitride which subsequently oxidizes to form silica. In this case, parabolic reaction kinetics are still observed, but the layer of silicon oxynitride may control the oxygen diffusion rate.

The dominant reaction sequence at any time may be strongly influenced by the chemical species in the attacking atmosphere and by the impurities, sintering aids, grain boundary phases, and porosity of the substrate material, as well as the immediate reaction history. Impurities such as carbon, for example, may cause an acidic slag to behave more like a basic slag with respect to corrosion of silicon carbide. For silicon nitride, sintering aids such as MgO and CaO may add magnesium-calcium silicate components to the oxide layer and may influence the crystalline or glassy nature of the oxide. Additional quantitative studies are needed to investigate these effects in greater detail.

In the context of designing components for use in corrosive environments, there are two primary concerns regarding the selection of a material: the survival of the material, expressed as the recession rate of the surface, and the mechanical strength of the component. The corrosion rates for ceramics can be relatively small, and, as a result, the recession rates may be tolerable. Recession rates of SiC on the order of 1 mm/yr in acidic slag and 10–100 mm/yr in basic slags are possible. However, surface pitting and the overall increase in the surface flaw populations generally degrade the strength of the material and can reduce its average mechanical lifetime even when the recession rate is small. While some combinations of material and environment may produce a short-term strength enhancement resulting from the healing of surface defects, long-term corrosion generally tends to decrease the strength of the material as the severity of the surface pitting increases. An understanding of the interplay of the time-dependent chemical and mechanical effects and consequences has yet to be established.

There are several critical issues that have yet to be examined. Prominent among these issues is long-term corrosion. Most studies report short-term results that span only a few tens of hours, and results with exposure times on the order of 1000 h are scarce. Long-term data are particularly needed to study possible time-dependent phenomena such as break-away corrosion and the potential for lifetime-limiting effects such as environmentally enhanced creep phenomena.

Of equal importance is the need for systematic studies of corrosion in environments that are well characterized chemically and thermally. Studies conducted in industrial furnaces are valuable proof tests, but the results are often difficult to interpret because the precise composition of the environment is unknown and both the composition and the

temperature distribution may vary over the course of the study.

In conjunction with these tests, mechanical properties need to be measured in situ at elevated temperature. Secondary or grain boundary constituents, impurities, and reaction products can be liquids at the temperatures of interest. Measurements at room temperature do not properly reflect the consequences of these phases, nor do they account for environmentally assisted fracture effects.

Lastly, while it has been noted that the corrosion behavior of various types of silicon carbide and silicon nitride have been examined in many environments, little research has focused on the role of ceramic coatings in protecting silicon-based materials. It may be possible to enhance the corrosion resistance of silicon-based ceramics by the use specially designed oxide coatings. Coatings of either the overlay type, which may be applied by plasma spraying, or surface modified materials offer the potential to develop surface layers more resistant to reaction with alkali or slag deposits than native silica. Consideration of previous experience with coatings for refractory ceramics and metal alloys suggests that zirconia stabilized with indium oxide or scandium oxide might provide an effective coating for silicon-based ceramics. However, the extent of corrosion may depend on the specific slag and ash deposit compositions, and the degree of protection may depend significantly on the capacity of the coating to resist spallation and cracking. Measurements of the thermal and mechanical properties of such coatings, along with studies of potential problems associated with the porosity of the coating, would have to be made.

Acknowledgment

The authors thank the Pittsburgh Energy Technology Center for their support of this work under contract DE-AI22-92PC92179.

6. References

- [1] R. N. Katz, Opportunities and Prospects for the Application of Structural Ceramics, in *Structural Ceramics*, J. B. Wachtman, Jr., ed., Treatise on Materials Science and Technology, Vol. 29, Academic Press (1989) pp. 1–26.
- [2] C. Eckert and J. Weatherall, *Advanced Ceramics: '90s Global Business Outlook*, Ceram. Ind. 53–57 (April 1990).
- [3] Anonymous, *Ceramic Application and Design*, Ceram. Ind. S3–S18 (February 1988).
- [4] W. Bryzik and R. Kamo, *Adiabatic Engines: Worldwide Review*, SP-571, Society of Automotive Engineers, Inc. (1984).

- [5] O. Van der Biest, M. Van de Voorde, and R. A. McCauley, Ceramics for High Temperature Heat Exchangers, in High Temperature Equipment, A. E. Sheindlin, ed., Hemisphere Publishing Corporation (1986) pp. 323–352.
- [6] S. J. Dapkunas, Ceramic Heat Exchangers, *Ceram. Bull.* **67** (2), 388–391 (1988).
- [7] W. C. Shumay, Jr., Corrosion in Electronics, *Advanced Materials & Processes Inc., Metal Progr.* **132** (3), 73–77 (1987).
- [8] H. A. Huckins, Apply Advanced Ceramics More Widely in Chemical Processes, *Chem. Eng. Progr.* **87** (2), 57–60 (1991).
- [9] Anonymous, Slow Growth for Ceramics, *Adv. Mater. Processes* **1**, 29–44 (1989).
- [10] J. A. Pask, Structural Ceramics, *J. Mater. Eng.* **11** (4), 267–274 (1989).
- [11] L. M. Sheppard, Corrosion-Resistant Ceramics for Severe Environments, *Ceram. Bull.* **70** (7), 1146–1166 (1991).
- [12] R. G. Munro, E. F. Begley, and T. L. Baker, Strengths and Deficiencies in Published Advanced Ceramics Data, *Ceram. Bull.* **69** (9), 1498–1502 (1990).
- [13] G. Fisher, Ceramic Corrosion Fundamental to Process Efficiency Gains, *Ceram. Bull.* **64** (7), 975–978 (1985).
- [14] K. E. Spear, R. E. Tressler, Z. Zheng, and H. Du, Oxidation of Silicon Carbide Single Crystals and CVD Silicon Nitride, *Ceramic Transactions, Vol. 10, Corrosion and Corrosive Degradation of Ceramics*, R. E. Tressler, ed., American Ceramic Society, Inc. (1989) pp. 1–18.
- [15] M. Srinivasan, The Silicon Carbide Family of Structural Ceramics, in *Treatise on Materials Science and Technology, Volume 29, Structural Ceramics*, J. B. Wachtman, Jr., ed., Academic Press (1989) pp. 99–159.
- [16] P. T. B. Shaffer, Engineering Properties of Carbides, in *Engineered Materials Handbook, Ceramics and Glasses, Volume 4*, S. J. Schneider, Jr., ed., ASM International (1991) pp. 804–811.
- [17] R. Morrell, Handbook of Properties of Technical & Engineering Ceramics, Part 1, An Introduction for the Engineer and Designer, Her Majesty's Stationery Office (1985) pp. 45–54.
- [18] S. Yajima, Special Heat-Resistant Materials from Organometallic Polymers, *Am. Ceram. Soc. Bull.* **62** (8), 893–898 (1983).
- [19] S. Strepkoff, Method and Device for Manufacturing Silicon Carbide, U.S. Patent Number 3,755,541 (1979).
- [20] G. C. Wei, Beta SiC Powders Produced by Carbothermic Reduction of Silica in a High-Temperature Rotary Furnace, *J. Am. Ceram. Soc.* **66** (7), C-111–C-113 (1983).
- [21] E. G. Acheson, Production of Artificial, Crystalline Carbonaceous Material, U.S. Patent Number 492,767 (1893).
- [22] A. W. Evans, R. Wynne, and C. Marynowski, Preparation of Pigmentary Silicon Carbide, U.S. Patent Number 3,485,591 (1969).
- [23] J. D. Chase, Method of Making Sub-micron Particles of Metal Carbides of Enlarged and Controlled Particle Size, U.S. Patent Number 3,839,542 (1974).
- [24] A. C. Lea, Oxidation of Silicon Carbide Refractory Materials, *J. Soc. Glass Technol.* **33**, 27–50T (1949).
- [25] G. Ervin, Jr., Oxidation Behavior of Silicon Carbide, *J. Am. Ceram. Soc.* **44** (9), 347–352 (1958).
- [26] C. Wagner, Passivity During the Oxidation of Silicon at Elevated Temperatures, *J. Appl. Phys.* **29**, 1295–1297 (1958).
- [27] E. A. Gulbransen, K. F. Andrew, and F. A. Brassart, The Oxidation of Silicon Carbide at 1150 to 1400 °C and at 9×10^{-3} to 5×10^{-1} Torr Oxygen Pressure, *J. Electrochem. Soc.* **113** (12), 1311–1314 (1966).
- [28] W. L. Vaughn and H. G. Maahs, Active-to-Passive Transition in the Oxidation of Silicon Carbide and Silicon Nitride in Air, *J. Am. Ceram. Soc.* **73** (6), 1540–1543 (1990).
- [29] W. W. Pultz and W. Hertl, SiO₂+SiC Reaction at Elevated Temperatures, *Trans. Faraday Soc.* **62**, 2499–2504 (1966).
- [30] E. A. Gulbransen and S. A. Jansson, The High-Temperature Oxidation, Reduction, and Volatilization Reactions of Silicon and Silicon Carbide, *Oxidation Metals*, **4** (3), 181–201 (1972).
- [31] V. L. K. Lou and A. H. Heuer, Graphical Displays of the Thermodynamics of High-Temperature Gas-Solid Reactions and Their Applications in High Temperature Corrosion of Technical Ceramics, R. J. Fordham, ed. Elsevier Applied Science, New York (1990) pp. 33–52.
- [32] K. G. Nickel, The Role of Condensed Silicon Monoxide in the Active-to-Passive Oxidation Transition of Silicon Carbide, *J. European Ceram. Soc.* **9** (1), 3–8 (1992).
- [33] J. A. Costello and R. E. Tressler, Oxidation Kinetics of Hot-Pressed and Sintered α -SiC, *J. Am. Ceram. Soc.* **64** (6), 327–331 (1981).
- [34] T. Narushima, T. Goto, and T. Hirai, High-Temperature Passive Oxidation of Chemically Vapor Deposited Silicon Carbide, *J. Am. Ceram. Soc.* **72** (8), 1386–1390 (1989).
- [35] M. Maeda, K. Nakamura, and M. Yamada, Oxidation Resistance Evaluation of Silicon Carbide Ceramics with Various Additives, *J. Am. Ceram. Soc.* **72** (3), 512–514 (1989).
- [36] J. A. Costello and R. E. Tressler, Oxidation Kinetics of Silicon Carbide Crystals and Ceramics, *J. Am. Ceram. Soc.* **69** (9), 674–681 (1986).
- [37] R. E. Tressler, K. E. Spear, Z. Zheng, and H. Du, Fundamental Studies of the Oxidation of Silicon Carbide Crystals and CVD Silicon Nitride, in *High Temperature Corrosion of Technical Ceramics*, R. J. Fordham, ed., Elsevier Applied Science (1990) pp. 69–89.
- [38] F. L. Riley and M. A. Lamkin, High Temperature Liquid Corrosion of Non-Oxide Ceramics, in *High Temperature Corrosion of Technical Ceramics*, R. J. Fordham, ed., Elsevier Applied Science (1990) pp. 143–160.
- [39] F. F. Lange, Healing of Surface Cracks in SiC by Oxidation, *J. Am. Ceram. Soc.* **53** (5), 290 (1970).
- [40] T. E. Easler, R. C. Brandt, and R. E. Tressler, Strength Distributions of SiC Ceramics after Oxidation and Oxidation under Load, *J. Am. Ceram. Soc.* **64** (12), 731–734 (1981).
- [41] P. F. Becher, Strength Retention in SiC Ceramics after Long-Term Oxidation, *Communications Am. Ceram. Soc.* **66** (8), C-120–C-121 (1983).
- [42] Y. Tsai, R. E. Tressler, and C. Near, Reliability of Silicon Carbide in Combustion Environments, Final Report, Research Project 2260-2, Electric Power Research Institute (1987).
- [43] D. W. Readey, Gaseous Corrosion of Ceramics, in *Ceramic Transactions, Vol. 10, Corrosion and Corrosive Degradation of Ceramics*, R. E. Tressler, ed., American Ceramic Society, Inc. (1989) pp. 53–80.
- [44] H. E. Kim and A. J. Moorhead, Effects of Gaseous Corrosion on the Strength of SiC and Si₃N₄, in *Ceramic Transactions, Vol. 10, Corrosion and Corrosive Degradation of Ceramics*, R. E. Tressler, ed., American Ceramic Society, Inc. (1989) pp. 81–96.

- [45] D. P. Butt, R. E. Tressler, K. E. Spear, Durability of SiC Materials in Gaseous N_2 - H_2 -CO Heat Treatment Environments, *Center Adv. Mater. Newslett.* **5** (1), 1–12 (1991).
- [46] R. E. Tressler, M. D. Meiser, and T. Yonushonis, Molten Salt Corrosion of SiC and Si_3N_4 Ceramics, *J. Am. Ceram. Soc.* **59** (5–6), 278–279 (1976).
- [47] N. S. Jacobson, Kinetics and Mechanism of Corrosion of SiC by Molten Salts, *J. Am. Ceram. Soc.* **69** (1), 74–82 (1986).
- [48] J. I. Federer, Corrosion of SiC Ceramics by Na_2SO_4 , *Adv. Ceram. Mater.* **3** (1), 56–61 (1988).
- [49] See Ref. [48].
- [50] D. W. McKee and D. Chatterji, Corrosion of Silicon Carbide in Gases and Alkaline Melts, *J. Am. Ceram. Soc.* **59** (9–10), 441–444 (1976).
- [51] N. S. Jacobson, J. L. Smialek, and D. S. Fox, High Temperature Corrosion of Engineering Ceramics, in *Corrosion of Glass, Ceramics and Ceramic Superconductors: Principles, Testing, Characterization and Applications*, D. E. Clark and B. K. Zaitos, eds., Noyes (1992) pp. 514–545.
- [52] J. L. Smialek and N. S. Jacobson, Mechanism of strength for hot corrosion of α -SiC, *J. Am. Ceram. Soc.* **69** (10), 741–752 (1986).
- [53] J. Masters, Ceramic Immersion Heaters for Molten Metal Processing, *Center Adv. Mater. Newsletter* **3** (2), 29–35 (1989).
- [54] J. I. Federer and T. N. Tieg, Analysis of Candidate Silicon Carbide Recuperator Materials Exposed to Industrial Furnace Environments, in *Advances in Ceramics*, Vol. 14, B. D. Foster and J. B. Patton, eds., American Ceramic Society, Inc. (1985) pp. 315–334.
- [55] J. Luyten, P. Lemaitre, and A. Stalios, High Temperature Corrosion of Silicon Nitride and Silicon Carbide Exposed to the Flue Gases of an Aluminum Remelting Furnace, in *High Temperature Corrosion of Technical Ceramics*, R. J. Fordham, ed., Elsevier Applied Science (1990) pp. 161–168.
- [56] M. K. Ferber and V. J. Tennery, Behavior of Tubular Ceramic Heat Exchanger Materials in Acidic Coal Ash from Coal-Oil-Mixture Combustion, *Ceram. Bull.* **62** (2), 236–243 (1983).
- [57] J. A. Bonar, C. R. Kennedy, and R. B. Swaroop, Coal-Ash Slag Attack and Corrosion of Refractories, *Ceram. Bull.* **59** (4), 473–478 (1980).
- [58] See Ref. [56].
- [59] M. K. Ferber and V. J. Tennery, Behavior of Tubular Ceramic Heat Exchanger Materials in Basic Coal Ash from Coal-Oil-Mixture Combustion, *Ceram. Bull.* **63** (7), 898–904 (1984).
- [60] T. E. Easler and R. B. Poeppel, Corrosion of Ceramics in Heat Exchanger Applications, in *High Temperature Corrosion in Energy Systems*, M. F. Rothman, ed., Metallurgical Society of AIME (1985) pp. 269–280.
- [61] See Ref. [59].
- [62] M. K. Ferber, J. Ogle, V. J. Tennery, and T. Henson, Characterization of Corrosion Mechanisms Occurring in a Sintered SiC Exposed to Basic Coal Slags, *J. Am. Ceram. Soc.* **68** (4), 191–197 (1985).
- [63] See Ref. [62].
- [64] P. F. Becher, Strength Degradation in SiC and Si_3N_4 Ceramics by Exposure to Coal Slags at High Temperatures, *J. Mater. Sci.* **19**, 2805–2814 (1984).
- [65] M. L. Torti, The Silicon Nitride and Sialon Families of Structural Ceramics, in *Treatise on Materials Science and Technology*, Volume 29, Structural Ceramics, J. B. Wachtman, Jr., ed., Academic Press (1989) pp. 161–194.
- [66] S. Hampshire, Engineering Properties of Nitrides in Engineered Materials Handbook, Volume 4, Ceramics and Glasses, S. J. Schneider, Jr., ed., ASM International (1991) pp. 812–820.
- [67] M. J. Pomeroy and S. Hampshire, Oxidation Processes in Silicon Nitride Ceramics, *Mater. Sci. Eng.* **15**, 443–448 (1980).
- [68] H. Du, R. E. Tressler, K. E. Spear, and C. G. Pantano, Oxidation Studies of Crystalline CVD Silicon Nitride, *J. Electrochem. Soc.* **136** (5), 1527–1536 (1989).
- [69] A. J. Kiehle, L. K. Heung, P. J. Gielisse, and T. J. Rockett, Oxidation Behavior of Hot-Pressed Si_3N_4 , *J. Am. Ceram. Soc.* **58** (1–2), 17–20 (1975).
- [70] W. C. Tripp and H. C. Graham, Oxidation of Si_3N_4 in the Range 1300° to 1500°C, *J. Am. Ceram. Soc.* **59** (9–10), 399–403 (1976).
- [71] F. F. Lange, Phase Relations in the System Si_3N_4 - SiO_2 -MgO and Their Inter-Relation with Strength and Oxidation, *J. Am. Ceram. Soc.* **61** (1–2), 53–56 (1978).
- [72] M. Desmaison-Brut and M. Billy, High Temperature Corrosion of Hot Pressed Silicon Nitride Materials, in *High Temperature Corrosion of Technical Ceramics*, R. J. Fordham, ed., Elsevier Applied Science (1990) pp. 131–140.
- [73] K. G. Nickel, R. Danzer, G. Schneider, and G. Petzow, Corrosion and Oxidation of Advanced Ceramics, *Powder Metallurgy Internatl.* **21** (3), 29–34 (1989).
- [74] See Ref. [72].
- [75] J. E. Sheehan, Passive and Active Oxidation of Hot-Pressed Silicon Nitride Materials with Two Magnesia Contents, *J. Am. Ceram. Soc.* **65** (7), C-111–C-113 (1982).
- [76] See Ref. [28].
- [77] T. E. Easler, R. C. Bradt, and R. E. Tressler, Effects of Oxidation and Oxidation Under Load on Strength Distributions of Si_3N_4 , *J. Am. Ceram. Soc.* **65** (6), 317–320 (1982).
- [78] S. C. Singhal, Effect of Water Vapor on the Oxidation of Hot-Pressed Silicon Nitride and Silicon Carbide, *J. Am. Ceram. Soc.* **59** (1–2), 81–82 (1976).
- [79] See Ref. [44].
- [80] M. I. Mayer and F. L. Riley, Sodium-Assisted Oxidation of Reaction-Bonded Silicon Nitride, *J. Mater. Sci.* **13**, 1319–1328 (1978).
- [81] D. S. Fox and N. S. Jacobson, Molten-Salt Corrosion of Silicon Nitride: I, Sodium Carbonate, *J. Am. Ceram. Soc.* **71** (2), 128–138 (1988).
- [82] N. S. Jacobson and D. S. Fox, Molten-Salt Corrosion of Silicon Nitride: II, Sodium Sulfate, *J. Am. Ceram. Soc.* **71** (2), 139–148 (1988).
- [83] See Ref. [55].
- [84] See Ref. [64].
- [85] W. A. Ellingson, K. Natesan, and T. Vojnovich, Materials of Construction, in *The Science and Technology of Coal and Coal Utilization*, Bernard R. Cooper and William A. Ellingson, eds., Plenum Press (1984) pp. 513ff.
- [86] S. Greenberg and R. Poeppel, The Corrosion of Ceramic Refractories Exposed to Synthetic Coal Slags by Means of the Rotating-Cylinder Technique: Final Report, Argonne National Laboratory Report ANL/FE-85-15 (April 1986).
- [87] P. L. Hemmings and R. A. Perkins, Thermodynamic Phase Stability Diagrams for the Analysis of Corrosion Reactions in Coal Gasification/Combustion Atmospheres, EPRI Report FP-539 (December 1977).

- [88] E. A. Gulbranson and G. H. Meier, Thermochemical Stability Diagrams for Condensed Phases and Volatility Diagrams for Volatile Species Over Condensed Phases in Twenty Metal-Sulfur-Oxygen Systems Between 1150 and 1450 K, DOE/FE/13547-01, UC-90h (May 1980).
- [89] E. A. Gulbranson and G. H. Meier, Thermochemical Stability Diagrams for Condensed Phases and Volatility Diagrams for Volatile Species over Condensed Phases in Twenty Metal-Chlorine-Oxygen Systems at 1150 and 1250 K, Department of Metallurgical and Materials Engineering, University of Pittsburgh, DOE Contract DE AC01 79 ET 13547 (January 1983).
- [90] G. M. Kim and G. H. Meier, Breakdown Mechanisms of Preformed Al_2O_3 , Cr_2O_3 and SiO_2 Scales in $\text{H}_2/\text{H}_2\text{O}/\text{H}_2\text{S}$ Environments at 950 °C, DOE Report ORNL/Sub/83-43346/01 (June 1, 1988).
- [91] J. W. Vogan and A. R. Stetson, Advanced Ceramic Coating Development for Industrial/Utility Gas Turbines, NASA Report Cr 169852 (January 1982).
- [92] C. A. Anderson, S. K. Lau, R. J. Bratton, S. Y. Lee, K. L. Rieke, J. Allen, and K. E. Munson, Advanced Ceramic Coating Development for Industrial/Utility Gas Turbine Applications, NASA Report CR-65919 (February 1982).
- [93] R. L. Jones, Thermogravimetric Study of the 800 °C Reaction of Zirconia Stabilizing Oxides with $\text{SO}_3\text{-NaVO}_3$, J. Electrochem. Soc. **139** (10), 2794–2799 (1992).
- [94] M. H. Van de Voorde, M. G. Hocking, and V. Vasantasrea, A Comprehensive Review of the Development of Ceramic Coatings for Thermomechanical Applications, High Temp. Mater. Processes **7** (2–3), 107–121 (1986).
- M. Desmanson-Brut and M. Billy, High Temperature Corrosion of Hot Pressed Silicon Nitride Materials, in High Temperature Corrosion of Technical Ceramics, R. J. Fordham, ed., Elsevier Applied Science (1990) pp. 131–140.
- H. Du, R. E. Tressler, K. E. Spear, and C. G. Pantano, Oxidation Studies of Crystalline CVD Silicon Nitride, J. Electrochem. Soc. **136** (5), 1527–1536 (1989).
- T. E. Easler, R. C. Brandt, and R. E. Tressler, Strength Distributions of SiC Ceramics after Oxidation and Oxidation under Load, J. Am. Ceram. Soc. **64** (12), 731–734 (1981).
- T. E. Easler, R. C. Brandt, and R. E. Tressler, Effects of Oxidation and Oxidation Under Load on Strength Distributions of Si_3N_4 , J. Am. Ceram. Soc. **65** (6), 317–320 (1982).
- G. Ervin, Jr., Oxidation Behavior of Silicon Carbide, J. Am. Ceram. Soc. **44** (9), 347–352 (1958).
- R. Forthmann and A. Naoumidis, Influence of the High-Temperature Corrosion by Different Gaseous Environments on the Bending Strength of SiC Materials, Werkstoffe Korrosion **41**, 728–733 (1990).
- C. D. Fung and J. J. Kopanski, Thermal Oxidation of 3C Silicon Carbide Single-Crystal Layers on Silicon, Appl. Phys. Lett. **45** (7), 757–759 (1984).
- A. Georges, B. Courrier, C. Gleitzer, Appraisal of SiC Oxidation Protection of Alumina-Graphite Refractories, I-Carbon Dioxide Oxidation at 1400 °C and 1500 °C, British Ceram. Trans. J. **86**, 124–128 (1987).

7. Topical Bibliography

Oxidation

- P. Andrews and F. L. Riley, Silicon Nitride Oxidation/Re-oxidation, J. European Ceram. Soc. **7**, 125–132 (1991).
- J. E. Antill and J. B. Warburton, Active to Passive Transition in the Oxidation of SiC, Corrosion Sci. **11**, 337–342 (1971).
- P. F. Becher, Strength Retention in SiC Ceramics after Long-Term Oxidation, Communications Am. Ceram. Soc. **66** (8), C-120–C-121 (1983).
- J. A. Costello and R. E. Tressler, Oxidation Kinetics of Hot-Pressed and Sintered $\alpha\text{-SiC}$, J. Am. Ceram. Soc. **64** (6) 327–331 (1981).
- J. A. Costello and R. E. Tressler, Oxidation Kinetics of Silicon Carbide Crystals and Ceramics, J. Am. Ceram. Soc. **69** (9), 674–681 (1986).
- J. A. Costello, R. E. Tressler, and I. S. T. Tsong, Boron Redistribution in Sintered $\alpha\text{-SiC}$ During Thermal Oxidation, J. Am. Ceram. Soc. **64** (6), 332–335 (1981).
- D. Cubicciotti and K. H. Lau, Kinetics of Oxidation of Hot-Pressed Silicon Nitride Containing Magnesia, J. Am. Ceram. Soc. **61** (11–12), 512–517 (1978).
- D. Cubicciotti and K. H. Lau, Kinetics of Oxidation of Yttria Hot-Pressed Silicon Nitride, J. Electrochem. Soc. **126** (10), 1723–1728 (1979).
- E. A. Gulbransen, K. F. Andrew, and F. A. Brassart, The Oxidation of Silicon Carbide at 1150 to 1400 °C and at 9×10^{-3} to 5×10^{-1} Torr Oxygen Pressure, J. Electrochem. Soc. **113** (12), 1311–1314 (1966).
- E. A. Gulbransen and S. A. Jansson, The High-Temperature Oxidation, Reduction, and Volatilization Reactions of Silicon and Silicon Carbide, Oxidation Metals **4** (3), 181–201 (1972).
- R. C. A. Harris, Oxidation of 6H- α Silicon Carbide Platelets, J. Am. Ceram. Soc. **58** (1–2), 7–9 (1975).
- J. W. Hinze and H. C. Graham, The Active Oxidation of Si and SiC in the Viscous Gas-Flow Regime, J. Electrochem. Soc. **123** (7), 1066–1073 (1976).
- R. M. Horton, Oxidation Kinetics of Powdered Silicon Nitride, J. Am. Ceram. Soc. **52**, (3), 121–124 (1969).
- P. J. Jorgensen, M. E. Wadsworth, and I. B. Cutler, Oxidation of Silicon Carbide, J. Am. Ceram. Soc. **42**, (12), 613–616 (1959).
- A. J. Kiehle, L. K. Heung, P. J. Gielisse, and T. J. Rockett, Oxidation Behavior of Hot-Pressed Si_3N_4 , J. Am. Ceram. Soc. **58**, (1–2), 17–20 (1975).
- M. Landon, P. Goeuriot, and F. Thevenot, Oxidation Behavior of SiC-AlN Ceramic Materials, J. European Ceram. Soc. **7**, 279–283 (1991).

- F. F. Lange, Healing of Surface Cracks in SiC by Oxidation, *J. Am. Ceram. Soc.* **53**, (5), 290 (1970).
- F. F. Lange, Phase Relations in the System $\text{Si}_3\text{N}_4\text{-SiO}_2\text{-MgO}$ and Their Inter-Relation with Strength and Oxidation, *J. Am. Ceram. Soc.* **61**, (1–2), 53–56 (1978).
- S. B. Lasday, Advanced Ceramics Broaden Applicability and Performance of Products in Heat and Corrosion Resistant Uses, *Industrial Heating*, 20–24 (December 1988).
- A. C. Lea, Oxidation of Silicon Carbide Refractory Materials, *J. Soc. Glass Technol.* **33**, 27–50T (1949).
- J. Li, P. Eveno, and A. M. Huntz, Oxidation of SiC, *Werkstoffe Korrosion* **41**, 716–725 (1990).
- V. L. K. Lou and A. H. Heuer, Graphical Displays of the Thermodynamics of High-Temperature Gas-Solid Reactions and Their Applications in High Temperature Corrosion of Technical Ceramics, R. J. Fordham, ed., Elsevier Applied Science, New York (1990) pp. 33–52.
- M. Maeda, K. Nakamura, and M. Yamada, Oxidation Resistance Evaluation of Silicon Carbide Ceramics with Various Additives, *J. Am. Ceram. Soc.* **72**, (3), 512–514 (1989).
- C. O'Meara, J. Sjöberg, G. Dunlop, and R. Pompe, Oxidation of Pressureless Sintered $\text{Si}_2\text{N}_2\text{O}$ Materials, *J. European Ceram. Soc.* **7**, 369–378 (1991).
- D. M. Mieskowski, T. E. Mitchell, and A. H. Heuer, Bubble Formation in Oxide Scales on SiC, *J. Am. Ceram. Soc.* **67** (1), C-17–C-18 (1984).
- T. Narushima, T. Goto, and T. Hirai, High-Temperature Passive Oxidation of Chemically Vapor Deposited Silicon Carbide, *J. Am. Ceram. Soc.* **72** (8), 1386–1390 (1989).
- K. G. Nickel, The Role of Condensed Silicon Monoxide in the Active-to-Passive Oxidation Transition of Silicon Carbide, *J. European Ceram. Soc.* **9** (1), 3–8 (1992).
- K. G. Nickel, R. Danzer, G. Schneider, and G. Petzow, Corrosion and Oxidation of Advanced Ceramics, *Powder Metallurgy Intl.* **21** (3), 29–34 (1989).
- L. U. Ogbuji, Development of Oxide Scale Microstructure on Single-Crystal SiC, *J. Mater. Sci.* **16** (10), 2753–2759 (1981).
- M. J. Pomeroy and S. Hampshire, Oxidation Processes in Silicon Nitride Ceramics, *Mater. Sci. Engin.* **15**, 443–448 (1980).
- W. W. Pultz, Temperature and Oxygen Pressure Dependence of Silicon Carbide Oxidation, *J. Phys. Chem.* **71** (13), 4556–4558 (1967).
- W. W. Pultz and W. Hertl, $\text{SiO}_2\text{+SiC}$ Reaction at Elevated Temperatures, *Trans. Faraday Soc.* **62**, 2499–2504 (1966).
- P. Reagan, A. N. Scoville, R. Leaf, W. Cole, and F. Huffman, CVD Technology for Heat Exchangers and Heat Pipes, in *Ceramics in Heat Exchangers*, Advances in Ceramics, Vol. 14, B. D. Foster and J. B. Patton, eds., American Ceramic Society Inc. (1985) pp. 301–308.
- F. L. Riley and M. A. Lamkin, High Temperature Liquid Corrosion of Non-Oxide Ceramics, in *High Temperature Corrosion of Technical Ceramics*, R. J. Fordham, ed., Elsevier Applied Science (1990) pp. 143–160.
- J. E. Sheehan, Passive and Active Oxidation of Hot-Pressed Silicon Nitride Materials with Two Magnesia Contents, *J. Am. Ceram. Soc.* **65**, (7), C-111–C-113 (1982).
- M. Shimada, T. Yonezawa, and M. Koizumi, Oxidation of High Pressure Hot-Pressed Si_3N_4 without Additives, Seventh Annual Conference on Materials for Coal Conversion and Utilization, S. J. Schneider, ed., Natl. Bur. Stands. (1982), pp. 129–136.
- S. C. Singhal, Thermodynamic Analysis of the High-Temperature Stability of Silicon Nitride and Silicon Carbide, *Ceramurgia Intl.* **2** (3), 123–130 (1976).
- S. C. Singhal, Oxidation Kinetics of Hot-Pressed Silicon Carbide, *J. Mater. Sci.* **11** (7), 1246–1253 (1976).
- S. C. Singhal and F. F. Lange, Effect of Alumina Content on the Oxidation of Hot-Pressed Silicon Carbide, *J. Am. Ceram. Soc.* **58** (9–10), 433–435 (1975).
- R. E. Tressler, J. A. Costello, and Z. Zheng, Oxidation of Silicon Carbide Ceramics, in *Industrial Heat Exchangers*, A. J. Hayes, W. W. Liang, S. L. Richlen, and E. S. Tabb, eds., American Society for Metals (1985) pp. 307–314.
- R. E. Tressler, K. E. Spear, Z. Zheng, and H. Du, Fundamental Studies of the Oxidation of Silicon Carbide Crystals and CVD Silicon Nitride, in *High Temperature Corrosion of Technical Ceramics*, R. J. Fordham, ed., Elsevier Applied Science (1990) pp. 69–89.
- W. C. Tripp and H. C. Graham, Oxidation of Si_3N_4 in the Range 1300 to 1500 °C, *J. Am. Ceram. Soc.* **59** (9–10), 399–403 (1976).
- Y. Tsai, R. E. Tressler, and C. Near, Reliability of Silicon Carbide in Combustion Environments, Final Report, Research Project 2260-2, Electric Power Research Institute (1987).
- O. Van der Biest and C. Weber, Effects of Oxidation on Long Term Failure of Silicon Nitride, *Ceramic Transactions*, Vol. 10, Corrosion and Corrosive Degradation of Ceramics, R. E. Tressler and M. McNallan, eds., American Ceramic Society (1989) pp. 125–139.
- W. L. Vaughn and H. G. Maahs, Active-to-Passive Transition in the Oxidation of Silicon Carbide and Silicon Nitride in Air, *J. Am. Ceram. Soc.* **73**, (6), 1540–1543 (1990).
- C. Wagner, Passivity During the Oxidation of Silicon at Elevated Temperatures, *J. Appl. Phys.* **29**, 1295–1297 (1958).

Hot Gases

W. Bremen, A. Naoumidis, and H. Nickel, Oxidation Behavior of Pyrolytic Deposited $\beta\text{-SiC}$ under an Atmosphere of $\text{Co}=\text{CO}_2$ Gas Mixtures, *J. Nucl. Mater.* **71**, 56–64 (1977).

D. P. Butt, R. E. Tressler, and K. E. Spear, Durability of SiC Materials in Gaseous $\text{N}_2\text{-H}_2\text{-CO}$ Heat Treatment Environments, *Center Adv. Mater. Newslett.* **5**, (1), 1–12 (1991).

- H. Hirayama, T. Kawakubo, and A. Goto, Corrosion Behavior of Silicon Carbide in 290 °C Water, *J. Am. Ceram. Soc.* **72** (11), 2049–2053 (1989).
- P. J. Jorgensen, M. E. Wadsworth, and I. B. Cutler, Effects of Water Vapor on Oxidation of Silicon Carbide, *J. Am. Ceram. Soc.* **44** (6), 258–261 (1961).
- W. A. Kern, R. E. Tressler, and M. J. McNallan, Durability of SiC/Al₂O₃ Composites in Contact with Sodium Silicate, *Center Adv. Mater. Newslett.* **6** (1), 1ff (1992).
- H. E. Kim and A. J. Moorhead, Effects of Gaseous Corrosion on the Strength of SiC and Si₃N₄, in *Ceramic Transactions, Vol. 10, Corrosion and Corrosive Degradation of Ceramics*, R. E. Tressler, ed., American Ceramic Society, Inc. (1989) pp. 81–96.
- M. J. McNallan, W. W. Liang, and M. F. Rothman, High Temperature Corrosion of Metallic and Ceramic Heat Exchanger Materials in Chlorine Contaminated Environments, in *Industrial Heat Exchangers*, A. J. Hayes, W. W. Liang, S. L. Richlen, and E. S. Tabb, eds., American Society for Metals (1985) pp. 293–298.
- D. S. Park, M. J. McNallan, C. Park, and W. W. Liang, Active Corrosion of Sintered α -Silicon Carbide in Oxygen-Chlorine Gases at Elevated Temperatures, *J. Am. Ceram. Soc.* **73**, (5), 1323–1329 (1990).
- D. W. Readey, Gaseous Corrosion of Ceramics, in *Ceramic Transactions, Vol. 10, Corrosion and Corrosive Degradation of Ceramics*, R. E. Tressler, ed., American Ceramic Society, Inc. (1989) pp. 53–80.
- M. Shimada and Tsugio Sato, Corrosion of Silicon Nitride Ceramics in HF and HCl Solutions, *Ceramic Transactions, Vol. 10, Corrosion and Corrosive Degradation of Ceramics*, R. E. Tressler and M. McNallan, eds., American Ceramic Society, (1989) pp. 355–365.
- S. C. Singhal, Effect of Water Vapor on the Oxidation of Hot-Pressed Silicon Nitride and Silicon Carbide, *J. Am. Ceram. Soc.* **59** (1–2), pp. 81–82 (1976).
- M. Yoshimura, J. Kase, M. Hayakawa, and S. Somiya, Oxidation Mechanism of Nitride and Carbide Powders by High-Temperature, High-Pressure Water, *Ceramic Transactions, Vol. 10, Corrosion and Corrosive Degradation of Ceramics*, R. E. Tressler and M. McNallan, eds., American Ceramic Society (1989) pp. 337–354.
- Molten Salts*
- D. P. Butt and J. J. Mecholsky, Jr., Effects of Sodium Silicate Exposure at High Temperature on Sintered α -Silicon Carbide and Siliconized Silicon Carbide, *J. Am. Ceram. Soc.* **72**, (9), pp. 1628–1635 (1989).
- J. W. Cree and M. F. Amateau, Mechanical Behavior of SiC Exposed to Molten Lithium and Lithium Salts, *Ceram. Eng. Sci. Proc.* **8** (7–8), 812–814 (1987).
- J. I. Federer, Corrosion of SiC Ceramics by Na₂SO₄, *Adv. Ceram. Mater.* **3** (1), 56–61 (1988).
- D. S. Fox and N. S. Jacobson, Molten-Salt Corrosion of Silicon Nitride: I, Sodium Carbonate, *J. Am. Ceram. Soc.* **71** (2), 128–138 (1988).
- N. S. Jacobson, Kinetics and Mechanism of Corrosion of SiC by Molten Salts, *J. Am. Ceram. Soc.* **69** (1), 74–82 (1986).
- N. S. Jacobson, Sodium Sulfate: Deposition and Dissolution of Silica, *Oxidation Metals* **31** (1–2), 91–103 (1989).
- N. S. Jacobson and D. S. Fox, Molten-Salt Corrosion of Silicon Nitride: II, Sodium Sulfate, *J. Am. Ceram. Soc.* **71** (2), 139–148 (1988).
- N. S. Jacobson and J. L. Smialek, Hot Corrosion of Sintered α -SiC at 1000 °C, *J. Am. Ceram. Soc.* **68** (8), 432–439 (1985).
- N. S. Jacobson, J. L. Smialek, and D. S. Fox, High Temperature Corrosion of Engineering Ceramics in Corrosion of Glass, Ceramics and Ceramic Superconductors: Principles, Testing, Characterization and Applications, D. E. Clark and B. K. Zoitos, eds., Noyes (1992) pp. 514–545.
- N. S. Jacobson, C. A. Stearns, and J. L. Smialek, Burner Rig Corrosion of SiC at 1000 °C, *Adv. Ceram. Mater.* **1** (2), 154–161 (1986).
- M. G. Lawson, H. R. Kim, F. S. Pettit, and J. R. Blachere, Hot Corrosion of Silica, *J. Am. Ceram. Soc.* **73** (4), 989–995 (1990).
- M. I. Mayer and F. L. Riley, Sodium-Assisted Oxidation of Reaction-Bonded Silicon Nitride, *J. Mater. Sci.* **13**, 1319–1328 (1978).
- D. W. McKee and D. Chatterji, Corrosion of Silicon Carbide in Gases and Alkaline Melts, *J. Am. Ceram. Soc.* **59** (9–10), 441–444 (1976).
- V. Pareek and D. A. Shores, Oxidation of Silicon Carbide in Environments Containing Potassium Salt Vapor, *J. Am. Ceram. Soc.* **74** (3) 556–563 (1991).
- J. L. Smialek and N. S. Jacobson, Mechanism of strength degradation for hot corrosion of α -SiC, *J. Am. Ceram. Soc.* **69** (10), 741–752 (1986).
- R. E. Tressler, Corrosion of Advanced Structural Ceramics, *Center Adv. Mater. Newslett.* **2** (1), 1ff (1988).
- R. E. Tressler, Corrosion Consideration for Materials in Natural-Gas-Fired Systems, *Center Adv. Mater. Newslett.* **3** (2), 44ff (1989).
- R. E. Tressler, M. D. Meiser, and T. Yonushonis, Molten Salt Corrosion of SiC and Si₃N₄ Ceramics, *J. Am. Ceram. Soc.* **59** (5–6), 278–279 (1976).
- Molten Metals*
- J. W. Cree and M. F. Amateau, Mechanical Behavior of SiC Exposed to Molten Lithium, *J. Am. Ceram. Soc.* **70** (11), C-318–C-321 (1991).

- J. I. Federer, High-Temperature corrosion of Heat Exchanger Materials, *Ceramic Transactions*, Vol. 10, Corrosion and Corrosive Degradation of Ceramics, R. E. Tressler and M. McNallan, eds., American Ceramic Society (1989) pp. 425–443.
- J. I. Federer and T. N. Tiegs, Analysis of Candidate Silicon Carbide Recuperator Materials Exposed to Industrial Furnace Environments, in *Advances in Ceramics*, Vol. 14, B. D. Foster and J. B. Patton, eds., American Ceramic Society, Inc. (1985) pp. 315–334.
- J. Luyten, P. Lemaitre, and A. Stalios, High Temperature Corrosion of Silicon Nitride and Silicon Carbide Exposed to the Flue Gases of an Aluminum Remelting Furnace, in *High Temperature Corrosion of Technical Ceramics*, R. J. Fordham, ed., Elsevier Applied Science (1990) pp. 161–168.
- J. Masters, Ceramic Immersion Heaters for Molten Metal Processing, *Center Adv. Mater. Newslett.* 3 (2), 29–35 (1989).
- U. Schwabe, L. R. Wolff, F. van Loo, and G. Ziegler, Corrosion of Technical Ceramics by Molten Aluminium, *J. European Ceram. Soc.* 9 (6), 407–415 (1992).
- W. Sinclair, A. M. MacDonald, and M. B. Trigg, Evaluation of Non-Oxide Ceramics for Steel Making, *Mater. Forum* 10 (3), 211–213 (1987).
- C. E. Smeltzer, T. A. Arabright, M. E. Ward, and W. Liang, An Investigation of the Hot-Corrosion of Silicon Carbide (SiC) Recuperator Tubes in Aluminum Remelt Furnace Stacks in Industrial Heat Exchangers, A. J. Hayes, W. W. Liang, S. L. Richlen, and E. S. Tabb, eds., American Society for Metals (1985) pp. 299–305.
- Complex Environments*
- J. W. Adams, D. C. Larsen, and R. Ruh, Corrosion of SiC, Si₃N₄, and Oxide Ceramics in Coal Gas Combustion Products in Industrial Heat Exchangers, A. J. Hayes, W. W. Liang, S. L. Richlen, and E. S. Tabb, eds., American Society for Metals (1985) pp. 315–321.
- P. F. Becher, Strength Degradation in SiC and Si₃N₄ Ceramics by Exposure to Coal Slags at High Temperatures, *J. Mater. Sci.* 19, 2805–2814 (1984).
- J. A. Bonar, C. R. Kennedy, and R. B. Swaroop, Coal-Ash Slag Attack and Corrosion of Refractories, *Ceram. Bull.* 59 (4), 473–478 (1980).
- H. W. Carpenter, Durability of SiC Heat-Exchanger Tubes in a High-Temperature Fluidized Bed, in *Ceramics in Heat Exchangers*, *Advances in Ceramics*, Vol. 14, B. D. Foster and J. B. Patton, eds., American Ceramic Society, Inc. (1985) pp. 345–358 (1985).
- A. L. Dragoo and J. L. Waring, The Reaction of Silicon Carbide with Product Gases of Coal Combustion, Seventh Annual Conference on Materials for Coal Conversion and Utilization, S. J. Schneider, ed., *Natl. Bur. Stands. (U.S.)* (1982) pp. 161–176.
- T. E. Easler and R. B. Poeppel, Corrosion of Ceramics in Heat Exchanger Applications, in *High Temperature Corrosion in Energy Systems*, M. F. Rothman, ed., Metallurgical Society of AIME (1985) pp. 269–280.
- M. K. Ferber, J. Ogle, V. J. Tennery, and T. Henson, Characterization of Corrosion Mechanisms Occurring in a Sintered SiC Exposed to Basic Coal Slags, *J. Am. Ceram. Soc.* 68 (4), 191–197 (1985).
- M. K. Ferber and V. J. Tennery, Evaluation of Tubular Ceramic Heat Exchanger Materials in Acidic Coal Ash from Coal-Oil-Mixture Combustion, ORNL/TM-7958 (1981).
- M. K. Ferber and V. J. Tennery, Evaluation of Tubular Ceramic Heat Exchanger Materials in Basic Coal Ash from Coal-Oil-Mixture Combustion, ORNL/TM-8385 (1982).
- M. K. Ferber and V. J. Tennery, Behavior of Tubular Ceramic Heat Exchanger Materials in Acidic Coal Ash from Coal-Oil-Mixture Combustion, *Ceram. Bull.* 62 (2) 236–243 (1983).
- M. K. Ferber and V. J. Tennery, Behavior of Tubular Ceramic Heat Exchanger Materials in Basic Coal Ash from Coal-Oil-Mixture Combustion, *Ceram. Bull.* 63 (7), 898–904 (1984).
- I. Sekercioglu, R. Razgaitis, and J. Lux, Evaluation of Ceramics for Condensing Heat-Exchanger Applications, in *Ceramics in Heat Exchangers*, *Advances in Ceramics*, Vol. 14, B. D. Foster and J. B. Patton, eds., American Ceramic Society, Inc. (1985), pp. 359–370 (1985).
- G. C. Wei and V. J. Tennery, Evaluation of Tubular Ceramic Heat Exchanger Materials in Residual Oil Combustion Environments, ORNL/TM-7578 (1981).

About the Authors: R. G. Munro and S. J. Dapkunas are staff members in the Ceramics Division, Materials Science and Engineering Laboratory, NIST. The National Institute of Standards and Technology is an agency of the Technology Administration, U.S. Department of Commerce.

3. NIUF Objectives and Structure

The NIUF seeks to achieve three principal goals:

- To promote an ISDN forum committed to providing users the opportunity to influence developing ISDN technology to reflect their needs;
- To identify ISDN applications, develop implementation requirements, and facilitate their timely, harmonized, and interoperable introduction; and
- To solicit user, product provider, and service provider participation in the process.

The actual work of the NIUF is accomplished in two workshops: the ISDN User's Workshop (IUW) and the ISDN Implementor's Workshop (IIW). The IUW produces application requirements which describe potential applications of ISDN and the features which may be needed. The IIW develops application profiles, implementation agreements, and conformance criteria which provide the detailed technical decisions necessary to implement an application requirement in an interoperable manner. The NIUF Executive Steering Committee coordinates the activities of the two workshops.

4. NIUF Achievements

Since its inception in 1988, the NIUF has achieved the following:

- 141 active applications for development of application profiles have been accepted;
- application profiles have been completed for 14 applications;
- 15 implementation agreements have been completed; and
- 8 conformance tests have been completed.

CSL established the NIST Special Publication 823 series, Integrated Service Digital Network Technology Publications, to publish the approved implementation agreements, conformance tests, and other NIUF documents. Copies of these documents are available for sale by the U.S. Government Printing Office, (202) 783-3238 or the National Technical Information Service, (703) 487-4650.

5. Highlights of June 1993 NIUF

Tutorials presented at the June meeting included an overview of the NIUF for new users and new implementors; migration to broadband ISDN; basic ISDN; applications software interface; and national ISDN user applications.

Highlights from the Executive Steering Committee Standing Groups included a presentation by Pat Donovan, Bell Atlantic, on the provisional definition of National ISDN-3. The presentation was part of the National ISDN Planning Process that is an ongoing part of NIUF activities. The panel discussion following the talk featured representatives from AT&T, NTI, Siemens Stromberg-Carlson, Ericsson, and Ameritech.

The IUW held its first General User Meeting in order to cover topics of interest to a wide range of users and implementors. A resounding success in terms of attendance and interest generated by the topics, the meeting focused on three main topics: the current state of ISDN tariffs in the United States and Canada; the status of the Tennessee Public Utilities Commission ISDN field trials; and a panel discussion on the impact of the Clean Air Act Amendment on state and local governments and the use of telecommuting as a potential solution.

IUW Working Group highlights included the following: the Broadband ISDN Working Group presented tutorials on Switched Multimegabit Data Service (SMDS) and the North Carolina Broadband Network; the Enterprise Network Data Interconnectivity Family (ENDIF) discussed the need for interoperability among different vendors for ISDN applications involving access to LANs and between LANs, and proposed a demonstration for the October meeting; the Government Services Industry Group (GSIG) identified three high-profile items for the GSIG to address through the forum: ISDN and GOSIP compatibility, the definition of managed objects for secure network management, and secure video conferencing; the Private Industries Group decided to try to develop an initial Quality Index figure to measure the availability and usability of ISDN as it applies to the companies represented, and discussed packet data services over ISDN and the lack of well-defined service parameters among the various exchange carriers; the Call Management Family continued to advance the Telecommuting Application Profile, with the goal of presenting a stable

draft at the October NIUF; and the Messaging and Answering Family heard a presentation by Jim Rothweiler, Bellcore, on a survey assessing five new features that will support the voice messaging industry in providing service to the consumer market.

The IIW approved three documents and declared six documents as working group stable (see plenary highlights below). Glenn Ehley, IIW Chair, proposed an increased participation drive. One recommendation was the use of graduate students to assist with the application analysis process. Also identified was the need for a Broadband Application Profile Team.

IIW Working Groups reported the following activities: ISDN CPE and Software Working Group (ICSW) heard presentations on the implementation schedules for National ISDN-2. Ameritech sponsored a session on the Primary Rate ISDN switched fractional services that will become available with National ISDN-2. The ICSW Basic Rate Subcommittee hopes to implement a simplified ISDN ordering procedure by year's end. The ICSW PBX Subcommittee began an effort to facilitate the standardization of the ISDN-based Q.SIG protocols for ISDN PBX interworking. The Application Analysis Technical Working Group helped to advance work on "Interactive Simulation." The forum discussed the initial draft of the second edition of "A Catalog of National ISDN Solutions for Selected NIUF Applications." Proposed publication date is February 1994. The Call Management Profile Team met in three sessions with other groups to discuss the Telecommuting Application Profile. The CPE Compatibilities and Capabilities Profile Team will develop an implementation plan to attract graduate students. The ISDN Conformance Testing Technical Working Groups reported progress in their individual arenas. The Signaling/Supplementary Services (SSWG) Technical Working Group discussed Class II, BRI Trunking, and received support from users and implementors. Finally, the Video/Audio Conferencing Profile Team gave a second review to the Video Conference Application Profile document, which was declared working group stable once two open issues have been resolved.

At the NIUF Banquet, Matt Thomson, Northern Telecom, received a certificate of recognition for his leadership in the NIUF and his work on TRIP '92. InfoWorld magazine recognized the NIUF and Corporation for Open Systems (COS) with the Publisher's Industry Milestone Award for their efforts in the success of TRIP '92.

The closing plenary approved five new documents, including "A Generic Model for ISDN Cost Analysis." Also approved were Working Group Charters for Mass Market Industries; CPE Compatibilities and Capabilities Family; and Issues Family. Seven documents were announced to be working group stable and five new applications were submitted to the IUW.

6. For More Information

For more information about the NIUF and its publications or to obtain conference proceedings, contact the NIUF Secretariat: Dawn Hoffman, Computer Systems Laboratory, National Institute of Standards and Technology, Building 223, Room B364, Gaithersburg, MD 20899-0001; telephone (301) 975-2937 or fax (301) 926-9675.

Conference Report

NORTH AMERICAN INTEGRATED SERVICES DIGITAL NETWORK (ISDN) USERS' FORUM (NIUF) Gaithersburg, MD June 22–25, 1993

Report prepared by

Elizabeth B. Lennon

Computer Systems Laboratory,
National Institute of Standards and Technology,
Gaithersburg, MD 20899-0001

1. Introduction

The Computer Systems Laboratory (CSL), National Institute of Standards and Technology, hosted the eighteenth North American ISDN Users' Forum (NIUF) at its Gaithersburg, Maryland, site on June 22-25, 1993. About 230 users, implementors, and service providers of ISDN technology attended the meeting. CSL collaborated with industry in 1988 to establish the NIUF to ensure that emerging ISDN applications meet the needs of users. A Cooperative Research and Development Agreement (CRDA) with industry was established in 1991 to govern the management of the forum; as of June 1993, the CRDA has 36 signatories from industry and academia. CSL serves as chair of the forum and hosts the NIUF Secretariat. NIUF membership is open to all

interested users, product providers, and service providers; meetings are held three times a year at various locations throughout North America.

2. The Development of ISDN Standards

International standards for ISDN support worldwide communications for the exchange of voice, data, and image information among users, independent of any manufacturer, service provider, or implementation technology. ISDN standards are developed by the International Telecommunication Union-Telecommunication Standardization Sector (ITU-TS) (formerly the International Telephone and Telegraph Consultative Committee [CCITT]) and, for North America in particular, by the Exchange Carriers Standards Association (ECSA) accredited standards committee, T1, under the umbrella of the American National Standards Institute (ANSI).

ISDN standards provide a broad variety of options and parameters to meet many potential needs and applications. To ensure interoperability and terminal portability within the ISDN network and its attendant equipment, a uniform subset of options and parameters must be selected for implementation. Each application usually requires only a subset of total functionality available in the standards; for ISDN products and services to work together in a multi-vendor environment, common sets of options must be selected.

To cope with this proliferation of choices and to provide interoperable products and services which will meet the needs of users, the standards specification process has been augmented to develop application profiles, implementation agreements, and conformance criteria. The NIUF addresses all of these areas.

News Briefs

General Developments

Inquiries about News Briefs, where no contact person is identified, should be referred to the Managing Editor, Journal of Research, National Institute of Standards and Technology, Administration Building, A635, Gaithersburg, MD 20899-0001; telephone: 301/975-3572.

UNITED STATES, RUSSIA DEVELOP OPTICAL IMAGING SYSTEM

NIST and the Institute of Solid State Physics at the Russian Academy of Science have established a cooperative project to study flux distributions in superconducting materials. A magneto-optical measurement system now being operated at NIST (with the assistance of the Russian scientists who developed it) will be used to study the influence of defects in single crystals and in inhomogeneities in bulk samples of barium-yttrium-copper-oxygen ceramic materials. A laboratory director at NIST says, "The cooperative project between the United States and Russia enables us to take advantage of a new concept and technology that enhances our broad base of expertise. The system will offer us an opportunity to focus on many fundamental issues in magnetic measurements, optical microscopy and single crystal growth." For information on the magneto-optical measurement system, contact Debra L. Kaiser, A329 Materials Building, NIST, Gaithersburg, MD 20899-0001, (301) 975-6759.

BIOSENSOR CONSORTIUM ANNOUNCES FIRST MEMBERS

Members of the new Consortium on Advanced Biosensors, six companies and one government agency, are helping NIST launch a new research program to improve biosensor technology. The Environmental Protection Agency has joined the new consortium as an interagency partner. The consortium's goal is to solve problems that prevent

commercialization of many biosensor technologies in U.S. industry. Located at NIST, the consortium can take direct advantage of the institute's scientific expertise and laboratory facilities. CAB's first project is studying ways to eliminate background interference from biosensor signals. In this initial research, scientists are examining how positively and negatively charged proteins bind to a dozen different chemical surfaces. Consortium members will select future projects and support them through yearly membership fees. For more information, contact Howard Weetall, Biosensor Technology Group, A353 Chemistry Building, NIST, Gaithersburg, MD 20899-0001, (301) 975-2628.

STANDARDS WORKING GROUP PLANS MOSCOW MEETING

Industry and government standard officials concerned about the harmonization of standards and conformity assessment measures between the United States and Russia to improve international trade should plan to participate in the third meeting of the Inter-governmental United States/Russian Business Development Committee's Standards Working Group. The meeting will be hosted by the State Committee of the Russian Federation for Standardization, Metrology and Certification (GOSSTANDART) in Moscow, May 24-25, 1994. The group also has been invited to meet with the State Committee of Ukraine on Standardization, Metrology, and Certification in Kiev, May 26-27, 1994 and the Standardization, Metrology and Certification Committee, Council of Ministers, in Minsk, Republic of Belarus, May 30. The Standards Working Group is co-chaired by Stanley I. Warsaw, director of the NIST Office of Standards Services, and Serguei F. Bezverkhi, president of GOSSTANDART. To participate in the meetings, contact Warsaw, A603 Administration Building, NIST, Gaithersburg, MD 20899-0001, (301) 975-4000, fax: (301) 963-2871.

MODELS MEASURE SPEED OF SOUND FOR GAS MIXTURES

Under the sponsorship of the Gas Research Institute, NIST has gathered comprehensive experimental data on the speed of sound of 13 binary and four multicomponent mixtures of natural gas constituents, and has developed mathematical models (equations) from these data. Knowledge of the speed of sound for specific mixtures of gas can be used to calibrate flowmeters used in the sale and transfer of huge quantities of natural gas. Modeling uncertainty averages 0.1 percent over the range of pressure, temperature, and composition encompassing the major region of custody transfer of natural gas. Temperatures ranged from 250 K to 350 K, with pressures running from below 0.5 MPa to over 10 MPa. The gas mixtures were primarily methane with smaller amounts of ethane, nitrogen, carbon dioxide, or propane. NIST Monograph 178, *Speed of Sound Data and Related Models for Mixtures of Natural Gas Constituents* is available from the National Technical Information Service, Springfield, VA 22161, (703) 487-4650, for \$19.50 prepaid. Order by PB 93-200822.

LOCATION EFFECTS IN ORIFICE FLOWMETERS DOCUMENTED

Orifice meters are used extensively to measure the high-volume flow of fluids (such as natural gas) through a pipe. Asymmetric and swirling flows (caused by nearby upstream bends, tees, or constrictions such as a partially closed valve) can make orifice meters inconsistent, so a flow conditioner of one kind or another is generally placed upstream between the meter and the first disturbance. NIST's latest publication on the subject, *Flow Conditioner Location Effects in Orifice Flowmeters* (NIST Technical Note 1356), describes experimental results for four kinds of conditioners and two sizes of orifice meters, 52 mm and 104 mm (2 in and 4 in), with various sizes of orifice plates and various degrees of roughness, using nitrogen gas. TN 1356 is available from the National Technical Information Service, Springfield, VA 22161, (703) 487-4650 for \$19.50 prepaid. Order by PB 93-159457.

KEY ESCROW ENCRYPTION STANDARD PROPOSED

NIST is proposing a voluntary escrowed encryption standard that will help improve the security and privacy of telephone communications while meeting law enforcement needs. The standard specifies use of the SKIPJACK cryptographic algorithm and a method for creating a Law Enforcement Access Field, or LEAF. The LEAF provides a mechanism needed for authorized government agencies to decipher lawfully intercepted encrypted telecommunications. The proposed standard may be used by federal agencies and others in designing and implementing security products and systems to encrypt sensitive, but unclassified data. Specific operations of the algorithm and the LEAF creation method are classified. They are referenced, but not specified, in the standard. The standard is part of a voluntary key escrow encryption program announced by the White House on April 16. The announcement by NIST and information concerning the applicability, implementation and technical aspects of the standard appeared in the July 30 *Federal Register*.

GUIDE HELPS USERS BUILD OPEN SYSTEMS

More and more organizations are realizing that isolated "islands of computing" are not productive. The ideal computing environment is one in which all products interoperate, data can be easily transferred, applications can be used on a variety of systems, and users can interact with all. Many standards and specifications are needed to define an open system environment, and not all have been written. A new NIST catalog can help managers select available specifications that can be used to move toward an open system environment. The guide covers standards for different functions and services that must work together, from the human interface with the computer to applications and interconnections with networks. Known as the *Application Portability Profile* guide, this version updates the initial one issued in April 1991. The APP, *The U.S. Government's Open System Environment Profile, OSE/1 Version 2.0* (NIST SP 500-210) is available for \$6.50 prepaid from the Superintendent of Documents, U.S. Government Printing Office, Washington, DC 20402, (202) 783-3238. Order by stock no. 003-003-03222-1.

**RESEARCHERS HELP CIRCUIT LAYERS
“GET IN LINE”**

A fast, inexpensive method to calibrate alignment systems for photo- and x-ray lithography equipment has been developed by NIST researchers. The measurement procedure allows semiconductor manufacturers to ensure proper “registration” or alignment of successive layers within an integrated circuit with a precision better than 10 nm. This represents a more than fivefold improvement over current alignment calibration methods. Unlike those techniques that require multimillion dollar optical equipment, the NIST procedure relies on a pair of relatively easy-to-make circuit patterns that a manufacturer overlays to “print” a simple, microelectronic test structure. Electrical measurements taken at several points on the structure allow calculation of its length, and in turn, an assessment of proper alignment. A patent application has been filed. For more information, contact Loren Linholm, B360 Technology Building, NIST, Gaithersburg, MD 20899-0001, (301) 975-2052.

**VOLT STANDARD MARKETED WITH NIST
COOPERATION**

With the recent signing of a cooperative research and development agreement, NIST has formalized a long-standing relationship with a private company to continue development of commercial Josephson voltage standard systems. NIST developed the original intrinsic voltage standard in the early 1970's using a Josephson junction (a weak contact between two super-conductors that can convert an easily measured microwave frequency into voltage). An array of Josephson junctions, developed by NIST, forms the heart of the systems sold by the private company. Under the terms of the CRADA, NIST will assist the company in improving the voltage standard, configuring it to meet customer requirements, and making products developed from it conform to accepted metrological practice. The company will provide feedback to NIST on the performance of these devices in a commercial environment. For more information, contact Clark A. Hamilton, Div. 814.03, NIST, Boulder, CO 80303-3328, (303) 497-3740.

**NEW TEST PLANNED FOR PAINT
INDUSTRY'S PALETTE**

A government-industry consortium for seeking a better way to predict the service life of paint was proposed by NIST and the Federal Highway Administration at an October 1993 workshop at NIST's Gaithersburg, MD, headquarters.

The group's goal will be to help the U.S. paint industry get new, highly predictable products more quickly to market. Because of health and environmental concerns, the chemical makeup and manufacturing processing of paints have changed tremendously over the past decade. However, reliable methods of predicting performance have not kept pace. Current methods rely heavily on outdoor exposure tests that are time-consuming and difficult to duplicate. The proposed consortium will develop an assessment protocol based on the fundamental mechanisms that cause paint degradation and will rely more on short-term laboratory tests. The consortium is expected to start in January 1994. For more information, contact Jonathan Martin, B348 Building Research Building, NIST, Gaithersburg, MD 20899-0001, (301) 975-6717.

DNA STANDARD MAKES THE “TOP 100” LIST

A standard developed at NIST to ensure accuracy in forensic DNA analysis has been named one of the “100 most technologically significant new products of the year” by R&D Magazine. Two NIST chemists and a NIST physical scientist were honored for developing the DNA Profiling Standard (Standard Reference Material 2390) at a ceremony on Sept. 9, 1993, at the Chicago Museum of Science and Industry. First made available in August 1992, the NIST DNA Profiling Standard is used by forensic and medical labs that examine patterns in genetic material to calibrate their own DNA profiling techniques. Including this year's honor, NIST researchers have won 75 R&D 100 awards since 1973. To order the DNA Profiling Standard, contact the Standard Reference Materials Program, Rm. 204, Building 202, NIST, Gaithersburg, MD 20899-0001, (301) 975-6776, fax: (301) 948-3730.

**NOVEL CHEMICAL CONCENTRATOR
MAKES DEBUT**

A U.S. patent (5,217,904) has been issued to a physical chemist at NIST's Boulder, CO, laboratories, for a new device that concentrates chemicals faster, more efficiently and cheaper than conventional methods. Such concentrates are used in the analysis of laboratory and environmental samples. The apparatus operates by compressed air, emitting hot and cold air streams from a vortex tube to provide a combination of controlled evaporation and thermal concentration of chemicals. Because it does not require electric heat to concentrate, this method has a number of advantages over current

procedures including greater safety, speed, efficiency, and variety of samples that can be processed (including heat-sensitive chemical compounds). It also is very economical; the cost to produce the concentrator is about one-fourth that of the lowest-priced commercial unit now available. The chemist has used his method successfully to concentrate promising cancer drugs beta-carotene and taxol, and isolate pollutant polychlorinated biphenyls from environmental samples. For more information, contact Thomas J. Bruno, Div. 838.02, NIST, Boulder, CO 80303-3328, (303) 497-5158.

CONSORTIUM TO HELP BUILDING SYSTEMS COMMUNICATE

NIST is looking for partners for a cooperative research and development consortium to help test the BACnet standard communication protocol. BACnet—*Building Automation and Control Networks*—will allow building control systems from different manufacturers to communicate and work together. Currently, different systems (such as those for energy management and control, security, fire detection, and telecommunications) use proprietary protocols which make interactions almost impossible. Consortium members will develop prototype control products or software which implement BACnet, or tools for developing and testing the implementations. Tests for the 2 year program will be conducted at NIST. BACnet, developed by NIST and building industry experts, has been published as a draft standard by the American Society of Heating, Refrigerating, and Air-Conditioning Engineers. For further information, contact Steven Bushby at (301) 975-5873.

PLAN ANNOUNCED TO HARMONIZE U.S. LABS

In a major effort to improve the acceptance of U.S. products in foreign markets, NIST is proposing to make the National Voluntary Laboratory Accreditation Program fully compatible with international standards, both those used by other accreditation systems in the European Community and worldwide for lab accreditation and quality systems management. NVLAP procedures will be revised and expanded to include calibration labs; to ensure compatibility with conformity assurance and assessment concepts; and to assure accreditation with relevant ISO documents (such as ISO Guide 25, General Requirements for the Technical Competence of Testing Laboratories and the ISO 9000

Standard Series on quality management and assurance). For information on the proposed changes to the federal regulations on NVLAP procedures, contact Albert D. Tholen, NVLAP, A162 TRF Building, NIST, Gaithersburg, MD 20899-0001, (301) 975-4016, fax: (301) 926-2884.

NOW HEAR THIS: SOUND USED FOR CLEANER BURNS

Most commercial and industrial burners ignite fuel supplied through pressurized nozzles. The nozzles atomize the fuel stream into tiny droplets for better combustion and less pollution. A new way of atomizing fuel with sound waves could improve efficiency and reduce emissions even more. NIST and a private company recently signed a cooperative research and development agreement to investigate high-power acoustic nozzles. These devices can provide droplets of known size and distribution from a high-quality orifice plate or even from commercial pressurized nozzles. Researchers plan to study whether these nozzles are feasible for combustion systems. Tests at the NIST Spray Combustion Facility will check spray characteristics, flame stability, and emission levels. The research is part of a NIST program to design more fuel-efficient and environmentally acceptable combustion systems for U.S. industry.

MAJOR BARRIER TO ADVANCED MATERIALS IDENTIFIED

More than 250 people from 12 countries met at NIST recently to strengthen communications and technology transfer among researchers and engineers involved in ceramics and composites machining. The high cost associated with machining and finishing was identified as a major barrier to the use of these materials in commercial components. It was concluded that development of new machining technologies for advanced materials requires interdisciplinary research and collaboration between industry, government, and universities. The conference proceedings, *Machining of Advanced Materials, Proceedings of the International Conference on Machining of Advanced Materials*, July 20-22, 1993 (NIST SP 847), contains 48 papers on machining and finishing techniques, surface quality, cutting tools, precision grinding, and other topics. Copies are available prepaid for \$33 from the Superintendent of Documents, U.S. Government Printing Office, Washington, DC 20402-9325, (202) 783-3238. Order by stock no. 003-003-03218-2.

GATT STANDARDS ACTIVITIES REPORTED FOR 1992

The annual report, GATT Standards Code Activities of the National Institute of Standards and Technology 1992 (NISTIR 5194), describes the NIST Standards Code and Information Program's role in supporting industry with information on standards and certification information activities that might affect U.S. trade. SCIP operates the U.S. inquiry point for standards and certification information in support of the General Agreement on Tariffs and Trade, or GATT, Standards Code. For 1992, SCIP received and processed 394 notifications of proposed regulations; reported 20 proposed U.S. technical regulations to the GATT Secretariat in Geneva, Switzerland; and responded to more than 8500 inquiries on the existence, source, and availability of standards and related documents. SCIP also operates a GATT hotline on proposed foreign regulations (301) 975-4041, and a European Community hotline with information on draft EC documents (301) 921-4164. To obtain the report, send a self-addressed mailing label to SCIP, A163 TRF Building, NIST, Gaithersburg, MD 20899-0001, (301) 975-4037.

NEW SOFTWARE SIMPLIFIES SEMICONDUCTOR MEASUREMENTS

Two-probe (spreading) and four-probe resistance measurements are important for determining a semiconductor's resistivity profile (electrical activity). A new report and corresponding software package known as RESPAC provides users with a simplified means of accomplishing this critical measurement. Consisting of ten FORTRAN77 programs, the RESPAC software may be used to calculate the two-probe resistance from the resistivity profile, the resistivity profile from the two-probe resistance, and the four-probe resistance from the resistivity profile. The report, Semiconductor Measurement Technology: A Collection of Computer Programs for Two-Probe Resistance (Spreading Resistance) and Four-Probe Resistance, RESPAC (NIST SP 400-91), supplies background material enabling the reader to make optimal use of the software package. Single copies of NIST SP 400-91 and the RESPAC programs are available by contacting John Albers, B310 Technology Building, NIST, Gaithersburg, MD 20899-0001, (301) 975-2075, fax: (301) 948-4081, and email via the Internet system (albers @sed.eeel.nist.gov).

CRYOGENIC ALLOY NOW AVAILABLE FOR LICENSING

Welding seams in magnet cases and other components of superconducting magnets must remain fracture-resistant in the cryogenic temperatures (4 K to 77 K) in which such magnets operate. NIST researchers have developed a new technology which, when incorporated into a consumable welding electrode, produces a strong alloy that achieves the needed durability. The alloy contains nickel, chromium, manganese, molybdenum, copper, nitrogen, and iron. It remains very ductile and provides a yield strength of 900 MPa at cryogenic temperatures. This is two to three times stronger than conventional construction steel at room temperature. For technical information, contact Thomas Siewart, Div. 853.07, NIST, Boulder, CO 80303-3328, (303) 497-3523. For licensing information, contact Mike Blaney, Office of Technology Commercialization, B256 Physics Building, NIST, Gaithersburg, MD 20899-0001, (301) 975-2870.

NEW FACILITY DESIGNED FOR BETTER ANTENNA ASSESSMENTS

Aerospace and defense-oriented companies will be interested in a new, multipurpose antenna facility recently put into operation at NIST's Boulder, CO, laboratory. It is used to perform extrapolation gain, probe pattern, spherical near-field, cylindrical near-field, and polarization measurements. The frequency range is from 1 GHz to 75 GHz. The facility has 10 m long horizontal rails for gain measurements using the NIST-developed extrapolation technique. At this length, gain calibrations at 1 GHz can be performed on antennas with apertures as large as 1 m. Another setup allows antennas up to 2 m in length to be accommodated for probe pattern measurements and also permits spherical near-field measurements on antennas up to 3.5 m in diameter. A set of 6 m long vertical rails allows cylindrical near-field measurements on antennas up to 3.5 m in diameter. For more detailed information on the new facility, contact Sarabeth Moynihan, Div. 104, NIST, Boulder, CO 80303-3328, (303) 497-3237. Ask for paper no. 31-93.

**1993 WEIGHTS AND MEASURES LABS
DIRECTORY PUBLISHED**

State and other labs accredited by the NIST Office of Weights and Measures are listed in *State Weights and Measures Laboratories: State Standards Program Description and Directory, 1993 Edition (NIST SP 791)*. The publication serves as a guide for locating and obtaining measurement services required by contract or law. Accreditation by NIST indicates the lab is capable of providing a measurement service, but each state is responsible for verifying its measurement traceability. The directory lists a lab's accreditation period; general data such as address, telephone/fax number, and names of staff members; services available; and fees for services. Accreditation requirements currently are being revised to include the adoption of ISO Guide 25. Most accredited labs will meet ISO 9000 customer requirements. Copies of SP 791 are available for \$8.50 prepaid from the U.S. Government Printing Office, Washington, DC 20402, (202) 783-3238. Order by stock no. 003-003-03220-4.

**ATOMIC-LEVEL DEPOSITS PROMISE
SOLID RETURNS**

NIST has installed a unique, state-of-the-art chemical beam epitaxy system at its Boulder, CO, laboratory. The CBE is a high-tech, computer-controlled vacuum system that uses thermally vaporized solid elements, metal-organic liquids, and gas chemicals as sources for creating semiconductor materials with specific electronic and optical properties for advanced optoelectronic devices. With the CBE, elements can be deposited, as precise crystalline forms, uniformly over large areas while monitoring the growth of individual atomic layers. The elements of primary interest are aluminum, gallium, indium, arsenic, and phosphorous—all basic ingredients for optoelectronic devices such as semiconductor diode lasers and optical detectors. NIST's role is to provide metrology support for the optoelectronic industry. The CBE machine will be used to: (1) develop metrology to support the actual crystal growth process, (2) make specific structures to evaluate new metrology concepts and (3) make unique devices not otherwise available but required for advanced metrology and measurement standards. For more information, contact Mark McCollum, Div. 814.02, NIST, Boulder, CO 80303-3328, (303) 497-5167.

**RESEARCHER WINS TURKEY'S HIGHEST
SCIENCE AWARD**

A NIST scientist received the Republic of Turkey's highest scientific honor in an award ceremony in Ankara on Sept. 6, 1993. A 12 year veteran of NIST (and its predecessor, the National Bureau of Standards), the scientist has been investigating the chemical mechanisms of DNA damage for more than 2 decades. The Scientific and Technological Research Organization of Turkey recognized the Turkish-born scientist for his research on DNA damage by free radicals, molecules believed responsible for certain cancers and other diseases. He also has developed a method for identifying and assessing molecular-level damage to DNA in cells and organs. "If you're able to understand the mechanisms of DNA damage and repair, you could potentially develop the necessary means to prevent or repair the DNA damage in cells," the scientist explains. A naturalized U.S. citizen, the scientist also received the 1989 Hillebrand Award of the American Chemical Society.

**PROPOSALS SOUGHT FOR PRECISION
MEASUREMENT GRANTS**

NIST is seeking project proposals for its 1995 Precision Measurement Grants. The grants are for \$50,000 for 1 year and may be renewed for up to 2 additional years. Prospective candidates must submit summaries of their proposed projects and biographical information to NIST by Feb. 1, 1994, to be considered for the current grants, which will run from October 1994 through September 1995. The Precision Measurement Grants are awarded each year to scientists in U.S. academic institutions for work in determining values for fundamental constants; investigating related physical phenomena; or developing new, fundamental measurement methods. For further information, contact Barry N. Taylor, B160 Physics Building, NIST, Gaithersburg, MD 20899-0001, (301) 975-4220.

**DATA TABLES ON ETHANE
PROPERTIES AVAILABLE**

NIST's study of the thermophysical properties of fluid ethane has been documented in several forms: as an equation of state and a limited number of tables based on critical analysis of the best experimental data in the literature [*J. Phys. Chem. Ref. Data*, **20**(2), 275-347 (1991)]; as a companion publication with more complete tables and extensive graphical comparisons between the data

and correlating equations (the 1990 NIST Technical Note 1346, Tables for the Thermophysical Properties of Ethane); and now, as the complete tabulation of the data considered in the study. This latest publication, Tables of Experimental Data Used for the Correlation of the Thermophysical Properties of Ethane (NISTIR 3953), includes comparisons between the data and the correlations, and the weight assigned to each point during the latter's development. Properties considered include vapor pressures, densities of saturated liquid and vapor, the pressure-vapor-time relationship in the single phase, isochoric and isobaric heat capacities, sound speed, viscosity, and thermal conductivity. The general range of the data is from the triple point temperature near 90.4 K to about 625 K, and for pressures to 100 MPa. Both NISTIR 3953 and TN 1346 are available from the National Technical Information Service, Springfield, VA 22161, for \$44.50 each. Order by PB 93-173417 (NISTIR 3953) and PB 93-160786 (TN 1346).

FIRST PRODUCT SUCCESSFULLY MACHINED USING STEP

An automobile connecting rod doesn't sound like something that would make history, but one designed and built by a major automobile manufacturer and the Department of Energy's AlliedSignal Kansas City Plant recently did. The engine part was the first product created using STEP (Standard for the Exchange of Product model data). The new technology enables companies to express and share a product's design, manufacturing, and support processes via computer in a three-dimensional standard format. STEP, whose U.S. development has been primarily coordinated by NIST, was approved as a draft international standard in February by the International Organization for Standardization. The automobile manufacturer's engineers hope to use STEP to improve processes for powertrain design and manufacture, ultimately reducing current automotive engine design lead time and development costs by an estimated 25 percent. The automobile company, AlliedSignal, the Commerce Department, and the Department of Energy are members of the National Initiative for Product Data Exchange, an industry-led organization established to accelerate digital product data exchange development and use. NIPDE is hosted by NIST.

NIST MEASUREMENT TECHNOLOGY GOES TO MARKET

Prototypes of a NIST-developed measurement technology played well in Peoria—at a private company's Technical Center there—and now an equipment manufacturer says the technology is ready for market. The equipment manufacturer recently announced it is commercializing NIST's novel interim testing standard device for assessing the performance of coordinate measuring machines, which firms use to check the dimensions of manufactured parts and assembled products. Typically, companies calibrate their CMM's about once a year, but without periodic checks between calibrations, they cannot be certain that their machines are continuing to measure accurately. If not, firms may reject parts that are within tolerance limits or let unacceptable parts slip through. The NIST invention consists of inexpensive, calibrated ball bars (two steel spheres connected by a steel bar) kinematically mounted on an arm that can be rapidly rotated throughout most of a CMM's three-dimensional work zone. A complete system check-out can be completed within 15 min. Under a cooperative research and development agreement, a private company tested several prototypes of the interim standard, providing the NIST inventors with feedback that led to improvements in subsequent versions. The NIST work was supported by the U.S. Air Force, the U.S. Navy, a private company, and an equipment manufacturer.

CRADA SETS PLANS FOR ATOMIC MICROCLOCK IN MOTION

Imagine a clock with atomic accuracy, roughly the size of a cube 10 cm on each side and running on only half a watt of power. The development of such a device is under way, thanks to a cooperative research and development agreement between NIST and a private company. The company's Science and Technology Center in Pittsburgh has already built and tested a prototype miniature atomic clock that runs on electricity. However, the stability is poorer than predicted. Under the CRADA, NIST, which pioneered the development of atomic clocks, will work with the private company on resolving the stability issue. NIST also will assist the company with measurements to ensure that the company's specifications are met. As a result of their efforts, the partners hope to

better understand the physics and electronics associated with producing a tightly packaged clock. NIST expects to learn generic fabrication and processing methods that will be helpful in developing future primary frequency standards. The company has identified many commercial and military systems that would benefit from a miniature atomic clock. For technical information, contact Bob Drullinger at NIST at (303) 497-3183 or Irving Liberman at Westinghouse at (412) 256-1571. For marketing information, contact David Leksell at (412) 256-1467.

NCWM TO WORK ON PRICE ACCURACY IN RETAIL STORES

In response to nationwide concern about price accuracy in retail stores, the National Conference on Weights and Measures has established a Working Group on Price Verification. The aim will be to develop a field handbook for officials to use in verifying the accuracy of advertised prices. Recent national news stories have accused both retailers, and state and local weights and measures officials of failing to ensure that posted prices match advertised and "scanned" prices, and have called for tougher inspection standards. To address this important issue, NCWM invited state and local weights and measures officials as well as business representatives to participate in an effort to develop uniform price accuracy test procedures. Plans call for a final report to be ready for adoption by NCWM at its 79th Annual Meeting, San Diego, CA, in July 1994. For information, contact Ken Butcher, Office of Weights and Measures, A617 Administration Building, NIST, Gaithersburg, MD 20899-0001, (301) 975-3991, fax: (301) 926-0647.

PARTNERS TO DEVELOP POWERFUL TUNABLE LASER

NIST and a private company have signed a cooperative research and development agreement to develop frequency-tunable diode lasers for a variety of commercial applications, including pollution monitoring and isotope detection. The company is a world leader in high-power laser diode technology, and NIST is a leader in using diode lasers for scientific applications. NIST has developed several low-power, tunable laser diode prototypes; however, their performance has been limited by designs not optimized for frequency-tuning applications. The goal of the collaboration is to custom-fabricate a broadly tunable (over 10 nm) external cavity semiconductor laser with narrow linewidths (less than

500 kHz) and high power (20 mW). The program has three aspects: development of high-power laser diodes suitable for implementation into the external cavity; development of optomechanical designs that are compact, stable, and efficient; and optical characterization of the external cavity laser. For more information, contact Leo Hollberg of NIST at (303) 497-5770 or David Welch of SDL at (408) 943-9411.

NEW DEVICE PRECISELY MEASURES HYDROGEN IN METALS

Failed turbine blades, fouled silicon chips, faltering superconductors. Blame them on hydrogen, an element that can embrittle metals in high concentrations. Chemists at NIST's Cold Neutron Research Facility have developed an instrument for nondestructive measurement of hydrogen and other elements. Their method, called cold neutron prompt gamma activation analysis, determines the trace hydrogen content of a sample without the disadvantages of other measurement techniques. The U.S. Air Force recently asked NIST to determine the levels of hydrogen in titanium-alloy turbine blades that had broken. Cold neutron prompt gamma activation analysis revealed that one turbine blade contained two to three times as much hydrogen as another blade from the same engine. In other tests of the new method, NIST chemists have measured hydrogen in advanced materials such as fullerenes, quartz crystals, and silicon wafers. Many of these measurements were made on request for U.S. companies. For technical information, contact Rick Paul, B125 Reactor Building, NIST, Gaithersburg, MD 20899-0001, (301) 975-6287.

ANTENNA SOFTWARE MEASURES "NEAR AND FAR"

NIST researchers have developed a new software package that allows scientists, engineers, and programmers to make complex antenna computations on any IBM RISC (Reduced Instruction Set Codes) machine. The package, named "Planar Near-Field Codes," provides analysis of near-field antenna data to obtain the far-field data; it also corrects near-field data for probe position errors. The software was transferred to the RISC systems under a developer's contract. This package is an adaptation of an earlier one designed for personal computers. To order either package, contact Lorant A. Muth, Div. 813.08, NIST, Boulder, CO 80303-3328, (303) 497-3603.

NIST LEADS INDUSTRY TO RESOLVE PROBLEMS IN DETERMINING LASER BEAM SPATIAL PARAMETERS

NIST scientists have conducted and analyzed the results of an interlaboratory comparison to test the current International Standards Organization (ISO) procedure for determining laser beam spatial parameters, which characterize the propagation of the beam. In the round-robin experiment, six manufacturers of laser beam profilers measured the same laser, each using its own measurement method for, and definition of, beam diameter, and then applied the ISO procedure to the resulting data. NIST presented the results as an invited paper at the recent SPIE OE/Technology conference in Boston, including the surprising result that values for the calculated spatial parameters disagreed by as much as 380 percent (relative standard deviation). By contrast, the beam diameter measurements agreed to within a few percent.

These results catalyzed the ISO committee to revise its procedure and to redefine laser beam diameter, and in a subsequent meeting, the committee decided that NIST should conduct a second round robin to test the revised procedure and that this intercomparison should be international in scope. At that meeting NIST presented preliminary results of a propagation-of-errors analysis of the original ISO procedure, showing that the uncertainties resulting from its application could be halved by using an alternative calculational procedure. This work has been completed and can be applied in the revised procedure. A paper has been accepted for publication in the journal *Optical and Quantum Electronics*.

NIST, SANDIA COLLABORATE TO DEVELOP TOOLS FOR EVALUATING THERMAL PERFORMANCE OF SEMICONDUCTOR DEVICE PACKAGING

NIST scientists are collaborating with their counterparts in Sandia National Laboratories in the development of new tools for evaluating the thermal performance of the packaging of semiconductor microelectronic chips. This is one of the first projects undertaken in the context of the technical agreement signed by the two organizations earlier this year. In the collaboration, NIST and Sandia will separately and jointly design test chips, Sandia will fabricate them from the design information, and NIST will develop test methods for applying them. Both laboratories will participate in test-chip evaluation. Thermal performance considerations

are vital to advanced semiconductor device design: no matter how excellent the chip, if the heat generated by its operation is not removed by the packaging, it will fail. The first stage of the collaboration is concerned with a special test chip—one of a class of “assembly test chips”—developed by Sandia and applied to the characterization of the thermal properties of various die-attach materials. Sandia has encountered some difficulty in interpreting the results and sought the benefit of NIST expertise in test structure methodology. As a result, NIST scientists have developed measurement methods and techniques, including a special constant-power circuit, for using this chip and evaluating its performance. The data from the NIST measurements show that the chip can be significantly improved through redesign to reduce parasitic resistances. Sandia is beginning the redesign and is replicating the constant-power circuit. A NIST goal of the overall effort is to supply to industry evaluated test chips for packaging characterization for sale in the Standard Reference Material mode.

NIST MEASUREMENTS OF ION KINETIC ENERGIES FROM RF PLASMAS PROVIDE BASELINE DATA FOR SEMICONDUCTOR PROCESSING

In support of advanced plasma processing steps coming into use in the semiconductor industry, NIST researchers have completed an extensive set of measurements of the kinetic energy of ions sampled from radiofrequency glow discharges. These energies represent a key parameter determining etching rates, and industry is developing instruments to monitor ion energies in real time as part of the plasma diagnostics needed for manufacturing control. The NIST project supports these developments by characterizing and calibrating the performance of the resulting diagnostic tools and by correlating electrical parameters measured by other methods in order to obtain a better understanding of the physical processes involved.

The researchers determined kinetic energies of ions from radiofrequency discharges generated in argon, helium, and hydrogen and in mixtures of argon-helium, argon-oxygen, helium-nitrogen, and argon-hydrogen in a reference parallel-plate discharge cell having well-characterized electrical parameters. These gases and gas mixtures were chosen because they are representative of gases used in plasma processing and because the cross sections and rates describing the kinetic processes occurring in the plasmas are well enough known

that observed changes in ion energy distributions can be related to changes in plasma conditions. Developing effective control for processes such as etching requires predictive models; the team's data provide means for testing the validity of various models proposed. Of particular interest to practical applications, the team made an unexpected discovery: ion energy distributions measured through an electrode agree well with those measured from the side of the plasma. This finding suggests that the methods used may be applicable to many different types of plasma reactors. The team has reported on its results to industry at five conferences and through three archival publications.

NIST CONTRIBUTES TO DEVELOPMENT OF PROTOTYPE SOFTWARE SUPPORTING COMPUTER DESIGN OF HIGH-POWER MICROWAVE TUBES

NIST scientists have been asked by the Microwave and Millimeter-Wave Advanced Computational Environment program (MMACE) to participate in the development of software protocols and interfaces in support of the design of high-power microwave products. A Tri-Service/Advanced Research Projects Agency program, MMACE goals include maximizing the effectiveness of the design process, improving the quality of products, and generally reducing the cost of doing business, especially as applied to a niche market. In Phase One, four contractor teams have written software to serve as a framework of information exchange standards to support the design and modeling of high-power microwave vacuum tubes by means of various application programs. Phase Two will result in an integrated software product that has been evaluated at a number of sites. NIST has provided the teams and the project technical director guidance and consultation based on expertise in software standards development and knowledge of the state of relevant standards in place or under development.

For example, a NIST scientist has analyzed software development plans, identified potential problems with proprietary and acceptance issues, and steered work in directions more likely to lead to general use. The problem addressed by the MMACE project is that individual application programs have been developed as independent entities

with program-specific requirements for data format and entry. Thus separate packages model magnetic circuits (magnetostatic and magnetoinductive codes), electron optics (electrostatic and electromagnetic codes), electron beam interaction with radiofrequency fields (helix traveling-wave tube and electro-magnetic particle-in-a-cell codes), thermal energy transfers and states (finite-element codes), and mechanical characteristics (also finite-element codes). An agreed-upon standardized framework will provide a basis for specifying interfaces and protocols that individual software programs will have to meet. Data formats resulting from device design processes then will be compatible with each other, with data formats supporting device manufacturing, and with data formats needed by the designers of equipment incorporating the device.

AFM MAPS OBSERVE NEW DEPOSITION PROCESS

News of a new high-resolution deposition process was highlighted in a news article in the June 1993 issue of *Laser Focus World*. The process was observed using an atomic force microscope (AFM). One of the AFM images is shown in that article.

The process involves laser-assisted metallic-vapor deposition and was developed by NIST scientists. They produced a fine grating-like structure with 212 nm periodicity and linewidths approximately 50 nm across.

The AFM measures surface topography at higher lateral resolution than traditional stylus or optical instruments. With a tip size in the range of 10 nm and a contact force in the range of 10 nN, the AFM generated a topographic image of the grating, and features to the 10 nm scale were visible. In addition to viewing the image, the AFM provides dimensional measurement in three directions. The measured area can be up to 80 μm by 80 μm in size. The dimension of the sample is not constrained, and the probe on this AFM can position on any part of a flat sample. In addition, it does not require a vacuum system, so turnaround time is fast. The AFM can also measure insulators unlike the counterpart scanning tunneling microscope, which is limited to measuring conducting surfaces only. Therefore, NIST's AFM has been an ideal tool for testing the results of the experimental deposition process, so that it could be optimized.

SEA-VIEWING RADIOMETER DEVELOPED

A high-accuracy portable transfer radiometer (SXR) for the SeaWiFS (Sea viewing Wide Field Spectrometer) project was designed and characterized at NIST. The SeaWiFS project is an ocean color remote-sensing project to study ocean biology in the first 10 m of water. The project includes a satellite instrument to be flown in 1994 and a large network of ocean-based spectroradiometers to measure down-welling and up-welling irradiance below the ocean surface in field studies. Some of the radiative transfer measurements derived through the network include aerosol samples, temperature and saline profiles, phytoplankton pigments, total suspended material concentration, and airborne fluorescence and radiances.

The development of the SXR was sponsored by NASA Goddard Space Flight Center and was used in June 1993 in an intercomparison of laboratory calibration sources at the Center for Hydro-Optics and Remote Sensing at San Diego State University. Participants included NASA, NIST, two universities, and two private companies. Through round-robin intercomparisons the SXR will verify the radiometric output of sources used to calibrate the satellite and ground-based instruments used throughout the SeaWiFS project. This will serve to improve the accuracy and long-term consistency of data produced by the SeaWiFS project over the mission lifetime of 5 years. NIST has also been asked to develop a rugged calibration source for shipboard calibration and verification of submersible spectrometers during field studies.

NEW IONIZATION SOURCE DEVELOPED FOR MASS SPECTROSCOPY

At NIST, a glow discharge cell has been coupled to a resonance ionization mass spectrometer system (RIMS) and the production of ions and atoms demonstrated. This source allows the direct analysis of solid materials and represents a first step in our goal to achieve direct compositional analysis of environmental materials without chemical processing. Potential advantages of the glow discharge source over other atomization sources are its simplicity, its applicability to direct analysis of conductors with wide coverage of the periodic table, and its sensitivity.

The glow discharge source consists of a cylindrical stainless steel cavity held at approximately 67 Pa of argon with a rod of sample material inserted from one end. A plasma is developed at

the inside end of the rod by impressing a 1000 V potential drop between the cavity wall and the rod. Neutral atoms are sputtered from the sample by bombardment of ions within an argon ion plasma, after which they are selectively ionized by means of carefully tuned lasers, and then mass analyzed in a double-focusing mass spectrometer.

A sample containing 95 percent aluminum and 5 percent iron has been examined. The ion source was operated in two modes: using glow discharge ions and using RIMS ions. The glow discharge ions gave a clean spectrum but with an enhanced peak at mass 54 corresponding to aluminum interference. The interference was completely removed in the RIMS spectrum because of the selectivity of the laser.

Work is continuing toward improvement of the selectivity and sensitivity by dramatically increasing the duty cycle with high-frequency and cw lasers.

MISSING LINK IN FISSION SYSTEMATICS FOUND

A long-standing problem in understanding the systematics of nuclear fission has been resolved by measurements carried out by a NIST scientist in collaboration with scientists from the Los Alamos and Oak Ridge National Laboratories. Missing in all earlier measurements of the neutron-induced fission of ^{236}U was a subthreshold structure in the fission probability predicted by the double-humped barrier of fission theory. This breakdown of fission formalism was difficult to understand since the expected structure is observed for fissionable nuclides of similar neutron-proton pairing.

The new measurements, using targets of very high isotopic purity and using highly selective fission fragment detection, found the expected intermediate structure in the difficult subthreshold regime of small fission probability. The new data place the anomalous ^{236}U nucleus where it belongs in fission systematics based on the well-established, two-potential-well theory of nuclear fission. The fission detectors in the experiment, a NIST specialty, were the key. They provided the needed level of discrimination against interfering radiation now believed to be the major cause of the erroneous results in earlier work. These specific experiments are part of a larger effort to establish reference and standard neutron interaction data for the design and safe operation of electric power generation systems and for medical therapy applications.

**LASER IONIZATION MONITORING
PROMISES NEW DIAGNOSTIC OF
SEMICONDUCTOR GROWTH**

Precise control of the purity and concentration of materials deposited under high vacuum during semiconductor growth is a significant factor in the "art" of fabrication processes. Lack of control of fluxes in the deposition processes can result in high failure rates and defects, and in poor junctions. At NIST an important recent technological advance was the successful incorporation of 118 nm laser ionization detection (10.5 eV per photon) into a molecular beam epitaxy (MBE) reactor. A patent has been filed on the application of this technique to commercial MBE reactors. The laser source is used to produce selective, single photon ionization of gaseous fluxes of Ga, In, As₄, As₂, and As species; the ions are detected by a time-of-flight mass spectrometer. This new laser technique affords a major new non-intrusive optical tool for the study and control of epitaxial growth. The ability to continuously and individually monitor the gas phase species involved in growth of III-V and II-VI semiconductor materials is particularly important for process control. The incorporation of non-invasive probes into advanced generations of MBE machines would make it possible to carry out in situ diagnostics to quantify and characterize the growth process, to provide optical feedback for adjustment of species concentrations, and to determine the purities of materials used during semiconductor fabrication.

**NIST RESEARCH ASSOCIATES LICENSE
BONE REPAIR/REPLACEMENT MATERIAL**

The American Dental Association Health Foundation has licensed a hydroxyapatite bone repair and replacement material developed by research associates at NIST. The material is currently completing FDA evaluation for neurosurgical and maxillofacial applications and is expected to be marketed within the next 2 years. The cement greatly simplifies surgical procedures by repairing bone defects with a biocompatible material very similar in chemistry to natural bone. Once in place, the cement becomes a template for new bone development as it is resorbed and replaced by new bone. Its use would eliminate the need for additional surgery to harvest graft material elsewhere from the patient or the use of less satisfactory alloplastic materials. This surgical bone repair material was developed under an ongoing Cooperative Research and Development Agreement between

NIST and the American Dental Association Health Foundation.

**CLASSIFICATION SYSTEM FOR ADVANCED
CERAMICS DEVELOPED BY INTERNATIONAL
COLLABORATION**

An international effort chaired by a NIST scientist, and conducted under the auspices of the Versailles Project on Advanced Materials and Standards (VAMAS), produced a classification system for advanced ceramics that meets the prescription set by the worldwide ceramics industry. VAMAS, operating under a memorandum of understanding between Canada, France, Germany, Italy, Japan, the United Kingdom, the United States, and the Commission of the European Communities, supports precursor technical projects leading to advanced materials standards. The classification system as developed is built upon a non-hierarchical, matrix-type scheme accessible by a number of entry routes to build relational databases. The system identifies 500 different advanced ceramic product classes, sortable by a machine-readable coding system comprised of four independent descriptor fields: A—application, C—chemical/form character, P—processing, and D—property data. The system's design makes it multifunctional to meet the classification needs of individuals, companies, industries, and governments alike.

PHASE TRANSITION PUZZLE CLARIFIED

A collaborative study involving scientists from NIST and Brookhaven National Laboratory has provided the answer to a fundamental question concerning phase transitions in crystals. When a crystal is brought close to its transition temperature T_c , small regions of the crystal undergo thermally induced fluctuations into and out of the low-temperature ordered phase. A central feature of the theory of second-order phase transitions is that the average size of these regions can be characterized by a single correlation length which diverges at T_c . In 1986, high-resolution x-ray scattering experiments found that the cubic to tetragonal structural phase transition in SrTiO₃ exhibited two correlation lengths instead of one. This startling result motivated an intense study of this and various other systems possessing both structural and magnetic phase transitions, the results of which suggested that two correlation lengths may be a feature common to all phase transitions in condensed matter systems. Available experimental techniques could

not provide further clarification: x rays, which probe crystal surfaces to a depth of order $1\ \mu\text{m}$, could not show if it is absent in the crystal bulk; neutrons, which do probe the bulk, were not able to separate surface and bulk contributions.

The recent experiments at NIST utilized high-resolution neutron scattering at the reactor's BT7 reflectometer to study a cube-shaped single crystal of Tb, which exhibits a transition to a magnetically ordered spiral phase. By using a $300\ \mu\text{m}$ wide beam, very thin slices of the Tb crystal could be isolated and studied by translating the sample through the beam. The results show that the origin of the second correlation length lies in the near-surface volume or "skin" of the Tb sample, and not in the bulk. In this context the meaning of skin is distinct from that of surface since the second correlation length is spread over several hundred μm and not just one or two.

As yet, a satisfactory microscopic explanation for this phenomenon has not been formulated. One model suggests that extended crystal defects such as dislocations might produce a second correlation length. Another possibility is that the phenomenon results from the boundary condition imposed by the crystal surface on the interaction driving the transition. The unique facilities available at the reactor will be used in future experiments in an effort to further resolve this important and fundamental question.

SIMULTANEOUS MEASUREMENT OF SOOT VOLUME FRACTION AND TEMPERATURE IN FLAMES

Radiative heat transfer governs burning and flame-spread rates in fires and, therefore is a key factor in assessing potential fire hazards. The radiative heat feedback from a flame to the fuel surface is controlled by the temperature and soot concentration distribution inside the flame. NIST scientists have evaluated the performance of a new *in situ* technique for measuring soot volume fraction and temperature developed by colleagues at the University of Maryland under grant from BFRL. The method involves determination of the temperature and soot volume fraction from two-line (900 nm and 1000 nm) emission measurements and an independent determination of the latter from a third-line (632.8 nm) laser extinction measurement. For a premixed, fuel-rich ethylene/air flame of varying equivalence ratio, good agreement was obtained with previously published data. However, the soot volume fractions measured by the two

methods differed. Further experiments demonstrated that this was not due to scattering by the soot or to light absorption by large molecules. The agreement between the two values improved when extinction measurements were performed with longer wavelength light sources. This observation, combined with a strong sensitivity to the refractive index at shorter wavelengths, leads to a recommendation that future soot volume fraction measurements be made with a light source such as a 1523 nm He-Ne laser. A paper has been submitted to Combustion and Flame.

APPLICATION PORTABILITY PROFILE (APP) GUIDE REVISED

Computer system users need open systems that provide interoperability of products and portability of people, data, and applications throughout heterogeneous computing environments. NIST Special Publication 500-210, APP, The U.S. Government's Open System Environment Profile OSE/1 Version 2.0 (known as the APP Guide), provides recommendations on a variety of specifications that fit the requirements of U.S. government systems. The APP integrates industry, federal, national, international, and other specifications into a federal application profile to provide the functionality necessary to accommodate a broad range of federal information technology requirements.

The revised document assists federal agencies in making informed choices regarding the selection and use of Open System Environment specifications and in developing more selective application profiles based on the APP. The report targets managers and project leaders who acquire, develop, and maintain information systems supported by heterogeneous computing environments.

NIST SUPPORTS THE DEPARTMENT OF DEFENSE COMPUTER-AIDED ACQUISITION AND LOGISTIC SUPPORT (CALS) INITIATIVE IN COMPUTER GRAPHICS

To meet CALS conformance test requirements, NIST developed validation test services for testing metafiles and generators for conformance to Federal Information Processing Standards (FIPS) 128-1, CGM, and the CALS CGM application profile, MIL-D-28003. NISTIR 5191, Computer Graphics Metafile (CGM) Test Requirements Document, updates the initial test requirements document to include new functionality and additional require-

ments resulting from revisions to the standard and the CALS CGM profile. The updated conformance test suite and tools ensure that a CGM product correctly implements FIPS 128-1 and its associated application profile. NIST is also developing a test service for interpreters in support of CALS.

FIPS FOR MASSACHUSETTS GENERAL HOSPITAL UTILITY MULTI-PROGRAMMING SYSTEM (MUMPS) PROGRAMMING LANGUAGE REVISED

The Secretary of Commerce recently approved a revision to FIPS 125, MUMPS, which will be published as FIPS 125-1. Now known as M Technology, the MUMPS language was developed at Massachusetts General Hospital in 1969 and has been adopted for use in government health care systems. The standard promotes the portability of MUMPS programs for use on a variety of computer systems. FIPS 125-1 adopts American National Standard for MUMPS, ANSI/MDC X11.1-1990, which was developed by industry and users. NIST is developing a validation suite to test MUMPS language processors for conformance to the standard.

NIST/ASA/NSF FELLOW DEVELOPS NEW STATISTICAL METHODS FOR MANUFACTURING PROCESS QUALITY ASSURANCE

A NIST visiting research fellow, and a NIST scientist have developed new statistical methods for manufacturing process quality assurance. In particular, they proposed a new statistical model for measurements collected on the circumference of circular features using a coordinate measuring machine. The statistical model is motivated by hole location problems of the automobile gear carrier manufacturing process. The model takes into consideration the variability of center locations in a series of machined parts. Statistical procedures were developed to assess the performance of the manufacturing process in producing parts that conform to design specifications, and to keep track of the trend of the manufacturing process over time.

In related work, the researchers developed new statistical procedures for estimating the proportion of conformance of a manufacturing process. Proportion of conformance is defined as the proportion of products with quality characteristics inside the specification limits and is, therefore, a measure of the capability of the process in meeting design specifications. Proportion of conformance,

in many ways, is preferable to the widely used process capability indices for assessing the performance of manufacturing processes. The new methodology has been implemented in a computer program that produces both point and interval estimators for the proportion of conformance. The work described above was performed at NIST under the NIST/ASA/NSF Fellowship Program, administered by the American Statistical Association.